

---

# Cold Atoms and Bose-Einstein Condensates in Optical Dipole Potentials

Vom Fachbereich Physik der Technischen Universität Darmstadt  
zur Erlangung des Grades  
eines Doktors der Naturwissenschaften  
(Dr. rer. nat.)

genehmigte Dissertation von

**Johanna Nes M.Sc.**  
aus Hoorn, den Niederlanden

Darmstadt 2008  
D17

---

Referent: Prof. Dr. Gerhard Birkel  
Koreferent: Prof. Dr. Thomas Halfmann

Tag der Einreichung: 13.06.08  
Tag der Prüfung: 07.07.2008

I am trying to challenge and subvert my own fundamental assumptions as to what constitutes rationally constructed behaviour.

DNA

# CONTENTS

1. <i>Introducing Bose-Einstein Condensates in Dipole Traps</i> . . . . .	1
2. <i>Bose-Einstein Condensation</i> . . . . .	5
2.1 The Non-Interacting Bose Gas . . . . .	5
2.1.1 The Thermodynamic Limit . . . . .	5
2.1.2 The Finite Size Effect . . . . .	8
2.1.3 Interacting Atoms . . . . .	10
2.2 The Wave Function of the Condensate . . . . .	12
2.2.1 An Ideal Bose Gas . . . . .	12
2.2.2 Taking Interactions into Account . . . . .	13
The Gross-Pitaevskii Equation . . . . .	14
The Thomas-Fermi Approximation . . . . .	16
3. <i>Trapping Atoms in Optical Dipole Traps</i> . . . . .	19
3.1 The Optical Dipole Potential . . . . .	19
3.1.1 The Classical Oscillator Model . . . . .	20
3.1.2 The Semi-Classical Model . . . . .	23
3.1.3 Dressing Atoms . . . . .	24
3.2 Trapping Atoms with Lasers . . . . .	26
3.2.1 Catching Atoms with a Single Beam . . . . .	26
3.2.2 Crossing the Laser Beams . . . . .	28
3.3 Putting Theory into Practice . . . . .	29
3.3.1 The Vacuum Chamber . . . . .	30
3.3.2 Cooling the Atoms . . . . .	32
3.3.3 The Magneto-Optical Trap (MOT) . . . . .	33
3.3.4 The Lasers . . . . .	34
3.3.5 The Optical Dipole Trap in Practice . . . . .	35
3.3.6 Detecting the Atoms . . . . .	38

---

4. <i>A Fast Route to Bose-Einstein Condensation</i> . . . . .	41
4.1 Characterizing the Dipole Trap . . . . .	41
4.1.1 The Lifetime . . . . .	42
4.1.2 Oscillation Frequencies . . . . .	47
4.2 Loading the Atoms in the Dipole Trap . . . . .	49
4.3 Evaporative Cooling . . . . .	53
4.3.1 Colliding Atoms . . . . .	53
4.3.2 Evaporating Atoms . . . . .	56
4.4 Detecting a Bose-Einstein Condensate . . . . .	58
4.5 Bose-Einstein Condensation . . . . .	62
4.6 Summarizing the Route to BEC . . . . .	67
5. <i>Using the Coherence Properties of Bose-Einstein Condensates</i> . . . . .	69
5.1 Introduction . . . . .	69
5.2 The Microfabricated Ring-Lens . . . . .	71
5.3 1D Quantum Degenerate Gases in a Toroidal Trap . . . . .	72
5.4 A Possible Interferometry Experiment . . . . .	75
6. <i>Some Concluding Remarks</i> . . . . .	79
 <i>Appendix</i>	 81
A. <i>The Rubidium Atom</i> . . . . .	83
B. <i>Parameters of the Optical Dipole Trap</i> . . . . .	87

## SUMMARY

In 1925, Einstein predicted the condensation of bosons into the ground state of the system for low (but finite) temperatures. Several phenomena, including superfluidity and superconductivity have been associated with Bose-Einstein condensation, but these systems interact strongly with their environment and pure Bose-Einstein condensation could not be established. It took 70 years, in which time the laser was discovered, and laser cooling techniques to manipulate atoms in a dilute atomic gas, before Bose-Einstein condensation in dilute atomic gases could be demonstrated in 1995. In the first condensation experiments, BECs were created in a magnetic trap. Since in a magnetic trap not all  $m_F$  states of the atom can be trapped simultaneously, thereby limiting the number of experiments that can be done, other ways of trapping and generating BECs were sought and found. In 2001, the first all-optical BEC was made, where the dipole force was used to trap atoms in the crossing of two far red detuned laser beams. In an optical dipole trap not only atoms in different internal states can be trapped, but also different atomic species simultaneously.

In this thesis, the formation of an all-optical Bose-Einstein condensate with rubidium atoms is presented. Conventional all-optical BECs are usually created in high power CO<sub>2</sub> laser dipole traps, or have complicated laser cooling schemes and complex dipole trap setups. In our simple and straightforward setup, we load rubidium atoms from a magneto-optical trap into a crossed optical dipole trap created by a single frequency Yb:YAG laser with a wavelength at 1030 nm. The small wavelength allows for a small diffraction limit, and permits us to use standard optical materials, thus making the experimental setup cost effective. Other attempts to achieve Bose-Einstein condensation in a multi-mode (frequency) fiber laser at 1064 nm failed, because the atom loss was quite high. It is assumed that the multi-mode character of the fiber laser induces Raman transitions in rubidium atoms, thereby heating them.

We can trap about  $\sim 5 \cdot 10^7$  atoms in a single beam dipole trap out of

$\sim 5 \cdot 10^9$  atoms trapped in the MOT, and  $\sim 350,000$  atoms can be trapped in a crossed beam dipole trap due to the smaller trap volume. 70% of the atoms in the dipole trap is optically pumped into one  $m_F$  state. Quantum degeneracy is reached by evaporatively cooling the atoms in the crossed dipole trap by ramping down the laser power with three linear ramps. We can independently change the power of each beam by an AOM. This allows us to use one beam as an atom waveguide for future experiments.

After evaporation, we typically have about 10,000 atoms at a temperature below the critical temperature. We have proved Bose-Einstein condensation by using the anisotropic expansion of a quantum degenerate gas trapped in an anisotropic potential. The aspect ratio of our atom cloud changed during a time of flight from 0.7 to 1.2 in 10 ms, thus proving that we have reached quantum degeneracy. We have about 5,000 condensed atoms in our optical dipole trap at a temperature less than 100 nK. The remaining atoms are thermal. Bose-Einstein condensation is obtained within 8 s, and we can repeat the experiment every 30 s.

It should be mentioned that the Bose-Einstein experiment was moved from the "Leibniz Universität Hannover" to the "Technische Universität Darmstadt", and had to be completely rebuilt. All-optical Bose-Einstein condensation was reached within one year after the move.

Our Bose-Einstein condensation setup presents an ideal starting point for using our condensates in combination with miniaturized atom optical setups based on our novel microfabricated optical elements. With our microlenses, we can create a number of possible dipole trap configurations, such as the dipole trap array or the cylindrical microlens array. Using microlenses in miniaturized atom optical setups opens a completely new field of coherent atom optics. Also because the tight confinement of the microtraps allows us to load a 3D BEC, a 1D BEC, or a Tonks-Girardeau gas in the micropotentials depending on the density.

## ZUSAMMENFASSUNG

Einstein sagte 1925 voraus, dass unterhalb einer gewissen Temperatur nahe dem absoluten Nullpunkt ein signifikanter Anteil eines bosonischen Atomensembles im Grundzustand eines Systems kondensieren kann. Mehrere Phänomene wie zum Beispiel die Suprafluidität und die Supraleitung stehen in engem Zusammenhang mit der Bose-Einstein-Kondensation, jedoch gibt es in diesen Systemen starke Wechselwirkungen mit der Umgebung, sodass die Realisierung eines reinen Bose-Einstein-Kondensates erschwert ist. Es dauerte 70 Jahre, in denen der Laser und die Laserkühltechniken entwickelt wurden, die eine Manipulation von Atomen erlauben, bis 1995 erstmals ein Kondensat in verdünnten atomaren Gasen realisiert werden konnte. In den ersten Experimenten fand die Kondensation in einer Magnetfalle statt. Da aber in einer solchen Falle nicht alle magnetischen Unterzustände eines Atoms gefangen werden können, wurde nach anderen Möglichkeiten gesucht. In 2001 wurde das erste Kondensat mit rein optischen Methoden erzeugt. In diesem Experiment wurde die optische Dipolkraft genutzt, um Atome im Fokus zweier gekreuzter fern rotverstimmter Laserstrahlen zu gefangen. In einem rotverstimmten Laserstrahl können nicht nur alle magnetische Unterzustände gleichzeitig gefangen werden, sondern auch unterschiedliche Atomsorten.

In dieser Doktorarbeit wird die Erzeugung eines Bose-Einstein-Kondensates aus Rubidium-Atomen mit rein optischen Mitteln präsentiert. Bislang wurden Kondensate zumeist im Fokus eines Hochleistungs-CO<sub>2</sub> Laserstrahls erzeugt, oder die verwendeten experimentellen Aufbauten waren sehr aufwendig und komplex. In unserem einfachen Aufbau werden Rubidium-Atome direkt aus einer magneto-optischen Falle in einer gekreuzten Dipolfalle umgeladen. Die Dipolfalle wird von einem Yb:YAG Laser mit einer Wellenlänge bei 1030 nm erzeugt. Die niedrige Wellenlänge weist ein geringes Beugungslimit auf und erlaubt uns die Benutzung von konventioneller Optik und macht dadurch den experimentellen Aufbau kostengünstig. Andere Versuche ein Kondensat mit einem Mehrmodenfaserlaser bei einer Wellenlänge von 1064 nm zu erzeugen sind gescheitert, da die Verluste in der Dipolfalle

viel zu hoch waren. Es wird vermutet, dass die Mehrmoden-Charakter des Faserlasers Raman Übergänge in den Rubidium-Atomen hervorgerufen werden, die zu einem Aufheizen des Atomensembles führen.

Wir können  $\sim 5 \cdot 10^9$  Atome in unserer magneto-optischen Falle fangen, von denen wir  $\sim 5 \cdot 10^7$  Atome in einer Einzelstrahldipolfalle, und etwa 350,000 Atome in einer gekreuzten Dipolfalle umladen können. 70% der Atome pumpen wir optisch in einen einzigen magnetischen Unterzustand. Quantenentartung wird erreicht durch das evaporative Kühlen der Atome in der Falle, indem die Intensität des Lasers in drei linearen Rampen heruntergefahren wird. Dabei können wir über akustooptische Modulatoren jeden der beiden Strahlen individuell in der Leistung ansteuern. Dies erlaubt es uns auch, einen der Strahlen als einen Wellenleiter für künftige Experimente zu nutzen.

Nach der Evaporation haben wir typischerweise 10,000 Atome mit einer Temperatur unterhalb der kritische Temperatur. Wir haben das Erreichen der Bose-Einstein Kondensation nachweisen können, indem wir die anisotrope Ausdehnung eines Kondensats in einem anisotropen Potential ausgenutzt haben. Das Aspektverhältnis unserer Atomwolke hat sich dabei innerhalb 10 ms von 0.7 auf 1.2 umgekehrt, damit wurde das Beweis von dem Erreichen der Bose-Einstein Kondensation in unserer optischen Dipolfalle geliefert. Wir haben 5,000 kondensierte Atome bei einer Temperatur unterhalb 100 nK in unserer Dipolfalle. Die restlichen Atome sind thermisch. Die Bose-Einstein Kondensation kann innerhalb 8 s erreicht werden, und wir können alle 30 s das Experiment wiederholen.

Dabei sollte erwähnt werden, dass das Experiment von dem Leibniz Universität Hannover nach der Technischen Universität Darmstadt umgezogen wurde. Das Experiment wurde komplett neu aufgebaut, und Bose-Einstein Kondensation konnte innerhalb eines Jahres nach der Neuaufbau erreicht werden. Unser Aufbau stellt eine ideale Grundlage für weitere atomoptische Experimente mit unseren Kondensaten in mit mikrooptischen Elementen erzeugten Dipolfallen dar. Mit diesen Mikrolinsen können wir verschiedene Dipolfallengeometrien realisieren, wie zum Beispiel ein Dipolfallenarray oder ein zylindrisches Dipolfallenarray. Das Benutzen von Mikrolinsen in miniaturisierten atomoptischen Aufbauten eröffnet ein neues Forschungsgebiet in der kohärenten Atomoptik. Besonders der enge Einschluss in den Mikrofallen sollte uns die Erzeugung eines 3D Kondensats, eines 1D Kondensats, oder eines Tonks-Girardeau gases erlauben, je nach dem wie die Dichte der Wolke ist.

# 1. INTRODUCING BOSE-EINSTEIN CONDENSATES IN DIPOLE TRAPS

In 1924, Satyendra Nath Bose derived Planck's law for blackbody radiation. In his paper he assumed that the photons were identical and indistinguishable, and allowed any number of photons to occupy the same quantum state. He sent his paper to Albert Einstein, who generalized this idea to an ideal gas of identical atoms or molecules. This led to the Bose-Einstein distribution

$$f(E) = \frac{1}{e^{(E-\mu)/k_B T} - 1}, \quad (1.1)$$

where  $E$  is the energy,  $\mu$  is the chemical potential,  $k_B$  is Boltzmann's constant and  $T$  is the temperature. Einstein did an astonishing discovery, he found that for low but finite temperatures the particles condense into the ground state! This phenomenon is called Bose-Einstein condensation (BEC), and it can only occur for integer spin particles (bosons).

Bose-Einstein condensation is based on the indistinguishability and wave nature of particles. An ideal gas at room temperature can be described with a classical Maxwell-Boltzmann distribution, all the atoms are assumed identical but they are distinguishable. This is because the de Broglie wavelength of the atom is much smaller than the average distance between the atoms. Due to the Heisenberg uncertainty principle the position of an atom is smeared out over a distance, which is given by the de Broglie wavelength

$$\Lambda_{dB} = \frac{h}{\sqrt{2\pi m k_B T}}, \quad (1.2)$$

where  $h$  is Planck's constant,  $m$  and  $T$  are the mass and the temperature of the atom, respectively. As can be seen in equation (1.2), when the temperature decreases, the de Broglie wavelength  $\Lambda_{dB}$  increases. For very low temperatures the wavelength becomes on the order of the average distance between the atoms, and the wavepackets start to overlap. The indistinguishability of the atoms becomes important, and the (bosonic) atomic gas

is governed by Bose-Einstein statistics. At this critical temperature a phase transition occurs: All the atoms are condensed into the same quantum state and form a Bose-Einstein condensate (BEC). Since all the atoms in a BEC are described by the same quantum mechanical wave function, they behave as a single macroscopic quantum entity. This phenomenon allows us to investigate quantum mechanical effects with macroscopic entities.

The first evidence for BEC was found by F. London in the 1930s while he was investigating liquid helium. When liquid helium is cooled to a temperature lower than 2.17 K, the liquid undergoes a transition from the normal phase to the superfluid phase. This superfluidity of the liquid occurs when atoms condense to the lowest energy state. Bose-Einstein condensation can also be observed in superconducting solids. A superconductor loses its resistivity below a certain critical temperature, this disappearance of the resistance is explained in the BCS theory, developed by John Bardeen, Leon Cooper and Robert Schrieffer. In the BCS theory, Cooper pairs are formed, when two electrons close to the Fermi level couple through interactions with the crystal lattice. The Cooper pairs act like bosons and can condense into a state of zero electrical resistance. However, both systems interact strongly with their environment, thereby complicating the physics involved.

Bose-Einstein condensation in a dilute atomic gas was observed for the first time in 1995 by the groups at JILA in Boulder, Colorado (rubidium) [1], Rice University in Houston, Texas (lithium) [2] and at MIT in Cambridge, Massachusetts (sodium) [3]. In 2001, the nobel prize was given to Eric A. Cornell, Wolfgang Ketterle and Carl E. Wieman for their work on Bose-Einstein condensation.

The first condensates were created in a magnetic trap, in which only atoms in a certain  $m_F$  state can be trapped at the local minimum of the magnetic field. Nonetheless, for many experiments it is more advantageous to trap atoms independently from their magnetic moment, which can be done with optical dipole traps. The optical dipole trap is based on the interaction of inhomogeneous light fields with the induced electric dipole moment of the atoms, and was demonstrated for the first time with neutral atoms in 1986 [4]. The dipole trap can not only be used to trap atoms in different internal states, but it can also be used to trap atoms without a magnetic moment, or to trap different isotopic atoms or atomic samples simultaneously. Furthermore, the dipole trap can be overlapped with a magnetic field, to manipulate the scattering length of the atom through Feshbach resonances [5].

The first BEC in an optical dipole trap was transferred from a magnetic

---

trap into the dipole trap in 1998, but it wasn't until 2001, before a so-called all-optical BEC could be created in a dipole trap [6]. Rubidium atoms were trapped in the crossing of two CO<sub>2</sub> laser beams and evaporatively cooled down to quantum degeneracy by ramping down the laser power. Since then a variety of all-optical BECs, such as sodium [7], cesium [5] and ytterbium [8] have been prepared.

In this thesis, the preparation of a <sup>87</sup>Rb Bose-Einstein condensate in an optical dipole trap is presented. The optical dipole trap is created with an Yb:YAG laser with a wavelength  $\lambda = 1030$  nm. To our knowledge, we are the first to have reached all-optical Bose-Einstein condensation with rubidium atoms in a 1-micron laser in a simple and direct manner. In our experiment, we dispense with complex cooling techniques, like they employed in the group of D. Weiss [9]. In their experiment, they precooled rubidium atoms in an optical lattice before they loaded the atoms in a compressible crossed dipole trap. In our simple scheme, we load atoms from a magneto-optical trap directly into our dipole trap and with subsequent cooling, we reach quantum degeneracy.

Using a 1-micron laser has several advantages in respect with the CO<sub>2</sub> laser, which has a wavelength  $\lambda = 10$   $\mu$ m, since the diffraction limit of the CO<sub>2</sub> laser is much larger and therefore cannot be used in combination with the microfabricated microlenses used in our research group [10]. Another advantage is that the 1-micron laser can be used with standard optical materials, making the setup cost effective.

The Bose-Einstein condensate is the first step towards experiments where we want to investigate and exploit the wave nature of atomic matter. This particular research field is called atom optics and explores the possibility of manipulating atoms in the same way that conventional optics controls light beams. The field of atom optics started in 1929, where Stern demonstrated the reflection and diffraction of atoms from metallic and crystalline surfaces [11, 12]. However, it wasn't until the introduction of laser cooling techniques [4, 13, 14] that the field of atom optics with neutral atoms started to boom. Since then, many atom optical elements (such as lenses, mirrors, beam splitters, etc. [15]) have been created, and atom interferometers have been used to measure fundamental constants [16], atomic properties [17, 18], acceleration forces [19, 20, 21] and the rotation of the earth [22, 23, 24]. With the discovery of Bose-Einstein condensates in dilute atomic gases, the interest of atom optics nowadays lies in creating compact and reliable atom optical setups, which expands the applicability of atom optics in fundamental re-

search, and simultaneously allows the technological implementation of atom optical measurement systems. Many miniaturized atom optical setups are based on microfabricated charged and current carrying structures [25]. With these so-called atom chips, neutral atoms can be guided, trapped, manipulated [26, 27, 28], and even Bose-Einstein condensates can be created with the miniaturized setups [29, 30].

There are a number of disadvantages connected with trapping and manipulating atoms with charge or current carrying wires. The biggest disadvantage is that the atoms are trapped only a few 100  $\mu\text{m}$  away from a metallic surface. This significantly reduces the trapping and coherence times due to the coupling of atoms to fluctuating magnetic fields resulting from the roughness of the surface or the wires [31, 32]. Other disadvantages are that the optical access is limited, and the setups are relatively complex. These disadvantages can be circumvented when miniaturized and integrated atom optical setups based on microfabricated optical elements are used. Our research interest is based on loading our condensates into the micropotentials created by illuminating the microfabricated lenses with light. As the next important experiment, we want to load the condensate into a ring-shaped potential created by a microfabricated ring-lens. The ring can be used as a Sagnac interferometer.

This thesis is structured as follows: Chapter 2 explains the theory of Bose-Einstein condensation. In chapter 3, the optical dipole force is explained, which we use to create optical potentials in which we can trap atoms. For our BEC experiment we use a crossed optical dipole trap. In this trap, we capture rubidium atoms loaded directly from a magneto-optical trap (MOT). The experimental setup is explained in the second half of chapter 3. Chapter 4 demonstrates how we generate a Bose-Einstein condensate. First, the loading of atoms from the MOT into the dipole trap is explained and optimized. Then, through subsequent evaporative cooling, we cool down the atoms until we reach quantum degeneracy. Chapter 5 shows a preparatory experiment: The Bose-Einstein condensate will in the near future be loaded into the ring-shaped potential. Due to the tight trapping frequencies, the BEC might become a 1D BEC or a Tonks-Girardeau gas, depending on the density.

## 2. BOSE-EINSTEIN CONDENSATION

Bose-Einstein condensation is based on the indistinguishability and wave nature of particles. In a very simple description, atoms are depicted as quantum mechanical wavepackets with an expansion on the order of the thermal de Broglie wavelength:

$$\Lambda_{dB} = \sqrt{\frac{2\pi\hbar^2}{mk_B T}}, \quad (2.1)$$

where  $m$  and  $T$  are the mass and the temperature of the atom. As the atoms are cooled down, the de Broglie wavelength increases. When the atoms are cooled down to a temperature for which the de Broglie wavelength equals the mean distance between the atoms, the wavepackets start to overlap and the indistinguishability of the particles becomes important. Depending on whether the particles are fermions (particles with half-integer spin) or bosons (particles with integer spin), they behave differently and obey Fermi-Dirac or Bose-Einstein statistics, respectively. As the gas is cooled down to quantum degeneracy, bosons condense into the ground state of the system, and form a Bose-Einstein condensate (BEC), whereas fermions fill up the lowest lying energy states of the system, where each quantum mechanical state is occupied by only one fermion, forming a Fermi sea. The formation of a BEC is depicted in figure 2.1.

As the theory of Bose-Einstein condensation has been explained in many textbooks, this chapter will only summarize the main findings that are important for this thesis. More literature can be found in [33, 34, 35].

### 2.1 *The Non-Interacting Bose Gas*

#### 2.1.1 *The Thermodynamic Limit*

For trapped non-interacting bosonic atoms in thermal equilibrium, the mean occupation number for a given quantum state  $\nu$  is given by the Bose distri-

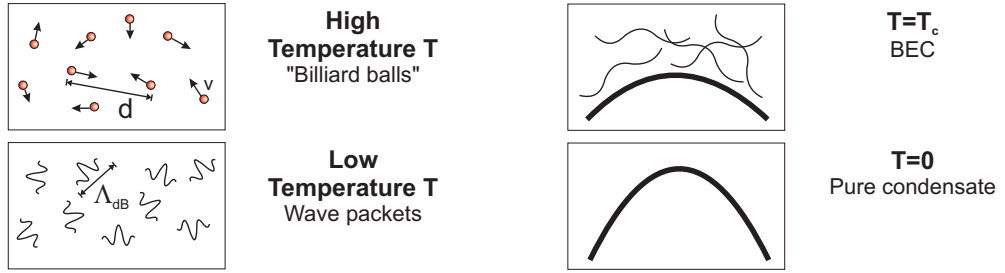


Fig. 2.1: Bose-Einstein condensation. At high temperatures, the atoms can be described by Maxwell-Boltzmann statistics just as well as by quantum statistics. As the temperature is lowered, the de Broglie wavelength of the atoms become larger, until the de Broglie waves start to overlap and the atoms condense into the ground state.

bution function:

$$f(\epsilon_\nu) = \frac{1}{e^{(\epsilon_\nu - \mu)/k_B T} - 1}, \quad (2.2)$$

where  $\epsilon_\nu$  is the energy of the respective state and  $\mu$  is the chemical potential. The chemical potential is determined by the condition that the sum of the occupancies of the individual levels must be equal to the total number of atoms:  $N = \sum_\nu f(\epsilon_\nu)$ . The mean occupation number of the ground state is much smaller than 1 for high temperatures. The chemical potential  $\mu$  is therefore smaller than the energy of the lowest energy state  $\epsilon_0$ . When the temperature is lowered, the occupancy in the lowest energy state increases, and the chemical potential also increases. The total number of atoms can be split into the total number of atoms in the ground state  $N_0$  and the total number of atoms in excited states  $N_{ex}$ . When the chemical potential  $\mu$  approaches the energy of the ground state  $\epsilon_0$ , the number of atoms in the ground state becomes macroscopic, thus approaching the total number of atoms of the system. The total atom number is given by:

$$N = N_0 + N_{ex} = N_0 + \sum_{\nu \neq 0} \frac{1}{e^{(\epsilon_\nu - \epsilon_0)/k_B T} - 1}. \quad (2.3)$$

A macroscopic number of atoms is in the ground state, as soon as the excited atom number  $N_{ex}$  falls below the total atom number  $N$ . This describes the effect of Bose-Einstein condensation. The highest temperature for which a BEC exists is referred to as the transition temperature and is denoted by

$T_c$ . This critical temperature  $T_c$  can also be defined as being the lowest temperature for which all the atoms are still in excited states ( $N_0 \ll N$ ). The critical temperature can then be determined from equation 2.3. Here we do this for the case of a harmonic trap as it is used in the work described in this thesis. Therefore, we replace the sum over the states by an integral over the energy density of states, and use the density of states for a harmonic potential  $g(\epsilon) = \frac{\epsilon^2}{2\hbar^3\bar{\omega}^3}$ , and obtain:

$$N_{ex} = \int_0^\infty d\epsilon \frac{\epsilon^2}{2\hbar^3\bar{\omega}^3(e^{(\epsilon-\epsilon_0)/k_B T} - 1)}. \quad (2.4)$$

Evaluating the integral and setting  $N_{ex} = N$  yields for the critical temperature:

$$k_B T_c = \hbar\bar{\omega} \left( \frac{N}{\zeta(3)} \right)^{1/3}, \quad (2.5)$$

where  $\bar{\omega} = (\omega_x\omega_y\omega_z)^{1/3}$  is the geometric mean of the oscillator frequencies of the three-dimensional harmonic potential

$$V(r) = \frac{1}{2}m(\omega_x^2 x^2 + \omega_y^2 y^2 + \omega_z^2 z^2), \quad (2.6)$$

and  $\zeta(\alpha) = \sum_{n=1}^\infty n^{-\alpha}$  is the Riemann zeta function with  $\zeta(3) \approx 1.202$ . The equation shows that for tighter confinement of atoms in a trap and/or larger atom numbers, Bose-Einstein condensation happens at higher temperatures. The fraction of condensed atoms in the trap can be calculated from equation 2.3 as well, giving

$$\frac{N_0}{N} = 1 - \left( \frac{T}{T_c} \right)^3. \quad (2.7)$$

The onset of Bose-Einstein condensation can be determined from the phase space density. The phase space density is the spatial density of the atoms multiplied with the density of one atom in momentum space:

$$\rho_{psd} = n\Lambda_{dB}^3. \quad (2.8)$$

The density consists of the condensate density and the thermal density  $n = n_0(\vec{r}) + n_T(\vec{r})$ . The thermal density is given by the integral over momentum space [35]

$$\begin{aligned} n_T(\vec{r}) &= \int d\vec{p} \frac{1}{(2\pi\hbar)^3} \frac{1}{e^{(V(\vec{r})-\mu)/k_B T} - 1} \\ &= \frac{1}{\Lambda_{dB}^3} g_{3/2}(e^{-(V(\vec{r})-\mu)/k_B T}), \end{aligned} \quad (2.9)$$

with the Bose function  $g_\alpha(x) = \sum_{n=1}^{\infty} \frac{x^n}{n^\alpha}$ . Independent of the trap geometry, at  $T = T_c$ , the chemical potential fulfills  $\mu \approx U(\vec{r})$  and Bose-Einstein condensation occurs, when in the center of the trap the phase space density attains the value

$$\rho_{psd}(0) = n_T(0)\Lambda_{dB}^3(T_c)g_{3/2}(1) = g_{3/2}(1) \approx 2.612. \quad (2.10)$$

In the above analysis, the semiclassical approximation was used, where it was assumed that the atom number goes to infinity. The semiclassical approximation makes use of a continuous level structure instead of a discrete level structure. This is only valid when  $k_B T_c$  is much larger than the energy level spacing  $\hbar\bar{\omega}$ . Equation 2.5 shows that  $k_B T_c$  can indeed be much larger than  $\hbar\bar{\omega}$ . In BECs of a few thousand to several million atoms, the transition temperature is  $\sim 20 - 200$  times larger than the energy level spacing  $\hbar\bar{\omega}$ , thus the semiclassical approximation is a good description of the condensate.

### 2.1.2 The Finite Size Effect

In reality, the thermodynamic limit is never reached, because the number of atoms that can be trapped and condensed is not infinite. Therefore, Bose-Einstein condensation is not exactly a phase transition, however the macroscopic occupation of the lowest energy level still happens rather abruptly as the temperature is lowered. To calculate corrections due to the finite atom number for a non-interacting Bose gas, one can calculate the summation  $N = \sum_{\nu} f(\epsilon_{\nu})$  for a finite number of atoms numerically, as is given in reference [36]. The results of reference [36] are shown in figure 2.2(a), where it is demonstrated that there is only a small difference between the thermodynamic limit and taking into account the finite size of the gas. The condensate fraction calculated numerically is smaller than in the thermodynamic limit, and near the phase transition, the onset of BEC is not sudden, but is slightly rounded off.

A correction to equation 2.7 has been determined in reference [37]:

$$\frac{N_0}{N} = 1 - \left(\frac{T}{T_c}\right)^3 - \frac{3\omega_m\zeta(2)}{2\bar{\omega}(\zeta(3))^{2/3}} \left(\frac{T}{T_c}\right)^2 N^{-1/3}, \quad (2.11)$$

where  $\omega_m = (\omega_x + \omega_y + \omega_z)/3$  is the algebraic mean of the frequencies. It fits perfectly to the numeric calculations of [36], except for a narrow region around the critical temperature, where higher orders should be taken into

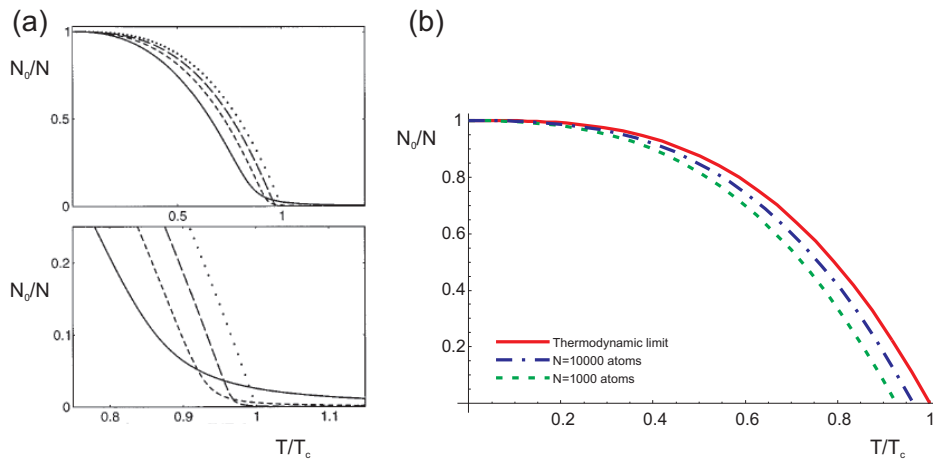


*Fig. 2.2:* (a) Figure taken from reference [36]. It shows the numerically calculated condensate fraction for a finite number of atoms in a three-dimensional harmonic potential versus the temperature. The plots are for  $N = 100$  atoms (solid line),  $N = 1,000$  (short dashes),  $N = 10,000$  (long dashes) and  $N = \infty$  atoms (dots). The lower graph is an enlargement of the region around  $T = T_c$ . (b) The graph shows the condensate fraction as a function of the temperature according to equation 2.11, calculated for the potential used in our experiments (section 4.5).

account [35]. Figure 2.2(b) shows the condensate fraction calculated with equation 2.11 for the potential used in our experiments (section 4.5), together with the result from the thermodynamic limit. As can be seen in the graph, equation 2.11 does not take the "rounding effect" near the critical temperature into account. Nevertheless, the condensate fraction for temperatures lower than the critical temperature can be calculated from this equation. Using equation 2.7 to calculate the condensate fraction leads to an error of approximately 7% for a Bose gas consisting of 1,000 atoms. Equation 2.7 becomes more accurate for higher atom numbers, for a Bose gas consisting of 10,000 atoms, the deviation is only 3%.

Not only the condensate fraction is lowered by the finite size of the Bose gas, the critical temperature is also lower than the critical temperature given by equation 2.5. The shift in the critical temperature can be estimated by setting the condensate fraction in equation 2.11 to zero:

$$\frac{\delta T_c}{T_c} = -\frac{\omega_m \zeta(2)}{2\bar{\omega}(\zeta(3))^{2/3}} N^{-1/3} \simeq -0.73 \frac{\omega_m}{\bar{\omega}} N^{-1/3}. \quad (2.12)$$

For a gas with 1,000 atoms, the transition temperature is lowered by 7% compared to the critical temperature calculated with equation 2.5. The finite size effect can be measured in current experiments. Equation 2.7 still describes the condensate fraction quite well, as long as the correction to the critical temperature, given by equation 2.12, is used in the calculations:  $T_c \rightarrow T_c + \delta T_c$ .

### 2.1.3 Interacting Atoms

Although BEC is easily achieved in dilute gases ( $na^3 \ll 1$ ), where the interactions between the atoms are low, they cannot be neglected. The effect of repulsive interactions is that it expands the atomic cloud, thus decreasing the density and lowering the critical temperature. The opposite happens for attractive interactions: The atomic cloud is compressed, leading to an increase in the density and a higher critical temperature. The shift in the critical temperature can be determined using the Hartree-Fock approximation [35, 34], where it is assumed that the atoms are non-interacting bosons moving in a self-consistent mean field. The shift is given by:

$$\frac{\delta T_c}{T_c} = -1.3 \frac{a}{a_{ho}} N^{1/6}, \quad (2.13)$$

$a$  is the s-wave scattering length, which is the dominating scattering process at low temperatures. The harmonic oscillator length  $a_{ho}$  is given by:

$$a_{ho} = \left( \frac{\hbar}{m\bar{\omega}} \right)^{1/2}. \quad (2.14)$$

Equation 2.13 shows that the critical temperature shifts proportionally to the scattering length. The shift is negative for repulsive interactions, where the scattering length is positive ( $a = 110a_0$  for rubidium [38]). The shift induced by the interactions is of the same order as the shift due to the finite number. However, the shift due to the finite number disappears for high atom numbers, whereas the shift due to the interactions cannot be ignored and even increases for higher atom numbers. Attractive interactions induce a positive shift of the critical temperature. In this case, the shift due to the finite size of the cloud cannot be overlooked, since the number of atoms has to be small to prevent the effect of collapse of the condensate.

Similarly, the condensate fraction is also effected by the interactions. An expression is given in reference [39]:

$$\frac{N_0}{N} = 1 - \left( \frac{T}{T_c} \right)^3 - \frac{\zeta(2)}{\zeta(3)} a \left( N^{1/6} \frac{a}{a_{ho}} \right)^{2/5} \left( \frac{T}{T_c} \right)^2 \left( 1 - \left( \frac{T}{T_c} \right)^3 \right)^{2/5}. \quad (2.15)$$

The decrease of the condensate fraction is only due to interactions within the condensate, since the thermal cloud and the condensate are spatially separated from one another.

The corrections in critical temperature and condensate fraction due to finite size and interaction effects described above can be measured in BEC experiments, but they are small, usually in the order of a few percent. Therefore, most of the experiments described in this thesis can still be well understood quantitatively when the corrections are neglected, and the equations describing the critical temperature and the condensate fraction in the thermodynamic limit (Eqs. 2.5 and 2.7) are used.

## 2.2 The Wave Function of the Condensate

### 2.2.1 An Ideal Bose Gas

A gas with  $N$  noninteracting atoms can be described by a simple Schrödinger equation for the single particle Hamiltonian

$$H = -\frac{\hbar^2}{2m}\nabla^2 + V_{ext}(\vec{r}). \quad (2.16)$$

The eigenvalues of the Hamiltonian are

$$\epsilon_{n_x n_y n_z} = \left(n_x + \frac{1}{2}\right)\hbar\omega_x + \left(n_y + \frac{1}{2}\right)\hbar\omega_y + \left(n_z + \frac{1}{2}\right)\hbar\omega_z. \quad (2.17)$$

The ground state function  $\phi(\vec{r}_1, \dots, \vec{r}_N)$  of  $N$  noninteracting bosons trapped in a harmonic potential (Eq. 2.6) is just the product of the single particle ground state wave function  $\phi_0(\vec{r})$

$$\phi(\vec{r}_1, \dots, \vec{r}_N) = \prod_i^N \phi_0(\vec{r}_i), \quad (2.18)$$

with

$$\phi_0(\vec{r}) = \left(\frac{m\bar{\omega}}{\pi\hbar}\right)^{3/4} e^{-\frac{m}{2\hbar}(\omega_x x^2 + \omega_y y^2 + \omega_z z^2)}. \quad (2.19)$$

The density of the condensate is given by:

$$n_0(\vec{r}) = N|\phi_0(\vec{r})|^2, \quad (2.20)$$

and increases with increasing  $N$ . The density distribution is anisotropic if the three frequencies  $\omega_x, \omega_y$ , and  $\omega_z$  are not equal. The size  $a_i$  in dimension  $i$  of the cloud does not depend on the number of atoms and shows the anisotropy due to its dependence on the trap frequencies:

$$a_i = \sqrt{\frac{\hbar}{m\omega_i}}, \quad \text{with } i = x, y, z. \quad (2.21)$$

The aspect ratio is then proportional to the root of the reciprocal ratio of the trap frequencies:

$$\frac{a_i}{a_j} = \sqrt{\frac{\omega_j}{\omega_i}}, \quad \text{with } i, j = x, y, z. \quad (2.22)$$

When the atom cloud is allowed to expand, the distribution of the atoms does not only depend on the initial density distribution, but also on the initial velocity distribution. According to Heisenberg's uncertainty principle, a narrow spatial distribution implies a broad momentum distribution, and conversely. The ratio of the momentum widths is then:

$$\sqrt{\frac{\omega_i}{\omega_j}}, \text{ with } i, j = x, y, z. \quad (2.23)$$

This result can also be found by taking the Fourier transform of the ground state wave function (Eq. 2.19).

At temperatures well above the critical temperature, the density of the cloud can be approximated by a Maxwell-Boltzmann distribution  $n(\vec{r}) \propto e^{-V_{ext}(\vec{r})/k_B T}$ . In a harmonic trap, the thermal widths are given by:

$$r_i = \sqrt{\frac{2k_B T}{m\omega_i^2}}, \text{ with } i = x, y, z. \quad (2.24)$$

The size of the thermal cloud is much larger than the size of the condensate under normal experimental conditions ( $k_B T \gg \hbar\bar{\omega}$ ). As a consequence, the condensate appears as a narrow peak in the spatial distribution at temperatures below the critical temperature.

Above the critical temperature, the momentum distribution only depends on the temperature and the mass of the atoms in the cloud. Maxwell-Boltzmann statistics can be applied again, leading to a density in momentum space  $n(\vec{p}) \propto e^{-p^2/2mk_B T}$ . The distribution is isotropic, and a thermal cloud will be spherically symmetric after a long enough free expansion time, whereas a condensate will be anisotropic after its expansion, given an anisotropic confining potential. The occurrence of anisotropy in condensate expansion can be used as proof for condensation, and has been recognized as an important signature of BEC from the very beginning [1, 3, 40].

### 2.2.2 Taking Interactions into Account

Interactions between the atoms cannot be ignored, since the interactions alter the size and the form of the cloud: Repulsive interactions expand the condensate, whereas attractive interactions can lead to a collapse of the condensate. Furthermore, when the condensate is allowed to expand freely, the interaction energy of the atoms is transformed into kinetic energy, thereby

changing the momentum distribution.

The many-body Hamiltonian describing  $N$  interacting atoms in a harmonic potential (Eq. 2.6) is given by:

$$\begin{aligned} \hat{H} = & \int d\vec{r} \hat{\Psi}^\dagger(\vec{r}) \left[ -\frac{\hbar^2}{2m} \nabla^2 + V_{ext}(\vec{r}) \right] \hat{\Psi}(\vec{r}) \\ & + \frac{1}{2} \int d\vec{r} d\vec{r}' \hat{\Psi}^\dagger(\vec{r}) \hat{\Psi}^\dagger(\vec{r}') V(\vec{r} - \vec{r}') \hat{\Psi}(\vec{r}') \hat{\Psi}(\vec{r}), \end{aligned} \quad (2.25)$$

where  $\hat{\Psi}(\vec{r})$  and  $\hat{\Psi}^\dagger(\vec{r})$  are the boson field operators, that annihilate respectively create a particle at the position  $\vec{r}$ , and  $V(\vec{r} - \vec{r}')$  is the interatomic two-body potential accounting for the interactions. The equation of motion is given by the Schrödinger equation in operator form  $i\hbar \frac{\partial}{\partial t} \hat{\Psi} = \hat{H} \hat{\Psi}$ :

$$i\hbar \frac{\partial}{\partial t} \hat{\Psi}(\vec{r}, t) = \left[ -\frac{\hbar^2 \nabla^2}{2m} + V_{ext}(\vec{r}) + \int d\vec{r}' \hat{\Psi}^\dagger(\vec{r}', t) V(\vec{r} - \vec{r}') \hat{\Psi}(\vec{r}', t) \right] \hat{\Psi}(\vec{r}, t). \quad (2.26)$$

The solution of the equation of motion entails all the interesting properties of the Bose gas, but is too complicated and a complete solution is not possible.

### *The Gross-Pitaevskii Equation*

In order to avoid solving the complete Schrödinger equation, mean field approaches have been developed. One approach was developed by Bogoliubov in 1947 [41], and consisted in separating the contribution of the condensate from the Boson field operators. In general, the Boson field operator is given by  $\hat{\Psi}(\vec{r}) = \sum_{\alpha} \Psi_{\alpha}(\vec{r}) a_{\alpha}$ , where  $\Psi_{\alpha}(\vec{r})$  are the single particle wave functions and  $a_{\alpha}$  are the corresponding annihilation operators. As shown before, Bose-Einstein condensation occurs when the ground state is macroscopically occupied. This is accompanied by an abrupt change of the macroscopic properties of the condensate of the Bose gas (such as the specific heat) at the transition point, and thus it can be said that the phase transition is a second order phase transition (this is similar to spontaneous symmetry breaking) [42]. The system below the critical temperature is therefore characterized by a so-called order parameter, which vanishes for temperatures above the critical temperature. In our case, this is the condensate wave function. The Boson field operator can then be split in two parts:

$$\hat{\Psi}(\vec{r}, t) = \langle \hat{\Phi}(\vec{r}, t) \rangle + \hat{\Psi}'(\vec{r}, t), \quad (2.27)$$

where the first parameter  $\langle \hat{\Phi}(\vec{r}, t) \rangle \equiv \Phi(\vec{r}, t)$  is the condensate wave function, and is responsible for the creation and annihilation of condensed particles. The operators  $a_\alpha$  can be neglected in the thermodynamic limit. The second parameter  $\hat{\Psi}'(\vec{r}, t)$  describes excitations of the Bose gas.

In quantum degenerate dilute Bose gases, the de Broglie wavelength is much larger than the interatomic distance. In this case, the interaction potential  $V(\vec{r} - \vec{r}')$  can be well approximated by a so-called zero range potential (or also pseudopotential)  $g\delta(\vec{r} - \vec{r}')$  [43]. The coupling constant  $g$  is related to the scattering length  $a$  by:

$$g = \frac{4\pi\hbar^2 a}{m} \quad (2.28)$$

Putting this in equation 2.26, and exchanging the Boson field operator  $\hat{\Psi}(\vec{r}, t)$  with the condensate wave function  $\Phi$ , since the occupation of higher energy levels can be neglected for low temperatures  $T \ll T_c$ , we get:

$$i\hbar \frac{\partial}{\partial t} \Phi(\vec{r}, t) = \left[ -\frac{\hbar^2 \nabla^2}{2m} + V_{ext}(\vec{r}) + g|\Phi(\vec{r}, t)|^2 \right] \Phi(\vec{r}, t). \quad (2.29)$$

This is the so-called Gross-Pitaevskii equation, which has been derived independently by Gross and Pitaevskii in 1961 [44, 45]. The equation shows that the interaction leads to an effective potential  $g|\Phi(\vec{r}, t)|^2$ , which is proportional to the density, acting on a particle. Since the density is always positive, the sign of the potential energy is determined by the scattering length  $a$ . If the scattering length is positive, then the potential energy increases with the density, and the interaction is repulsive. If the scattering length is negative, it is favourable for a homogeneous gas to shrink to a smaller volume, and can lead to the phenomenon of collapse of the condensate.

The order parameter  $\Phi$  is substituted with  $\phi e^{-i\mu t}$ , where  $\mu$  is the chemical potential and  $\phi$  is normalized to the total number of atoms  $N$ :  $\int d\vec{r} \phi^2 = N$ , to obtain the time independent Gross-Pitaevskii equation:

$$\mu\phi(\vec{r}) = \left[ -\frac{\hbar^2 \nabla^2}{2m} + V_{ext}(\vec{r}) + g\phi^2(\vec{r}) \right] \phi(\vec{r}). \quad (2.30)$$

This equation can be interpreted as a nonlinear Schrödinger equation with the mean field potential  $g\phi^2(\vec{r})$  as a nonlinear term, which is proportional to the density  $n = \phi^2(\vec{r})$ . The equation reduces to the single particle Hamiltonian (Eq. 2.16), when there are no interactions between the atoms ( $g = 0$ ).

The energy of the condensate may be expressed by the energy functional [34]:

$$E[\Phi] = \int d\vec{r} \left[ \frac{\hbar^2}{2m} |\nabla\Phi|^2 + V_{ext}(\vec{r})|\Phi|^2 + \frac{g}{2} |\Phi|^4 \right]. \quad (2.31)$$

The factor  $\frac{1}{2}$  comes from the fact that two bosons are needed for the interaction. Inserting the solution of the Gross-Pitaevskii equation for the ground state  $n = \phi^2(\vec{r})$  in the energy function gives:

$$\begin{aligned} E[n] &= \int d\vec{r} \left[ \frac{\hbar^2}{2m} |\nabla\sqrt{n}|^2 + nV_{ext}(\vec{r}) + \frac{gn^2}{2} \right] \\ &= E_{kin} + E_{ho} + E_{int}. \end{aligned} \quad (2.32)$$

The first term is the kinetic energy of the condensate  $E_{kin}$  and is also called the ‘quantum pressure’. This term vanishes for uniform systems. The second term is the harmonic oscillator energy  $E_{ho}$ , and the third term is the mean field interaction energy  $E_{int}$ . When the (harmonic) trap is suddenly turned off, the harmonic oscillator energy term disappears, and the kinetic energy of the condensate and the interaction energy are converted in kinetic energy of motion. The release energy  $E_{rel} = E_{kin} + E_{int}$  depends on the number of atoms  $N$ , which means that the more atoms, the greater the release energy per atom.

An important length scale called the healing length  $\xi$  can be found, when the two energies  $E_{kin}$  and  $E_{int}$  are equated. The healing length is the minimum distance over which the order parameter can heal, i.e. over which it can balance density fluctuations. The smallest distance necessary for the density of the condensate to grow from 0 to  $n$  is given by:

$$\xi = \frac{1}{\sqrt{8\pi na}}. \quad (2.33)$$

The healing length is important for superfluid effects, such as vortices, where the size of the core of the vortex is given by the healing length.

### *The Thomas-Fermi Approximation*

For large condensates with large atom numbers, the repulsive interactions lead to a lower density in the cloud, since the atoms are pushed outwards. As a consequence, the quantum pressure has a smaller influence and only contributes near the boundary surface of the condensate. Compared to the

interaction energy, it can therefore be ignored. With this approximation, the time independent Gross-Pitaevskii equation (Eq. 2.30) becomes:

$$\mu\phi(\vec{r}) = [V_{ext}(\vec{r}) + g\phi^2(\vec{r})] \phi(\vec{r}). \quad (2.34)$$

This is referred to as the Thomas-Fermi approximation, and gives the solution

$$n(\vec{r}) = \phi^2(\vec{r}) = \frac{[\mu - V_{ext}(\vec{r})]}{g} \quad (2.35)$$

in the region where  $\mu > V_{ext}(\vec{r})$ , and  $n(\vec{r}) = 0$  outside this region. This means that the boundary of the cloud is given by the chemical potential  $V_{ext}(\vec{r}) = \mu$ . The normalisation condition  $N = \int d\vec{r}n(\vec{r})$  defines the chemical potential as a function of the atom number:

$$\mu = \frac{\hbar\bar{\omega}}{2} \left( \frac{15Na}{a_{ho}} \right)^{2/5}. \quad (2.36)$$

Since  $\mu = \frac{\partial E}{\partial N}$ , the total energy per particle can be obtained from equation 2.36:

$$\frac{E}{N} = \frac{5}{7}\mu. \quad (2.37)$$

This energy splits into the potential energy  $E_{ho}$  and the interaction energy  $E_{int}$ . The ratio between these two energies can be found by inserting the solution attained from the Thomas-Fermi approximation (Eq. 2.35) into equation 2.31, whereby the kinetic energy of the condensate is neglected. Thus

$$\frac{E_{int}}{E_{ho}} = \frac{2}{3} \quad (2.38)$$

is obtained. The interaction energy per atom is then

$$\frac{E_{int}}{N} = \frac{2}{7}\mu. \quad (2.39)$$

As mentioned before, the boundary of the cloud is given by the chemical potential  $V_{ext}(\vec{r}) = \mu$ . From this relation, the size of the condensate can be determined. Using a harmonic trap, the size  $R_i$  of the condensate becomes:

$$R_i = a_{ho} \frac{\bar{\omega}}{\omega_i} \left( \frac{15Na}{a_{ho}} \right)^{1/5}, \quad \text{with } i = x, y, z. \quad (2.40)$$

The size of the condensate grows with the number of atoms. The aspect ratio is given by the inverse ratio of the trap frequencies:

$$\frac{R_i}{R_j} = \frac{\omega_j}{\omega_i}, \text{ with } i, j = x, y, z. \quad (2.41)$$

As has been shown for a condensate without interatomic interactions, the expansion of the cloud is anisotropic, if the trap is anisotropic. When the interactions are included, all the interaction energy is transformed into kinetic energy upon release, and anisotropy is thereby further increased. In axially symmetric traps, where the radial confinement is much tighter than the axial confinement ( $\omega_{radial} > \omega_{axial}$ ), the interaction energy is mainly changed into kinetic energy in the radial direction, since the interaction force

$$F_{int} = -\nabla E_{int} = -g\nabla n \quad (2.42)$$

is much larger in the radial direction than in the axial direction. This means that the cloud expands faster in the radial direction than in the axial direction, forming an ellipsoid with  $R_{radial} > R_{axial}$  for long expansion times.

It should be noted that the Thomas-Fermi approximation can only be applied, when the order parameter  $\Phi$  varies slowly. Therefore, the approximation fails near the cloud surface, which becomes important for when e.g. vortices are studied.

In this thesis, the creation of a Bose-Einstein condensate in an optical dipole trap is described. In the dipole trap, we evaporatively cool the atoms down to quantum degeneracy. At the end of the evaporation cycle, we typically have  $\sim 10,000$  atoms at a temperature below the critical temperature  $T_c$ . We assume that in our small trap the density is so high that the influence of the repulsive interactions is much larger than the quantum pressure. Therefore, all the physics necessary to describe the condensate is contained in the Thomas-Fermi approximation.

## 3. TRAPPING ATOMS IN OPTICAL DIPOLE TRAPS

### *Overview of this chapter*

In this chapter, the theory behind trapping atoms in an optical dipole trap is explained. Section 3.1 explains the theory of the optical dipole potential. In our experiments, neutral rubidium atoms are trapped in the crossing point of two laser beams. How we trap atoms in the focus of a laser beam is explained in section 3.2. The atoms are loaded straight from a magneto-optical trap into the dipole trap, after which the atoms are evaporatively cooled. The experimental setup used to cool and trap atoms in the magneto-optical trap and subsequently in the dipole trap is described in section 3.3.

### *3.1 The Optical Dipole Potential*

The experiments described in this thesis use the dipole force to trap rubidium atoms and cool them down to nanokelvin temperatures. An atom placed in a laser field experiences two kinds of forces: A dipole force and a scattering force, also called radiation force. The scattering force originates from the momentum  $p$  associated with light: Each photon does not only carry energy  $E = \hbar\omega$ , but also momentum  $p = \hbar k$  with  $k = 2\pi/\lambda$ , and angular momentum  $\hbar$ . An atom absorbing a photon stores the energy by going into an excited state, and it conserves the momentum by changing its velocity with the amount  $v_R = \hbar k/m$ , where  $m$  is the mass of the atom. At a later time, the atom de-excites by emitting a photon in a random direction. Over many absorptions and emissions, the recoil energy of the de-exciting atom averages to zero. This can lead to a big velocity change, when the atom only absorbs photons coming from one direction (see also section 3.3.2).

The dipole force results from the dispersive interaction of an induced atomic dipole moment with a gradient in the intensity of a laser beam.

The dipole force was first exploited in 1970 to manipulate micron-sized

particles [46]. It was demonstrated that the dipole force could be used to displace and levitate dielectric particles in both water and air. This work led to the development of the optical dipole trap, which was first demonstrated in 1986. In two separate experiments, it was shown that not only dielectric particles could be trapped in the focus of a single laser beam [47], but also neutral atoms [4].

The theory of the optical dipole force is explained in this section, starting with the classical oscillator model. An outstanding review article about trapping neutral atoms in optical dipole traps can be found in [48].

### 3.1.1 The Classical Oscillator Model

In the following, we assume the atom is a pure two-level system. In the classical picture the atom is a harmonic oscillator, which is coupled to an external electromagnetic field  $\vec{E}(\vec{r}, t) = \epsilon E(\vec{r})e^{-i\omega t} + c.c.$  through its induced dipole moment  $\vec{p} = \epsilon p(\vec{r})e^{-i\omega t} + c.c.$ . The dipole moment  $\vec{p}$  oscillates in the direction of the unit polarisation vector  $\epsilon$  with the driving frequency  $\omega$ . The amplitude of the dipole moment  $p(\vec{r})$  is related to the amplitude of the electric field  $E(\vec{r})$  by

$$p(\vec{r}) = \alpha(\omega)E(\vec{r}), \quad (3.1)$$

where  $\alpha(\omega)$  is the complex polarisability. The dipole potential is calculated by taking the temporal average of the interaction energy

$$U_{Dip} = -\frac{1}{2}\langle \vec{p}\vec{E} \rangle = -\frac{1}{2\epsilon_0 c} \text{Re}(\alpha)I(\vec{r}). \quad (3.2)$$

The factor  $\frac{1}{2}$  comes from the fact that the dipole moment is induced. The power absorbed from the electromagnetic field can be calculated in a similar way

$$P_{abs} = \langle \dot{\vec{p}}\vec{E} \rangle = \frac{\omega}{\epsilon_0 c} \text{Im}(\alpha)I(\vec{r}). \quad (3.3)$$

The scattering rate can be deduced from the absorbed power, by assuming that the absorbed power is a photon scattering process where the atom absorbs light and reemits the light by subsequent spontaneous emission. The scattering rate is therefore

$$\Gamma_{Scat} = \frac{P_{abs}}{\hbar\omega} = \frac{1}{\hbar\epsilon_0 c} \text{Im}(\alpha)I(\vec{r}). \quad (3.4)$$

The real part of the polarisability describes the in-phase oscillation responsible for the dispersive nature of the interaction, the imaginary part describes the out-of-phase component of the oscillation and is responsible for the absorption. When we look at the dipole force ( $\vec{F}_{Dip} = -\nabla U_{Dip}$ ) we see that it is proportional to the real part of the polarisability

$$\vec{F}_{Dip} = \frac{1}{2\epsilon_0 c} Re(\alpha) \nabla I(\vec{r}) \quad (3.5)$$

thus the dipole force  $\vec{F}_{Dip}$  is a conservative force, whose strength is proportional to the intensity gradient of the driving field. The polarisability is calculated by considering Lorentz's model of the harmonic oscillator, in which an electron is elastically bound to the core with an oscillation eigenfrequency  $\omega_0$ , which is the optical transition frequency of the two-level atom. The dipole radiation is responsible for the damping according to Larmor's formula for the power radiated by an accelerated charge. From the equation of motion  $\ddot{x} + \Gamma_\omega \dot{x} + \omega_0^2 x = -\frac{eE(t)}{m_e}$  we get

$$\alpha = \frac{e^2}{m_e} \frac{1}{\omega_0^2 - \omega^2 - i\omega\Gamma_\omega}. \quad (3.6)$$

$\Gamma_\omega$  is the classical damping rate due to the radiative energy loss, given by

$$\Gamma_\omega = \frac{e^2 \omega^2}{6\pi\epsilon_0 m_e c^3}. \quad (3.7)$$

Putting equations 3.6 and 3.7 into equations 3.2 and 3.4 and using the on-resonance damping rate  $\Gamma \equiv \Gamma_{\omega_0} = (\omega_0/\omega)^2 \Gamma_\omega$ , we get for the dipole potential

$$U_{Dip}(\vec{r}) = -\frac{3\pi c^2}{2\omega_0^3} \left( \frac{\Gamma}{\omega_0 - \omega} + \frac{\Gamma}{\omega_0 + \omega} \right) I(\vec{r}) \quad (3.8)$$

and for the scattering rate

$$\Gamma_{Scat}(\vec{r}) = \frac{3\pi c^2}{2\hbar\omega_0^3} \left( \frac{\omega}{\omega_0} \right)^3 \left( \frac{\Gamma}{\omega_0 - \omega} + \frac{\Gamma}{\omega_0 + \omega} \right)^2 I(\vec{r}). \quad (3.9)$$

For small detunings  $\Delta \equiv \omega_0 - \omega$ , where  $|\Delta| \ll \omega_0$ , the counter-rotating term can be neglected in the so-called rotating-wave-approximation. The general expression for the dipole potential and the scattering rate then simplify to

$$U_{Dip}(\vec{r}) = \frac{3\pi c^2}{2\omega_0^3} \frac{\Gamma}{\Delta} I(\vec{r}), \quad (3.10)$$

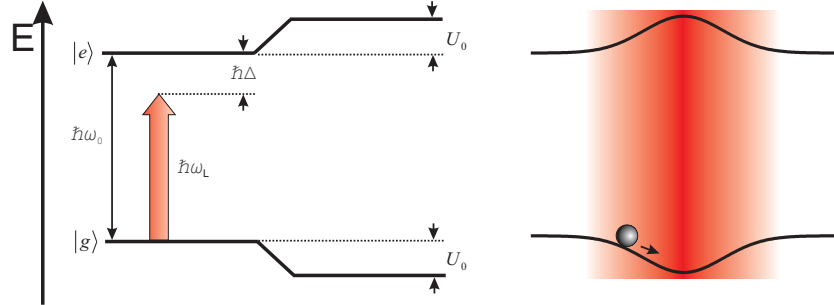


Fig. 3.1: Light shifts for a two-level atom. Left: For a red detuned laser beam,  $\Delta < 0$ , the light shift of the ground state is negative, whereas the light shift of the excited state is positive. Right: The light shift is proportional to the intensity of the applied field, therefore a spatially inhomogeneous field (e.g. a Gaussian laser beam) creates a ground state potential well, in which the atom can be trapped.

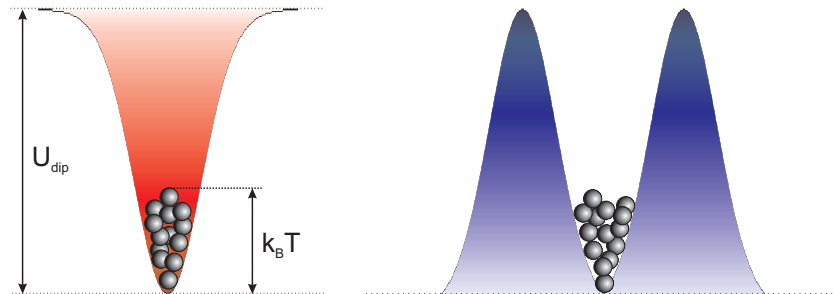


Fig. 3.2: Dipole potentials for red ( $\Delta < 0$ ), respectively blue ( $\Delta > 0$ ) detuned laser beams. The blue detuned case requires  $e^2$  times more laser power or a smaller detuning to achieve the same potential depth, since the atoms are repelled from the light.

$$\Gamma_{Scat}(\vec{r}) = \frac{3\pi c^2}{2\hbar\omega_0^3} \left(\frac{\Gamma}{\Delta}\right)^2 I(\vec{r}). \quad (3.11)$$

From equation 3.10 it is clear that when the laser field interacting with the atom is red detuned from the atomic transition ( $\Delta < 0$ ), a negative potential is created and the atom is attracted to higher intensities. Therefore, a very simple and effective way to trap atoms in a dipole trap is to use a focussed Gaussian laser beam (Fig. 3.1). As the scattering rate scales with a factor  $I/\Delta^2$  and the dipole potential with only a factor  $I/\Delta$ , the scattering rate of a red detuned laser beam can be kept as low as possible by using very large detunings and high intensities, assuring longer lifetimes of atoms in the trap.

Atoms are repelled from the light when the laser is blue detuned ( $\Delta > 0$ ). Trapping atoms with blue detuned laser is possible by using a Laguerre-Gaussian mode, also called doughnut mode. Figure 3.2 shows two dipole trap configurations.

### 3.1.2 The Semi-Classical Model

In this approach, the atom is also considered a pure two-level system which interacts with the electromagnetic field. When saturation effects are neglected, the same results are found for the polarisability. However, the damping rate cannot be calculated from Larmor's formula, but it is determined by the dipole matrix element between the ground state  $|g\rangle$  and the excited state  $|e\rangle$

$$\Gamma = \frac{\omega_0^3}{3\pi\epsilon_0\hbar c^3} |\langle e|\mu|g\rangle|^2. \quad (3.12)$$

This corresponds to the spontaneous decay rate of the excited level  $|e\rangle$ . As mentioned before, when saturation effects are neglected, equation 3.6 is a very good approximation for the polarisability. However, at high laser intensities the excited state gets highly populated and equation 3.6 is not valid anymore. Nevertheless, in most experiments, atoms are trapped in far-detuned dipole traps, where the scattering rate is low ( $\Gamma_{Scat} \ll \Gamma$ ) and the classical formulas are valid.

For real atoms the above models are not complete, but they show that an oscillating electromagnetic field can be used to exert a force on any polarisable particle, such as molecules, glass or plastic microspheres and biological specimens, such as cells or the organelles within living cells [47], [49], [50]. In the next section, the dipole potential of multi-level atoms in a far-detuned laser field is described.

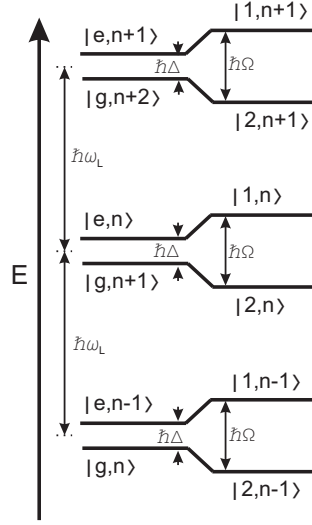


Fig. 3.3: The dressed atom with eigenstates such as  $|e, n\rangle$  and  $|g, n + 1\rangle$ . The eigenstates are degenerate for zero detuning. The shifts shown here are for red detuned light.

### 3.1.3 Dressing Atoms

The dressed atom model describes the atom and light field not independently, but takes the atom and laser mode together and describes it as a whole [51, 52]. The Hamiltonian can be written as

$$H_{DA} = H_{int} + H_{field} + V \quad (3.13)$$

where the kinetic energy term is omitted, so that the Hamiltonian can be diagonalised at a point  $\vec{r}$ . The dressed atom has eigenstates which are linear combinations of photon and atom states such as  $|e, n\rangle$  and  $|g, n + 1\rangle$  where  $n$  is the number of photons in the laser mode (Fig. 3.3). The laser modes  $|e, n\rangle$  and  $|g, n + 1\rangle$  are degenerate for zero detuning. The effect that the (far-detuned) light has on the energy levels, can be treated as a second-order perturbation of the electromagnetic field. The perturbation  $V = \hat{p}\vec{E}$  describes the atomic transitions  $|g\rangle \leftrightarrow |e\rangle$  via the dipole interaction between the laser field and the atom which occur at the Rabi oscillation frequency  $\Omega_R$

$$\langle e, n | V | g, n + 1 \rangle = \frac{\hbar\Omega_R}{2}$$

$$\Omega_R = \sqrt{\frac{12\pi c^2 \Gamma I(\vec{r})}{\hbar \omega_0^3}}. \quad (3.14)$$

Solving the complete Hamiltonian  $H_{DA}\Psi_i = E\Psi_i$  leads to the dressed states  $|1, n\rangle$  and  $|2, n\rangle$  with the eigenenergies

$$\begin{aligned} E_{|1,n\rangle} &= (n+1)\hbar\omega_L - \frac{1}{2}\hbar\Delta + \frac{1}{2}\hbar\Omega \\ E_{|2,n\rangle} &= (n+1)\hbar\omega_L - \frac{1}{2}\hbar\Delta - \frac{1}{2}\hbar\Omega \end{aligned} \quad (3.15)$$

where  $\Omega = \sqrt{\Delta^2 + \Omega_R^2}$  is the energy level splitting. As can be seen from equation 3.14, the energies from equation 3.15 are intensity dependent. The energies are therefore position dependent for inhomogeneous light fields: In a red detuned ( $\Delta < 0$ ) Gaussian laser beam the energy of the ground state  $|g, n+1\rangle$  decreases proportional to the increasing intensity of the laser, as a result, the atom moves to the potential minimum (Fig. 3.1). The optically induced shift of the  $i$ -th state is given by:

$$\Delta E_i = \sum_{j \neq i} \frac{|\langle j | \hat{p} \vec{E} | i \rangle|^2}{E_i - E_j}. \quad (3.16)$$

The shift of the ground state in a two-level atom exactly corresponds to the classical dipole potential (Eq. 3.10). The excited state also shows a shift, but in the opposite direction. The shift of the ground state can be seen as the dipole potential, when the atom resides most of its time in the ground state, this is the case for low saturation.

In reality, an atom is not a pure two-level system, but has many energy levels which interact with the light. To calculate the dipole potential of an alkali atom (e.g. rubidium, see also appendix A), the dipole matrix elements  $p_{ij} = \langle e_i | p | g_i \rangle$  between the ground state  $|g_i\rangle$  and each contributing excited state  $|e_i\rangle$  has to be known, taking into account the relevant Clebsch-Gordon coefficients and detunings. The calculation can be simplified by choosing a laser detuning which is much larger than the hyperfine structure of the excited state. The dipole potential of the ground state with total angular momentum  $F$  and magnetic quantum number  $m_F$  reduces to

$$\begin{aligned} U_{Dip}(\vec{r}) &= -\frac{\pi c^2 (1 - \mathcal{P}g_F m_F)}{2 \omega_{D1}^3} \left[ \frac{\Gamma_{D1}}{\omega_{D1} - \omega} + \frac{\Gamma_{D1}}{\omega_{D1} + \omega} \right] I(\vec{r}) \\ &\quad - \frac{\pi c^2 (2 + \mathcal{P}g_F m_F)}{2 \omega_{D2}^3} \left[ \frac{\Gamma_{D2}}{\omega_{D2} - \omega} + \frac{\Gamma_{D2}}{\omega_{D2} + \omega} \right] I(\vec{r}), \end{aligned} \quad (3.17)$$

$g_F$  is the Landé factor and  $\mathcal{P}$  is the laser polarisation: For linear polarisation  $\mathcal{P} = 0$  and for circular  $\sigma^\pm$  polarisation  $\mathcal{P} = \pm 1$ .  $\omega_{D1}$  and  $\omega_{D2}$  are the transition frequencies of the two  $D$  lines and  $\Gamma_{D1}$  and  $\Gamma_{D2}$  the corresponding natural linewidths.

### 3.2 *Trapping Atoms with Lasers*

There are many ways to trap atoms with lasers, using blue or red detuned lasers or a combination of both. As mentioned before, atoms are repelled from the laser field when the laser frequency is higher than the transition frequency (blue detuning) and attracted to maximum intensity when the laser frequency is lower than the transition frequency (red detuned). Trapping the atoms with a blue detuned laser has the advantage that the trapping light has little or no influence on the atoms, thus unwanted effects such as photon scattering, light shifts of the energy levels, and light-assisted collisions are not there or minimized. A disadvantage is that trapping the atoms in blue detuned lasers is not as straightforward as trapping them in red detuned lasers: Trapping atoms with a red detuned laser can be done by simply focussing the laser beam, whereas at least two blue detuned lasers are needed to form a trap. Therefore, only traps created by red detuned lasers are discussed in this thesis.

#### 3.2.1 *Catching Atoms with a Single Beam*

The simplest way to trap atoms in three dimensions is by focussing a red detuned Gaussian laser beam. This method was used for the first time by Chu and Ashkin [4] and due to its simplicity, it is still being used by many groups all over the world. The intensity distribution of a focussed Gaussian beam is given by [53]

$$\begin{aligned} I(r, z) &= I(z)e^{-\frac{2r^2}{w^2(z)}} \\ &= \frac{2P_0}{\pi w^2(z)}e^{-\frac{2r^2}{w^2(z)}} \end{aligned} \quad (3.18)$$

where  $P_0$  is the total laser power,  $r = \sqrt{x^2 + y^2}$  is the radius of the beam, and  $z$  is the longitudinal axis, or axis of propagation. The waist  $w(z)$  is the radial distance  $r$ , where the intensity  $I(z)$  of the beam has fallen down to

$I(z) \cdot \frac{1}{e^2}$ . The development of the waist along the propagation axis is

$$w(z) = w_0 \sqrt{1 + \left(\frac{z}{z_R}\right)^2}, \quad (3.19)$$

where  $z_R$  is the Rayleigh range, which is the distance where the waist has increased a factor  $\sqrt{2}$  compared with the waist  $w_0$  at the focus:

$$z_R = \frac{w_0^2 \pi}{\lambda}. \quad (3.20)$$

The intensity  $I(z)$  at the rayleigh range is  $I(z_R) = I_0/2$ . When a Gaussian beam is focussed by a lens or a mirror with focal length  $f$ , the waist at the focus is

$$w_0 = \frac{f\lambda}{\pi w(f)}, \quad (3.21)$$

with  $w(f)$  being the waist of the beam at the position of the lens, and  $\lambda$  is the wavelength of the laser. Since the dipole potential is proportional to the intensity distribution, the trap depth  $U_{Dip}$  is given by  $U_{Dip} = |U_{Dip}(r = 0, z = 0)|$ . The steepness of the trap in the radial and the axial direction is not the same, but differs by a factor of  $\pi w_0/\lambda$ . Hence, the potential in the radial direction is steeper.

When the thermal energy  $k_B T$  of atoms trapped in the optical potential is small compared to the trap depth  $U_{Dip}$ , the spread of the atoms in the trap is radially and axially small compared to the waist  $w_0$  and the Rayleigh range  $z_R$ , respectively. In this case, the optical potential can be approximated by a cylindrically symmetric harmonic oscillator. This leads to oscillation frequencies

$$\omega_r = \sqrt{\frac{4U_{Dip}}{mw_0^2}} \quad (3.22)$$

in the radial direction, and

$$\omega_z = \sqrt{\frac{2U_{Dip}}{mz_R^2}} \quad (3.23)$$

in the axial direction, with  $m$  being the atomic mass. Figure 3.4 shows a schematic representation of the single beam optical dipole trap, but also an image of our experimental optical dipole trap taken by absorption detection imaging (section 3.3.6). Also shown in the picture is a crossed dipole trap, where two focussed laser beams are overlapped in their foci.

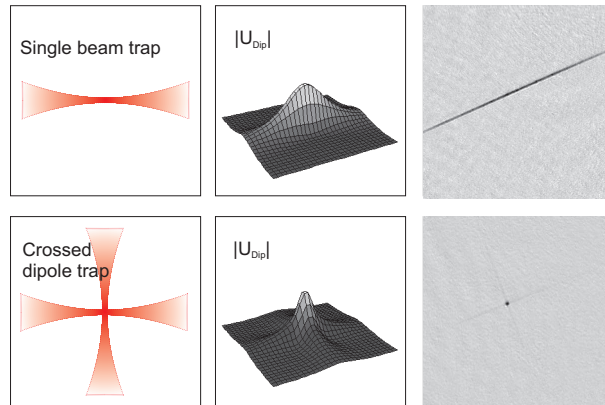


*Fig. 3.4:* In the graph are shown representations of a single beam dipole trap and a crossed beam dipole trap. The corresponding calculated potentials are also shown, as well as pictures of the experimental optical dipole trap taken with absorption imaging techniques (section 3.3.6). The graph clearly shows that a crossed dipole trap has a smaller trapping volume and a tighter confinement.

### 3.2.2 Crossing the Laser Beams

Achieving Bose-Einstein condensation in an optical dipole trap is done by evaporatively cooling the atoms in the trap: High-energetic atoms are removed from the trap and the remaining atoms thermalize through elastic collisions. For this process, high collision rates are necessary, which means that high trapping frequencies are needed. A single beam dipole trap is an anisotropic trap with a relatively weak confinement in the axial direction and a tight confinement in the radial direction and as such is not very suitable for applying evaporative cooling. A crossed dipole trap, however, has a tight confinement in all three dimensions and is thus a good candidate for applying evaporative cooling. Crossing two focussed beams in their foci under a  $90^\circ$  angle creates an almost isotropic trap. Interference effects can be neglected, when the polarisations of the two beams are orthogonal to one another. In this case, the intensity distribution of both beams can be added up:

$$I_{tot} = \frac{2P_x}{\pi w^2(x)} e^{-\frac{2(x^2+y^2)}{w^2(x)}} + \frac{2P_y}{\pi w^2(y)} e^{-\frac{2(x^2+y^2)}{w^2(y)}}, \quad (3.24)$$

with  $x$  and  $y$  being the axes of the laser beams. The trap depth  $U_{Dip}$  is calculated by inserting the total intensity  $I_{tot}$  in equation 3.17, but keep in mind that the effective dipole potential is only  $U_{Dip}/2$  for two beams with identical laser powers, since atoms with a larger energy leave the trap along one of the arms. The potential can also be described by a harmonic oscillator to derive the oscillation frequencies of the trap, given by

$$\begin{aligned}\omega_x &= \sqrt{-\frac{8U_\omega}{\pi m} \left( \frac{P_x}{2w_{0,x}^2 x_R^2} + \frac{P_y}{w_{0,y}^4} \right)} \\ \omega_y &= \sqrt{-\frac{8U_\omega}{\pi m} \left( \frac{P_x}{w_{0,x}^4} + \frac{P_y}{2w_{0,y}^2 y_R^2} \right)} \\ \omega_z &= \sqrt{-\frac{8U_\omega}{\pi m} \left( \frac{P_x}{w_{0,x}^4} + \frac{P_y}{w_{0,y}^4} \right)},\end{aligned}\tag{3.25}$$

where  $U_\omega$  is the optical dipole potential without the intensity distribution ( $U_{Dip} = U_\omega \cdot I_{tot}$ ):

$$\begin{aligned}U_\omega &= -\frac{\pi c^2}{2} \frac{1}{\omega_{D1}^3} \left[ \frac{\Gamma_{D1}}{\omega_{D1} - \omega} + \frac{\Gamma_{D1}}{\omega_{D1} + \omega} \right] \\ &\quad - \frac{\pi c^2}{2} \frac{2}{\omega_{D2}^3} \left[ \frac{\Gamma_{D2}}{\omega_{D2} - \omega} + \frac{\Gamma_{D2}}{\omega_{D2} + \omega} \right].\end{aligned}\tag{3.26}$$

The oscillation frequencies are now in the three dimensions  $x$ ,  $y$  and  $z$ , where  $x$  and  $y$  are the axes of the laser beams, note that  $\omega_z$  is not the axial oscillation frequency of section 3.2.1! From equations 3.26 it is clear that the atoms have the tightest confinement in the  $z$ -direction. The laser beams are therefore usually set up in the horizontal plane, so that the strongest dipole force works in the direction of gravity. The gravity does not play a big role when deep dipole traps are used, but when the atoms are evaporatively cooled, the trap depth becomes very small and gravity starts to play a significant role (see also section 4.5).

### 3.3 Putting Theory into Practice

Several demands have to be met, before a Bose-Einstein condensate can be made in an "all optical way". First of all, the atoms have to be transferred

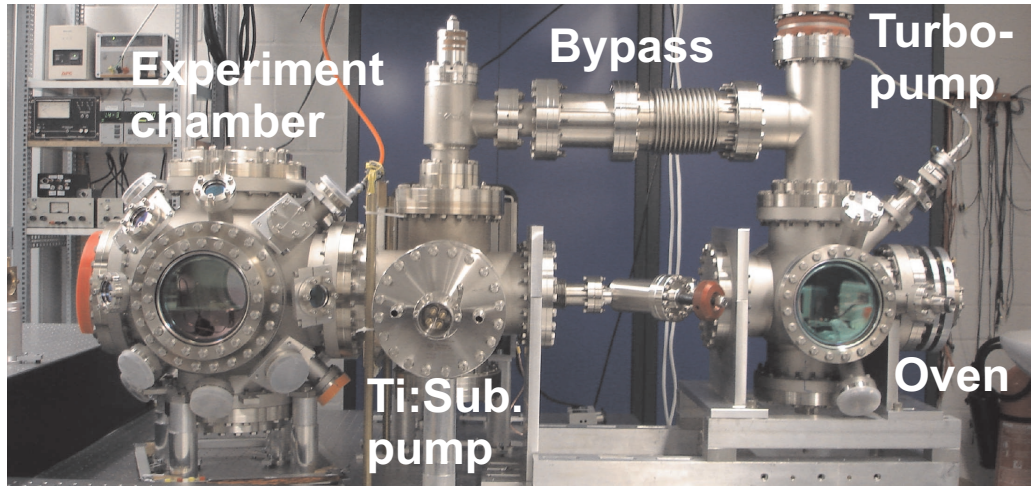


*Fig. 3.5:* The vacuum chamber.

into the dipole trap as efficiently as possible. This means that the trap should be as large as possible, having a large trap depth and a large trapping volume to trap as many atoms as possible. But at the same time, large densities and high oscillation frequencies are needed for the high collision rate necessary for the evaporative cooling. Another requirement is that losses from the trap and heating effects should be as small as possible. The way to fulfill all these demands is explained in this section, starting with the experimental set up necessary to cool rubidium atoms (see appendix A for a short introduction to the rubidium 87 atom).

### 3.3.1 *The Vacuum Chamber*

First of all, we need an environment for the rubidium atoms, where they are completely isolated from the surroundings: This is done by placing them in a vacuum. The vacuum chamber is shown in figure 3.5. The oven with rubidium atoms is separated from the main experiment chamber by a differential pumping stage (a tube of 15 cm length and 3 mm inner diameter) so that the pressure in the experiment chamber can be kept very small. The oven chamber is being pumped by a turbopump (Turbovac TW300, Leybold Vacuum), which is connected to a backing pump (rotary vane pump DUO 035D, Pfeiffer Vacuum). The experiment chamber is pumped by an ion getter pump (Noble Diode, Varian) and the Ti:Sublimation pump (SS-400/275,

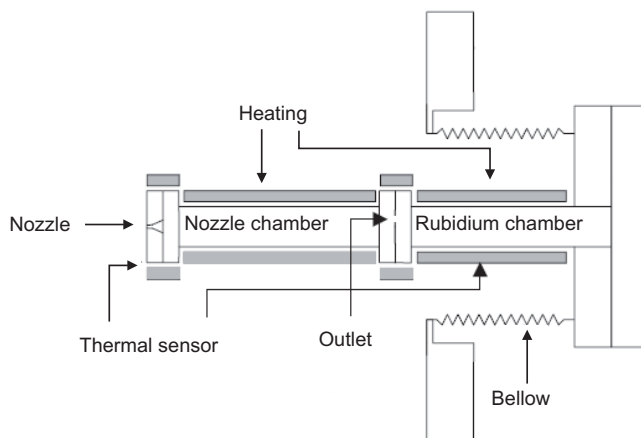


Fig. 3.6: The oven.

Thermionics Laboratory, Inc.) can also be used when needed. The pressure reached in the experiment chamber is  $\sim 6 \cdot 10^{-11}$  mbar and the pressure in the oven chamber is  $\sim 5 \cdot 10^{-7}$  mbar in normal operation mode. The bypass valve is only opened, when the vacuum has been breached (e.g. when the rubidium in the oven is refreshed) and we need a high pumping speed to pump the experiment chamber from atmospheric pressure down to lower pressures, after which we can start the ion getter pump. In normal operation, the bypass valve is always closed.

Before the atoms can be cooled down to nanoKelvin temperatures, they have to be first heated up to  $100^\circ - 150^\circ$  so that they can leave the oven. A picture of the oven is shown in figure 3.6. Rubidium metal (10 gram, 99.5%, ChemPur Feinchemikalien und Forschungsbedarf GmbH) is placed in the rubidium chamber every 1 – 2 years. The rubidium chamber is heated (heating element SEA 20/500, Thermocoax) to free atoms from the metal, upon which they enter the nozzle chamber. The nozzle chamber prevents the metal from blocking the nozzle and from entering the oven chamber. It is also heated, but made ten degrees hotter so that the atoms do not condense in the chamber and block the nozzle. The flange closing the rubidium chamber is heated from the outside for the same reason. The bellow allows us to align the nozzle of the oven with the axis of the differential pumping stage tube. Atoms leaving the oven have a velocity of about  $300 - 400$  m/s and thus have to be cooled with standard laser cooling techniques before they can

be trapped in a magneto-optical trap (MOT), which has a typical velocity capture range of  $\sim 50$  m/s.

### 3.3.2 Cooling the Atoms

A complete description of laser cooling can be found in [54] and [55]. The first person to show that light exerts a force on atoms was Otto Frisch in 1933 [56], who used a low intensity sodium lamp to deflect atoms. The observed deflection was very small: For this reason controlling the motion of atoms with light forces wasn't feasible until the discovery of tunable lasers. Laser cooling is based on the absorption and emission of photons with an energy  $E = \hbar\omega$  and an impulse  $p = \hbar k$ . An atom absorbing a photon is excited and its momentum changes from  $\vec{p}_i$  to  $\vec{p}_k = \vec{p}_i + \hbar\vec{k}$ . At a later time, the atom de-excites by emitting a photon in a random direction. If the atom is placed in a laser field, which is in resonance with the transition, the atom can absorb and emit many photons. Although the recoil is very small (for the  $D2$  transition of  $^{87}\text{Rb}$  at 780 nm is the recoil velocity  $\hbar k/m = 5.9$  mm/s), the cumulative effect of absorbing and emitting many photons can result in a big velocity change. The averaged force working on the atom is given by the scattering force:

$$\vec{F}_{scat} = \hbar\vec{k}\Gamma_s, \quad (3.27)$$

with the total scattering rate  $\Gamma_s$  given by:

$$\Gamma_s = \frac{s_0\Gamma/2}{1 + s_0 + [2(\Delta + \Delta\omega_{Doppler})/\Gamma]^2}, \quad (3.28)$$

where  $\Delta = \omega_0 - \omega$  is the detuning from resonance,  $\Delta\omega_{Doppler}$  is the Doppler shift, and the saturation parameter  $s_0 = \frac{I}{I_s}$ , where  $I_s$  is the saturation intensity. The direction of the force is given by the wave vector  $\vec{k}$ .

Atoms coming from the oven are decelerated by a laser beam coming from the opposite direction. To maximize the light absorption and the scattering rate, the Doppler shifted laser frequency in the moving atoms reference frame should match the atomic transition frequency. This can be done by using the Zeeman effect, where a spatially varying magnetic field shifts the energy levels of the atoms such that the changing Doppler shift is compensated, or by changing the laser frequency during the deceleration (chirp cooling). We use the latter method: The disadvantage of this method is that the magneto-optical trap is not loaded continuously, but the atoms arrive in packages. The

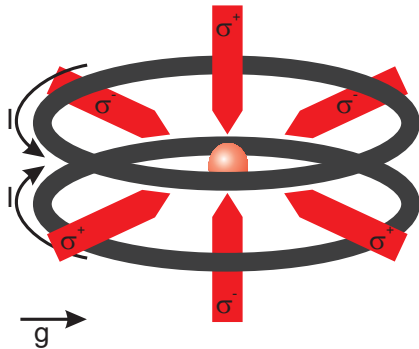


Fig. 3.7: Schematic representation of the magneto-optical trap. Gravity points to the left

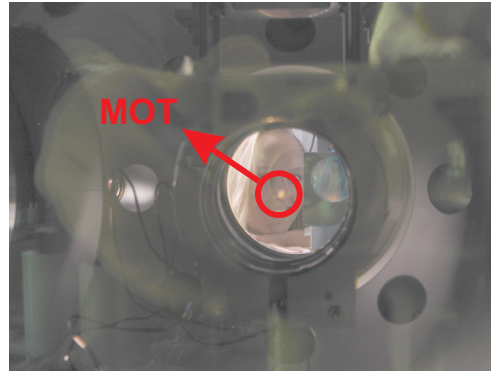


Fig. 3.8: The MOT. Shown are the anti-Helmholtz coils with in its center the trapped atoms.

advantage is that disturbing residual magnetic fields from a Zeeman slower are avoided.

It should be noted that deceleration is not the same as cooling, but as the atoms are slowed down, the originally wide thermal velocity distribution is not only shifted to lower velocities but also compressed, leading to an increase in phase space density, and thus atoms are cooled.

### 3.3.3 The Magneto-Optical Trap (MOT)

The most widely used trap for neutral atoms is the magneto-optical trap, which was first realised in 1987 [57]. A MOT is a combination of a quadrupole field created by two coils in anti-Helmholtz configuration and six red detuned laser beams with circular polarisations ( $\sigma^+$  and  $\sigma^-$ ), as shown in figure 3.7. The force working on the atoms is now not only velocity dependent, but also position dependent: Due to the circular polarisation of the laser beams, the transitions only take place in the magnetic substates  $m_F$  of the atom, which depend on the inhomogeneous magnetic field. Therefore, the atoms in a MOT are not only trapped, but are also compressed and cooled.

High densities are necessary to achieve Bose-Einstein condensation, but in a MOT there are a few effects which limit the density: First of all, the density of the MOT is limited by collision processes, but another density limiting effect is the fluorescence radiated by deexciting atoms in the MOT. The fluorescence can be absorbed by other atoms in the MOT, leading to

a repulsion between the atoms. Additionally, the trapped cloud becomes opaque for high densities. The density limit can be overcome by reducing the intensity of the repumping light so that only a fraction of the atoms reside in the transition used for cooling. This reduces the effective force on the atoms, but the density can be increased by a factor of 100 [58]. The phase space density in a MOT is typically  $10^{-7} - 10^{-6}$ , with an atomic density of  $\sim 10^{11}$  atoms/cm<sup>3</sup>.

The quadrupole field in the experiment is made by two coils in anti-Helmholtz configuration, spaced 2.5 cm apart, and a coil radius of 4 cm. Each coil has 37 windings through which 7 A current is flowing, corresponding to a 12 G/cm magnetic field. The MOT is placed precisely in the center of the chamber so that the chirp laser beams and the atom beam, which are placed 6 mm above the center of the chamber, do not influence the trapped atom cloud. The MOT can trap  $5 \cdot 10^9$  atoms.

### 3.3.4 *The Lasers*

Grating stabilized laser systems in Littrow configuration are used for the chirp cooling process. The  $5^2S_{1/2}, F = 2 \rightarrow 5^2P_{3/2}, F' = 3$  transition of  $^{87}\text{Rb}$  is used for cooling (appendix A). Because of the small but finite probability for atoms to excite to the  $5^2P_{3/2}, F' = 2$  level, a repumping laser is needed to pump them back into the cooling cycle. The repumping laser is resonant with the  $5^2S_{1/2}, F = 1 \rightarrow 5^2P_{3/2}, F' = 2$  transition. The lasers are frequency stabilized by rubidium saturation spectroscopy. The gratings of both chirp lasers are directly attached to a piezo, and are continuously moved over a small range, so that the frequency of the lasers varies over 440 MHz to counteract the changing Doppler shift of the slowing atoms. As a result, the position of the laser beam moves slightly. For this reason, the cooling laser beam is coupled into the laser diode of a slave laser. About 21 mW is used to cool the atoms in the chirp beam, and 1.2 mW to pump them back in the cooling transition.

Just with the chirp laser system, we need two laser systems to cool rubidium atoms in the MOT. The MOT cooling laser consists of a master laser, which is then amplified by a tapered amplifier (Eagleyard) to a maximum output power of 1 W. The master laser and the repumping laser are also grating stabilized systems in Littrow configuration, but now following the design presented in [59]. The main differences are that in this design both the laser diode and the grating are temperature stabilized, and the grating

is not directly attached to the piezo, but to a cantilever, which is moved by the piezo. The changes in laser design lead to a higher stability of the laser, since the laser is less sensitive to mechanical vibrations and thermal drifts.

The MOT repumping laser and the MOT cooling master laser are stabilized by generating a beat note, whereby a part of the light is superimposed with a reference laser on a photodiode. The servo system ensures a fixed frequency offset to the MOT laser by locking the frequency of the beat note to a constant value. The so-called offset locking technique allows for a large tuning range of the laser frequency. The error signal for locking the MOT repumping laser is made by an electronic delay line, which produces a frequency dependent phase shift. This phase shift is then converted into an amplitude signal by an electronic phase detector [60]. For the MOT cooling laser a frequency-to-voltage convertor is used [61]. Both lasers are 15 MHz red detuned from resonance.

The reference laser is an interference-filter-stabilized diode laser [62], which is stabilized with a rubidium saturation spectroscopy. The laser is simultaneously used as the detection laser for absorption imaging. The intensity (and the frequency) of each laser, except the chirp lasers, can be varied with acousto-optical modulators (AOM). Mechanical shutters (LS2T2, Uni-blitz) with a shutter time of 1 – 2 ms are placed in the laser beams to prevent resonant laser light from entering the experimental chamber when the atoms are loaded in the optical dipole trap.

The laser systems and the vacuum chamber are placed on two separate optical tables. The cooling laser beam and the repumping laser beam used for the separate cooling processes are overlapped on the laser table before they are coupled into polarisation maintaining fibers, which bring the light to the experiment. The six laser beams necessary for the MOT are made by retro-reflecting three laser beams. The overlapped cooling and repumping beam is divided in three beams on the laser table, before each beam is coupled into a fiber.

### 3.3.5 The Optical Dipole Trap in Practice

The optical dipole trap is created by a diode pumped Yb:YAG thin disk laser (VersaDisk) from ELS Elektronik Laser System GmbH, now Sahajanand Laser Technologies. The VersaDisk produces a maximum output power of 25 W at 1030 nm in single frequency operation. The emitted beam has a Gaussian beam profile with a  $M^2$  value better than 1.1.

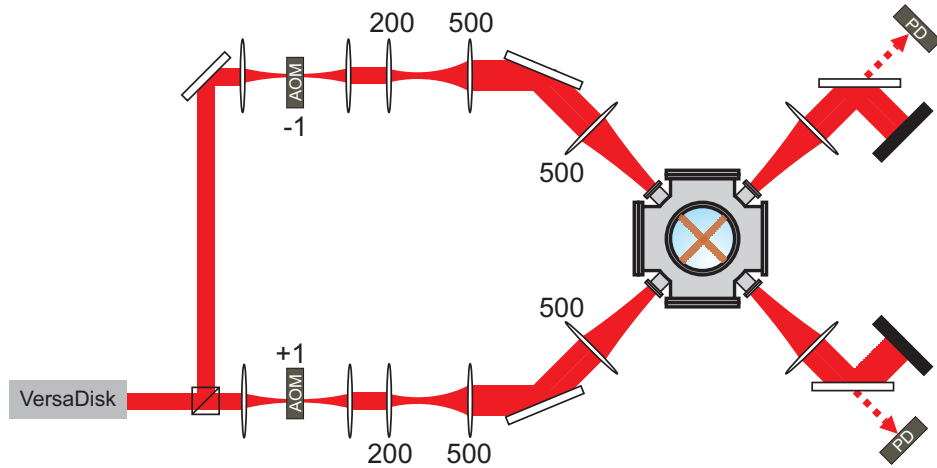
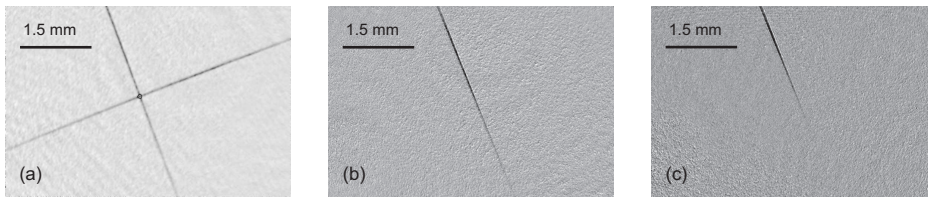


Fig. 3.9: The crossed optical dipole trap. The beam coming from the laser is split in two, after which each laser beam is sent through an AOM. The frequency of the horizontally polarized laser beam is shifted +120 MHz and the vertically polarized beam is shifted  $-120$  MHz. The beams are collimated and then focussed by a 200 mm focal length lens. The foci are imaged into the vacuum chamber by two 500 mm focal length lenses. The intensity of each laser beam is stabilized by detecting the transmission of the beam through a mirror with a photodiode. The corresponding signal is sent to a PI-control box.

The laser beam is split in two parts with equal intensities, but with perpendicular linear polarisations to avoid interference effects. Both beams are focussed down into an AOM (3110-125 (Horizontal polarisation) and 3110-197 (vertical polarisation), Crystal Technologies), and the first order diffracted beam is used to create the crossed dipole trap. Both AOMs shift the frequency of the laser beams 120 MHz, but the horizontally polarized beam is shifted to higher frequencies, whereas the vertically polarized beam is shifted to lower frequencies (Fig. 3.9). Then, the laser beams are collimated. The  $1/e^2$  waist of the laser beam is 1.4 mm, so that by careful choice of the focussing lens, a focus with a waist between 5 and 100  $\mu\text{m}$  can be selected. This focus is then imaged 1 : 1 into the experiment chamber. We used a 200 mm focussing lens, creating a (theoretical) waist of 47  $\mu\text{m}$  in the focal plane.

The diffracted beam intensity of the AOM is a function of the acoustic



*Fig. 3.10:* The focus of the dipole trap beam is moved due to the thermal lens effect. The beam traversing the AOM is collimated. (a) The foci of both beams are exactly in the crossing point. (b) Only one beam is shown for clarity. The laser power is ramped down from 6 W to 600 mW in 1 s. (c) The laser power is ramped down in 15 s. The focus moves at least 1 mm.

power, therefore, the AOM is used to turn off the dipole trap beam (response time  $\sim 100$  ns), or to perform evaporative cooling by ramping down the RF power and hence, the intensity. The AOM is also used for an active intensity stabilisation of the laser: The VersaDisk has a 10% power fluctuation, which has a negative effect on the number of atoms loaded in the dipole trap. For these purposes, a small part of the light that is transmitted through a normal mirror (transmission is  $\sim 0.1\%$ , which corresponds to a power of 5 – 10 mW in our case for a single beam) is used and sent onto a photodiode (Fig. 3.9). The photodiode signal is sent to a PI-control box, and from there back to the AOM. The only downfall of this system is the dependence of the mirror transmission on the polarisation of the beam, since acousto-optic devices can rotate the polarisation of an optical beam [63]. In fact, in our stabilisation setup, only the intensity of the beam falling onto the photodiode is kept constant, but that does not mean that the intensity of the first order beam is kept constant. By creating a little (more) anisotropy in the crystal, the incident beam and the diffracted beam will see different refractive indices and the polarisation is changed. This is only a problem during the evaporation cycle, where we lower the intensity of the laser beam by decreasing the RF power of the AOM. We have solved the problem by placing a polarisation beamsplitter cube right behind the AOMs.

Another problem concerning the AOM is the thermal lensing effect. We have seen in our experiments, that when the RF power is ramped down, the focus of the dipole trap moves at least 1 mm along the beam propagation axis (Fig. 3.10). The thermal lensing effect can be reduced by optimizing

the shape of the beam. We have reduced the effect, by focussing the beam through the AOM. The width of the focus in the AOM is  $\sim 150 \mu\text{m}$ , corresponding to an optical power density of  $\sim 35 \text{ kW}/\text{cm}^2$ , which is well below the  $10 \text{ MW}/\text{cm}^2$  optical power density specified for our AOMs.

### 3.3.6 *Detecting the Atoms*

There are three processes connected with the interaction of atoms with light, which can be exploited for the detection of atoms. The re-emission of photons is used in the fluorescence imaging method, and the phase shift of a beam transmitted through a cloud is used in dispersive imaging methods. The atoms in our experiment are detected with absorption imaging. In essence, absorption imaging relies on the resonant scattering of photons out of a probe beam, and the decrease of the probe beam intensity is measured. The setup is shown in figure 3.11. The atom cloud is imaged 1 : 1.3 onto a CCD camera (SenSys KAF-0401E, with a pixel area of  $9 \times 9 \mu\text{m}^2$ , Photometrics) by a single lens with  $f = 150 \text{ mm}$  focal length. The atoms absorb photons from the probe beam, which is resonant with the  $F = 2 \rightarrow F' = 3$  transition. The resulting shadow casted on the camera is used to determine the number of atoms. For each measurement, three pictures are taken: The first picture is the actual absorption image. After readout, which takes 2 s for our camera, a second picture is taken (reference picture), where the probe beam is turned on again with the same intensity and the same period of time. The atoms have fallen out of the detection region, thus the full intensity of the laser is measured. The third picture (dark picture) taken is without the probe laser, but under the same conditions as before. The dark picture is subtracted from the first two pictures, to eliminate dark counts of the camera and background light.

The decrease in intensity of the probe beam in an atom cloud is exponential, and is described by the Lambert-Beer law:

$$\begin{aligned} I &= I_{probe} e^{-OD} = I_{probe} e^{-\tilde{n}\sigma_0}, \\ \ln I - \ln I_{probe} &= -OD, \end{aligned} \tag{3.29}$$

$I_{probe}$  is the intensity of the probe beam. The optical density  $OD$  is the column density  $\tilde{n} = \int n\sigma_0 dz$  of atoms along the direction of the beam for the scattering cross section  $\sigma_0 = \frac{3\lambda^2}{2\pi}$ . Equation 3.29 is only valid for probe beams which are on resonance. When the probe beam is detuned from resonance,

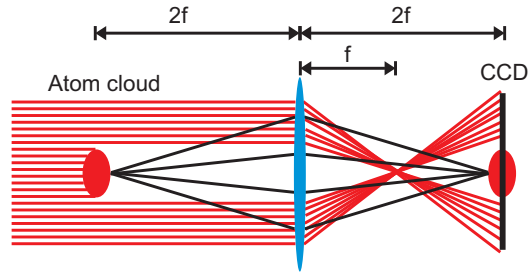


Fig. 3.11: The detection setup for absorption imaging. The atom cloud is imaged 1 : 1 onto the CCD camera.

we can include this detuning by multiplying the scattering cross section in equation 3.29 with the scattering rate  $\Gamma_s$  (Eq. 3.28). The number of atoms per pixel can be attained by multiplying the area  $A$  of the atom cloud imaged on camera pixel with the column density  $\tilde{n}$ . For a 1 : 1 imaging, the area is just the area of one pixel ( $81 \mu\text{m}^2$ ). However, we have a small magnification  $M$  in our setup ( $M = 1.3$ ), so we have to multiply the pixel area with the magnification factor squared:  $A = (bM)^2$ ,  $b$  is the size of the pixel. From equation 3.29, we get for the atom number  $N$ :

$$N = \sum_{\text{pixel}} \frac{2AI_s}{\hbar\omega\Gamma\alpha} \left( 1 + \left( \frac{2\Delta}{\Gamma} \right)^2 \right) \ln \left( \frac{c_{\text{Absorption}} - c_{\text{Dark}}}{c_{\text{Reference}} - c_{\text{Dark}}} \right). \quad (3.30)$$

This equation is valid for small intensities  $I_{\text{probe}} \ll I_s$ , the saturation parameter is for rubidium 87 atoms  $I_s = 1.669 \text{ mW/cm}^2$ . The photon counts for each pixel are denoted by  $c_{\text{Absorption}}$ ,  $c_{\text{Reference}}$  and  $c_{\text{Dark}}$  for the absorption picture, reference picture and dark picture, respectively. An important parameter is the absorption coefficient  $\alpha$ , which depends on the polarisation of the probe beam and the  $m_F$ -states of the transition,  $\alpha = 1$  for circular polarisation, and  $\alpha = 0.5$  for linear polarisation.

Equation 3.30 does not depend on the intensity of the probe beam, which is very advantageous, because detecting with coherent light almost always occurs with interference. The interference pattern only has a small influence on the total number of atoms, since the data is analyzed per pixel. However, the interference patterns of the absorption and reference picture have to be identical, which is not always the case due to beam pointing instability of the detection beam.



## 4. A FAST ROUTE TO BOSE-EINSTEIN CONDENSATION

### *Overview of this chapter*

In this chapter, a simple and fast route to Bose-Einstein condensation is described. Our experiment starts with loading the MOT with rubidium atoms, during this time the dipole trap is already turned on and running with full laser power. This has no visible effect on the atom number loaded in the MOT ( $\sim 5 \cdot 10^9$  atoms), or on the number of atoms loaded in the dipole trap ( $\sim 3.5 \cdot 10^5$  atoms). After the MOT is loaded, the atoms are transferred to the dipole trap. In the loading phase, or the molasses phase, the detuning of the MOT cooling laser is increased, and the intensity of the repumping and cooling laser is decreased to maximize the number of atoms loaded, as is described in the following (section 4.2). Then, we can start the evaporation cycle, where the laser power is ramped down with three linear ramps (section 4.3), and a BEC is made (section 4.5).

### *4.1 Characterizing the Dipole Trap*

The trapped atoms in the dipole trap are imaged with the absorption imaging technique explained in section 3.3.6. The probe laser is resonant with the  $5^2S_{1/2}, F = 2 \rightarrow 5^2P_{3/2}, F' = 3$  transition and illuminates the atoms for  $20 \mu\text{s}$ . We have to take care that we do not heat the cloud during the illumination. Therefore, the duration of the light pulse is kept short, and the intensity is low ( $I_{abs} \leq 130 \mu\text{Wcm}^{-2} \ll I_s$ ). The trap is switched off during the illumination to avoid the complexity arising from the AC Stark shift. In a normal experiment, about  $3 \cdot 10^5 - 4 \cdot 10^5$  atoms are captured in the crossed dipole potential out of  $\sim 5 \cdot 10^9$  atoms loaded in the MOT. This is much less than the number of atoms that can be trapped in a single beam trap ( $\sim 5 \cdot 10^7$  atoms), because the trapping volume is much smaller (Fig. 4.3).

### 4.1.1 The Lifetime

The lifetime of atoms in the dipole trap is determined by three processes: One-body losses, two-body losses, and three-body recombination. Two-body losses and three-body recombination are collisional losses, and therefore depend on the density of the atom cloud: The higher the density, the higher the losses. Two-body losses include photoassociation (which can be induced by the trapping laser light), ground state hyperfine changing collision, and radiative escape. In three-body collisions, three atoms collide and are lost, because two of the colliding atoms form a molecule, and the third carries away the excess energy. However, as will be shown later in this section, the lifetime of the dipole trap is mainly limited by one-body losses caused by background collisions and heating mechanisms, such as laser induced heating, heating due to photon scattering and heating due to background collisions. The first process arises from laser intensity fluctuations and pointing instability. It causes parametric heating, by which the atoms can be driven out of the trap (section 4.1.2). The dipole trap laser is intensity stabilized as explained in section 3.3.5, thus reducing heating due to intensity fluctuations. We have not observed beam pointing instability in our experiment.

The heating due to photon scattering can be determined by calculating the photon scattering rate given by equation 3.9. In a crossed dipole trap, where the waists of the laser beams are 40  $\mu\text{m}$  and the laser power is 14 W, the scattering rate is 4 photons/s. The energy gained by an atom due to the absorption of one photon is

$$E_{recoil} = \frac{\hbar^2 k^2}{2m}. \quad (4.1)$$

The heating induced by the scattering is given by

$$\dot{E} = \Gamma_s \times 2E_{recoil}, \quad (4.2)$$

which gives a heating rate of  $\sim 800$  nK/s for a dipole trap with a  $k_B \cdot 900$   $\mu\text{K}$  trap depth. This means that  $\sim 1125$  scattering processes are needed to heat one atom out of the trap, leading to a (theoretical) lifetime of  $\sim 280$  s. The heating rate decreases when the laser power decreases, e.g. during the evaporative cooling. For typical end values of 200 mW, the scattering rate is 0.05 photons/s, and the heating rate is 10 nK/s.

Heating also arises from collisions with background atoms, where the colliding atom does not leave the trap. This happens for small scattering

angles  $\theta$ , which is the angle between the final and initial relative velocity  $\vec{v}_r = \vec{v}_a - \vec{v}_b$ , with the velocity of the trapped atom  $\vec{v}_a$ , and the velocity of the background atom  $\vec{v}_b$ . For an atom to leave the trap, the scattering angle should be larger than the threshold angle  $\theta_0$ . The threshold angle is determined by  $\Delta E(\theta_0) = U_{Dip}$ , where  $\Delta E$  is the average energy that a trapped atom gains after colliding with a background atom. The change in average energy of a trapped atom when it collides with a background gas atom is [64]

$$\Delta E = \frac{4\pi\hbar^2}{m\sigma}, \quad (4.3)$$

where  $\sigma$  is the total scattering cross section. In the case of rubidium atoms, the energy due to the collision between a trapped and an untrapped atom is  $k_B \cdot 2.8$  mK [64], which is much larger than our trap depth. The heating rate is given by [64]:

$$\dot{Q} = 0.37\alpha \frac{U_{Dip}^2}{\Delta E}, \quad (4.4)$$

where  $\alpha$  is the one-body loss rate. As is shown later in this section, the  $1/e$  lifetime  $\tau = 12$  s of our dipole trap with a  $k_B \cdot 400$   $\mu$ K trap depth is limited by one-body losses (Fig. 4.1). The heating rate due to background collisions in the trap is then  $\dot{Q} = 1.7$   $\mu$ K/s.

The lifetime of the dipole trap can be increased, by decreasing the pressure in the vacuum chamber. In this case, the possibility of trapped atoms colliding with background atoms is lowered, resulting in a lower heating rate. Bose-Einstein condensation was reached with a typical vacuum chamber pressure of  $\sim 5 \cdot 10^{-11}$  mbar.

The lifetime of the dipole trap is measured by observing the number of atoms in the trap for different holding times. All the other light sources are blocked, so that resonant light cannot influence the lifetime of the atoms in the trap. Figure 4.1 shows the decay of rubidium atoms in the  $F = 1$  state and in the  $F = 2$  state of the  $5^2S_{1/2}$  ground state for a background pressure of  $6 \cdot 10^{-10}$  mbar. The loss of the atoms is well described by

$$\frac{dN}{dt} = -\alpha N - \beta N^2 - \gamma N^3, \quad (4.5)$$

where  $\alpha$  is an exponential loss rate caused by heating mechanisms and background collisions,  $\beta$  a collisional loss coefficient and  $\gamma$  is a three-body loss coefficient. The three-body rate constant for rubidium atoms in the

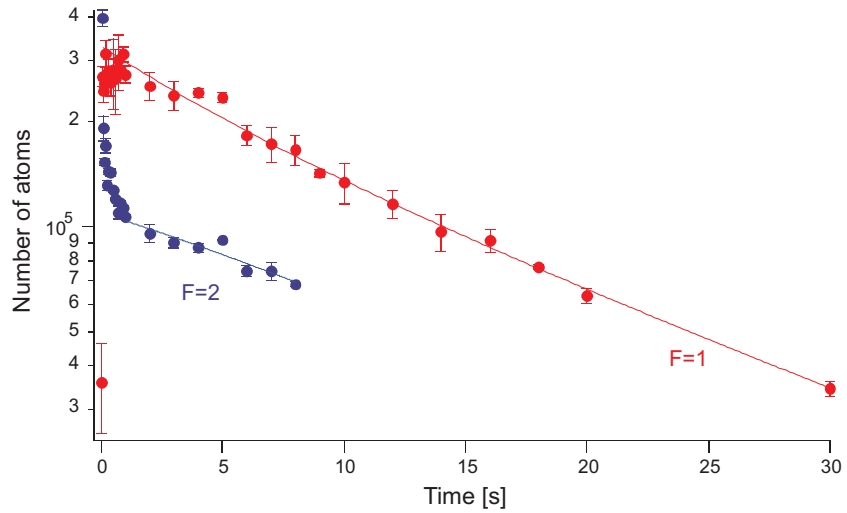


Fig. 4.1: Lifetime measurements of the  $5^2S_{1/2}, F = 1$  and the  $5^2S_{1/2}, F = 2$  ground state. Three measurements were taken for each data point and the error bar is the standard deviation. The data was fitted to equation 4.6. Atoms in the  $F = 1$  ground state show an exponential decay, whereas atoms in the  $F = 2$  ground state cannot be described by equation 4.6. The loss rate for atoms in the  $F = 2$  ground state is much larger than the atoms in the  $F = 1$  ground state. This can be contributed to three-body losses and hyperfine changing collisions. The measurement was made with a background pressure of  $6 \cdot 10^{-10}$  mbar.

$F = 1, m_F = -1$  state is  $4.3 \cdot 10^{-29} \text{ cm}^6\text{s}^{-1}$  [65]. For a dipole trap with  $k_B \cdot 400 \text{ } \mu\text{K}$  trap depth, and an initial density  $n = 3.4 \cdot 10^{13} \text{ atoms/cm}^3$  and atom number  $N = 350,000$ , this leads to an atom loss of  $3300 \text{ atoms/s}$ .<sup>1</sup> The three-body  $1/e$  lifetime of the trap is then  $66 \text{ s}$ , much larger than the actual lifetime of  $12 \text{ s}$ . Therefore, the three-body loss term is neglected. The solution of the loss rate becomes

$$N(t) = \frac{N_0\alpha}{(\alpha + N_0\beta)e^{\alpha t} - N_0\beta}. \quad (4.6)$$

The one-body loss coefficient  $\alpha$  is only dominant for long holding times and for low densities, but the collisional loss coefficient  $\beta$  depends on the density of the atom cloud and becomes increasingly important for higher densities. During the evaporative cooling, the density of our atom cloud is increased. Therefore, the collisional loss parameter  $\beta$  becomes the main loss parameter for our experiment during evaporation.

Figure 4.1 shows an exponential loss rate for the atoms in the  $F = 1$  ground state. This means that the lifetime of the atoms is only limited by collisions with background atoms and heating, which is an exponential decay with a lifetime  $\tau = \alpha^{-1}$ . Equation 4.6 is used as a fit function to the data to obtain the loss coefficients  $\alpha$  and  $\beta$  for the two ground states. The loss coefficients for the  $F = 1$  ground state are

$$\begin{aligned} \alpha_{F=1} &= 0.058 \pm 0.004 \text{ s}^{-1} \\ \beta_{F=1} &= 1.4 \cdot 10^{-7} \pm 2.5 \cdot 10^{-8} \text{ s}^{-1}. \end{aligned} \quad (4.7)$$

The errors of the loss coefficients were determined by the fit. The value of the one-body loss coefficient  $\alpha$  is much larger than the collisional loss coefficient  $\beta$ . This, and the 7% uncertainty in the one-body loss rate shows us that the contribution of the collisional loss parameter  $\beta$  to the decay cannot be determined accurately. Therefore, the 20% error determined by the fit for  $\beta$  is much too small. The effective dipole trap volume  $V_{eff}$  given by

$$V_{eff} = \left( \frac{2\pi k_B T}{m} \right)^{3/2} \frac{1}{\bar{\omega}^3}, \quad (4.8)$$

<sup>1</sup> The loss due to three-body recombination is given by the loss rate equation  $\frac{dN}{dt} = -K_3 \int_V n^3(\vec{r}, t) d\vec{r}$ . In a harmonic potential, the density distribution can be approximated by a Gaussian function, and the equation becomes  $\frac{dN}{dt} = -K_3 \frac{N^3}{\pi^{3/2} \sqrt{27} \sigma_x^2 \sigma_y^2 \sigma_z^2}$  with  $\sigma_i = \sqrt{\frac{k_B T}{m \omega_i^2}}$  for  $i = x, y, z$ .

was in the lifetime measurement  $1.03 \cdot 10^{-8} \text{ cm}^3$ , giving a volume independent collisional loss rate  $\beta'$

$$\beta'_{F=1} = 1.4 \cdot 10^{-15} \text{ cm}^3 \text{ s}^{-1} \quad (4.9)$$

This is one order of magnitude larger, than the value given in reference [65]:  $\beta \leq 1.6 \cdot 10^{-16} \text{ cm}^3 \text{ s}^{-1}$ . This value was determined in a magnetic trap, and thus does not include light assisted collisions. In our dipole trap with a  $k_B \cdot 400 \text{ } \mu\text{K}$  trap depth, the scattering rate is only 2 photons/s. Therefore, the contribution of the light assisted collisions to the two-body loss rate is negligible, and does not explain the one order of magnitude difference. One of the differences between magnetic traps and optical dipole traps is that optical dipole traps have a finite trap depth, whereas the trap depth of magnetic traps is only limited by the geometry of the quadrupole coils creating the magnetic field. For this reason, atoms trapped in an optical dipole trap require a smaller energy to escape the trap. Even though we cannot accurately determine the two-body loss rate, this might explain the larger two-body loss rate of the optical dipole trap.

The  $F = 1$  ground state shows a small incline in atom number in the first second of the lifetime measurement. This is because the dipole trap beams are not completely horizontal, so that atoms from the arms of the dipole trap can slide into the crossing point (Fig. 4.3). This might lead to a smaller value for  $\alpha$ , since the dipole trap loses atoms due to collisions and heating, but at the same time gains atoms from the arms.

Equation 4.6 cannot be fitted to the lifetime measurement of the  $F = 2$  ground state and thus does not describe the loss processes of the atoms in this state. The graph shows two decay processes: In the first decay process, the number of atoms in the dipole trap has dropped down to  $N/e$  in only 300 ms. This can partly be contributed to ground state hyperfine changing collision, which only occurs for atoms in the  $F = 2$  ground state. However, this is not the only loss process contributing to the fast decay. The other loss rate influencing the lifetime of the atoms can only be contributed to three-body losses, since we have neglected this term in the loss rate fitted to our data (Eq. 4.6). After about 1 s, the second decay process becomes prominent, and resembles the loss rate of atoms loaded in the  $F = 1$  state. This part has been fitted with equation 4.6, and shows an exponential decay with an one-body loss coefficient  $\alpha_{F=2} = 0.08 \text{ s}^{-1}$ . The second decay process is thus only limited by background collisions.

The loss rate of the atoms in the  $F = 2$  ground state is much larger, than

the loss rate of the atoms in the  $F = 1$  ground state. For this reason, we pump the atoms into the  $F = 1$  ground state, when they are loaded in the optical dipole trap, to avoid the larger loss rate and thus a smaller lifetime (section 4.2).

For a pure exponential decay, the lifetime  $\tau$  of the dipole trap is inversely related to the one-body coefficient  $\alpha$ :

$$\tau = \alpha^{-1} = 17 \text{ s.} \quad (4.10)$$

However, since the dipole trap does not only suffer losses due to heating and background collisions, but also collisional two-body losses, the lifetime is given by the time for which the atom number has dropped down to  $N_0/e$ . The lifetime of our dipole trap with an initial particle number  $N(1 \text{ s}) = 310,000$  and density  $n(1 \text{ s}) = 3.0 \cdot 10^{13} \text{ atoms/cm}^3$  is then

$$\tau_{F=1} = 12 \text{ s.} \quad (4.11)$$

The lifetime of the  $F = 1$  ground state is long enough for the evaporation cycle, which has a typical duration of 6 s (section 4.5).

#### 4.1.2 Oscillation Frequencies

The oscillation frequencies, and thus the waist of the dipole trap (Eq. 3.26), can be measured through a parametric resonance [66], [67]. The intensity of the dipole trap laser is modulated with a sinusoidal signal, thereby oscillating the trap depth so that the atoms in the trap are forced to oscillate. If the oscillation frequency is twice the trap frequency of the dipole trap ( $\omega_{mod} = 2\omega_0$ ), the atoms are parametrically excited. The kinetic energy of the atoms on resonance increases exponentially with time and the atoms are heated out of the trap. The dipole potential is proportional to the square of the trap frequencies according to equation 3.26. Accordingly, we can take for a harmonic oscillator in a modulated potential:

$$U(x) = -\omega_0^2(1 + \epsilon \sin(\omega_{mod}t))x, \quad (4.12)$$

$\epsilon$  is the strength of the modulation. The solution of the equation shows resonances at  $\omega_{mod} = 2\omega_0/n$  for  $n = 1, 2, 3, \dots$ . As the width of the resonances decrease exponentially with  $n$ , we only expect to see the resonances  $\omega_{mod} = 2\omega_0$  and  $\omega_{mod} = \omega_0$  [66].

To determine the trap frequencies in our experiment, the intensity of the

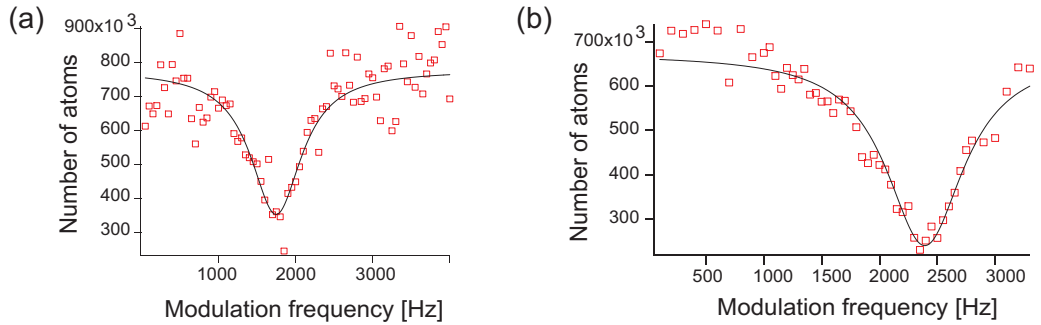


Fig. 4.2: Parametric heating. The atoms are trapped in a single beam trap, which is modulated in the intensity by 2%. The atoms are heated out of the trap, when the modulation frequency is twice the trap frequency. Figure (a) shows a resonance at 1.7 kHz for the single beam trap in the  $x$ -direction (Fig. 4.3). Figure (b) shows a resonance at 2.4 kHz for the single beam trap in the  $y$ -direction. A Lorentz profile was fitted to the data.

single beam dipole trap laser is modulated by 2%. The results are shown in figure 4.2. Resonances at twice the trap frequencies were measured at 1.7 kHz and 2.4 kHz for the single beam trap in the  $x$ - and  $y$ -direction, respectively. Combining equations 3.22 and 3.17 leads to the radial trap frequencies for the two single beam traps. The laser beam traveling in the  $x$ -direction had 4.3 W laser power, leading to a waist of the single beam trap of  $49 \pm 2 \mu\text{m}$ . The beam traveling in the  $y$ -direction had 3.45 W laser power, and thus the waist of the laser beam is  $40 \pm 2 \mu\text{m}$  in the focus. As a consequence, our dipole trap is slightly anisotropic.

The waist of the dipole trap laser beam traveling in the  $y$ -direction was also measured by moving a sharp edge in the laser beam, and measuring the decreasing intensity with a photodiode. By integrating the intensity profile, a Gaussian distribution is obtained, from which the waist can be determined. The waist of the beam was  $42 \pm 2 \mu\text{m}$ , which is in good agreement with the waist measured with the parametric heating experiment. The waist of the dipole trap laser beam traveling in the  $x$ -direction could not be measured due to experimental difficulties.

## 4.2 Loading the Atoms in the Dipole Trap

The first all-optical BEC has been made in the group of Chapman [6], where they have used a CO<sub>2</sub> laser with 10  $\mu\text{m}$  wavelength. The BEC was created in a crossed dipole trap, in which evaporative cooling was performed by ramping down the laser power. Since then, more groups have created an all-optical BEC with a CO<sub>2</sub> laser [68]. However, the diffraction limit

$$w_0 \approx \frac{\lambda f}{\pi w(f)}, \quad (4.13)$$

where  $w(f)$  is the waist of the laser beam at the position of the lens with focal length  $f$ , of the CO<sub>2</sub> laser is quite large due to its large wavelength. For this reason, other groups have tried to achieve Bose-Einstein condensation with smaller wavelengths. Another advantage is that lasers with smaller wavelengths can be used in combination with standard optical materials. The first BEC at a smaller wavelength was created by the experimental group of Weiss [9, 69]: They used a YAG laser with 1064 nm wavelength. Their setup was not a straightforward route to BEC: they first cooled rubidium atoms in an optical lattice and then loaded them into the crossed dipole trap. In 2006, a sodium BEC was created in a straight manner in the group of Lett [7]: The atoms were loaded directly from the MOT into the 1  $\mu\text{m}$  crossed optical dipole trap. Our way to quantum degeneracy is similar, as far as we know we are the first to have reached Bose-Einstein condensation of rubidium atoms with a 1  $\mu\text{m}$  dipole trap in a very simple and direct manner (section 4.5).

In our experiment, the dipole trap is continuously overlapped with the MOT. This has no visible effect on the atom number loaded in the MOT ( $N \sim 5 \cdot 10^9$  atoms), or on the number of atoms loaded in the dipole trap. The atoms are loaded straight from the MOT into the dipole trap by cooling them using a molasses (Fig. 4.3). The flux of atoms into the trapping volume depends on the density of the MOT, the temperature of the atoms and the parameters of the dipole trap [70]. Throughout the loading process, losses from the trap caused by heating mechanisms and collisional processes occur. Heating is caused by spontaneously scattered dipole trap laser photons, background gas collisions and intensity fluctuations. But for large numbers of atoms, the losses are dominated by collisional processes such as photoassociation, ground state hyperfine changing collisions and radiative escape. To obtain a large loading rate into the trap and as little losses as possible, the parameters

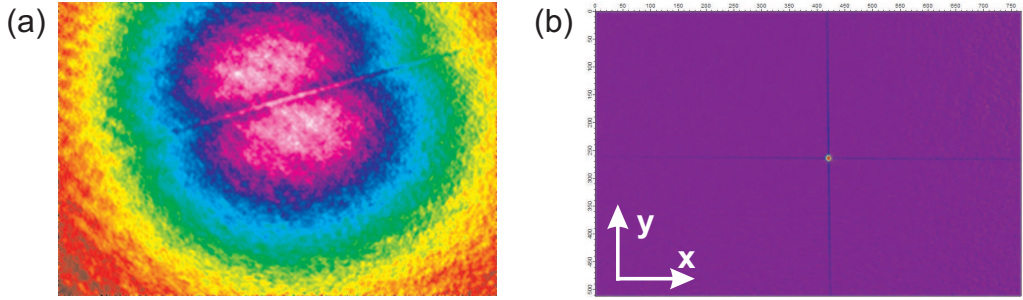


*Fig. 4.3:* The dipole trap is continuously overlapped with the MOT. The intensity of the MOT repumping and cooling laser is lowered during the loading process, to optimize the number of atoms loaded in the dipole trap. Simultaneously, the detuning of the MOT cooling laser is increased. (a) Single beam optical dipole trap overlapped with the MOT. The trapping volume is much larger than the trapping volume of the crossed dipole trap. (b) Crossed optical dipole trap with  $\sim 350,000$  atoms trapped in the crossing.

of the MOT have to be changed, starting with the duration of the loading phase. Figure 4.4(d) shows the number of atoms loaded in the trap as a function of the loading phase duration. Initially, the number of atoms loaded increases linearly in time, until a maximum is reached. For longer loading times the number of atoms loaded decreases, because of two reasons: First of all, the MOT loses atoms due to the changed detuning of the cooling laser for the molasses, and due to the reduced intensity of the repumping laser to pump the atoms into the  $F = 1$  ground state (section 4.1.1). Secondly, the dipole trap loss rates have become large enough to counteract the loading. The losses can be determined by a lifetime measurement, shown in figure 4.1.

In the loading process, the intensity of the repumping laser is lowered, so that a large proportion of the atoms are loaded in the  $F = 1$  ground state. Figure 4.4(a) shows the effect on the number of atoms loaded, when the intensity of the repumping laser is reduced. The repumping laser power in the normal MOT operation mode is 2.1 mW ( $I_{repump} = 2.7 \text{ mWcm}^{-2}$ ), and in the loading process it has to be reduced to  $\sim 1 \mu\text{W}$  to maximize the number of atoms loaded. For lower intensities of the repump laser, the loading rate decreases, because the MOT is not sustained. For larger intensities, the loading rate is larger due to the higher number of atoms in the MOT

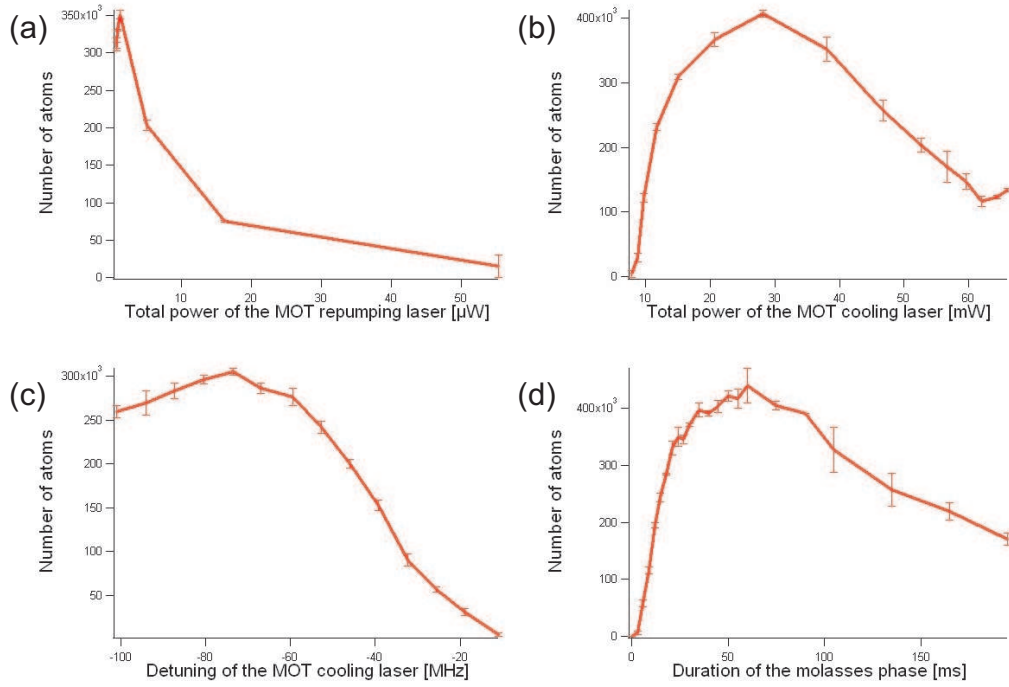


*Fig. 4.4:* Atoms loaded in the dipole trap as a function of (a) the repumping laser intensity, (b) the cooling laser intensity, (c) the cooling laser detuning from resonance, and (d) the duration of the loading phase. (a) The intensity of the repumping laser is decreased, so that the atoms are pumped into the  $F = 1$  ground state. The optimum repumping laser intensity is  $\sim 1 \mu\text{W}$ . The MOT is not sustained for lower intensities, and for higher intensities, the light induced losses increase. (b) The intensity of the MOT cooling laser has a similar effect on the number of atoms loaded in the dipole trap. (c) The light shift induced by the dipole trap increases the effective detuning of the atoms in the trap. The larger effective detuning reduces the excitation rate of the atoms in the dipole trap, and thus also reduces light induced collisions. At the same time, the cooling rate of the MOT is reduced, leading to a smaller loading rate in the dipole trap. (d) The number of atoms loaded increases linearly in time, until a maximum is reached. For longer loading times the number of atoms loaded decreases, because the MOT loses atoms due to the different detuning of the cooling laser and the reduced intensity of the repumping laser. Secondly, the trap loss rates have become large enough to counteract the loading.

and cooling rate, but the light induced loss rates also become larger with increasing repumping intensity. Another effect limiting the atom number is the radiative repulsion leading to a smaller density in the MOT and thus to a lower loading rate [58]. Reducing the repumping laser intensity increases the number of atoms loaded in the  $F = 1$  ground state, and thus removing them out of the cooling transition, thereby reducing the radiative repulsion.

Because the main losses are light induced, it is clear that the intensity of the cooling laser also has an effect on the number of atoms loaded. According to figure 4.4(b), the MOT cooling laser power has to be reduced from 70 mW (normal MOT laser power,  $I_{cool} = 91 \text{ mWcm}^{-2}$ ) to 30 mW ( $I_{cool} = 39 \text{ mWcm}^{-2}$ ) in the loading phase. Below this level, the MOT is not sustained.

The final parameter that has to be changed in the loading process is the MOT cooling laser detuning. Figure 4.4(c) shows the number of atoms loaded in the dipole trap versus the detuning of the MOT cooling laser. The MOT cooling laser is 15 MHz red detuned from resonance. However, the light shift induced by the dipole trap increases the effective detuning for the atoms in the trap:

$$\Delta_{eff} = \Delta_{MOT} - \Delta_{Stark}, \quad (4.14)$$

$\Delta_{MOT}$  is the detuning of the MOT lasers (15 MHz in our case) and  $\Delta_{Stark}$  is the Stark shift of the dipole trap. The Stark shift for a dipole trap with  $k_B \cdot 450 \text{ } \mu\text{K}$  trap depth is  $\omega_{shift} = \Delta E / \hbar = 2U_{Dip} / \hbar \approx 18 \text{ MHz}$ . The factor 2 comes from the fact that  $\Delta E$  is the shift of the ground and excited state and  $U_{Dip}$  is just the shift of the ground state. The larger effective detuning reduces the excitation rate of the atoms in the dipole trap, and thus also reduces light induced collisions. At the same time, the cooling rate of the MOT is reduced, leading to a smaller loading rate in the dipole trap. In addition, atoms are cooled down to sub Doppler temperatures by increasing the detuning of the cooling laser, thereby increasing the probability of trapping the atoms in the dipole trap (polarisation gradient cooling). The optimum detuning for a dipole trap with  $\sim k_B \cdot 450 \text{ } \mu\text{K}$  trap depth is  $\sim 75 \text{ MHz}$ . The optimized total number of atoms loaded in the dipole trap is  $\sim 3.5 \cdot 10^5$  at a temperature of  $\sim 30 \text{ } \mu\text{K}$ . As can be seen from equation 4.14, the optimum detuning depends on the optical dipole trap depth. A deeper trap means a larger light shift of the atoms, which means a reduced MOT cooling rate. For this reason, usually a smaller detuning is chosen for deeper traps [71, 70]. The detuning of the repumping laser is not changed in the loading process.

### 4.3 *Evaporative Cooling*

Evaporative cooling was first demonstrated with magnetically trapped hydrogen in 1988 [72], but was extended to alkali atoms in 1994 [3, 73]. It turned out to be the standard technique to cool atoms to low temperatures and high densities, because soon thereafter, a Bose-Einstein condensate was made [1, 2, 3]. The advantage of evaporative cooling is that it does not involve density limiting interactions with light. In general, evaporative cooling of a trapped gas is the removal of atoms with an energy higher than the average energy of the atom cloud. Atoms confined in a trap with depth  $U_{Dip}$  can leave the trap, when their energy  $E$  is larger than the trap depth  $U_{Dip}$ . This reduces the average energy of the remaining atoms and the atoms rethermalize through elastic collisions towards a new equilibrium at a lower temperature. The elastic collisions also provide new atoms with an energy  $E$  higher than the trap depth, thus the evaporation continues. As the temperature drops, the number of atoms that are able to leave the trap decreases exponentially, and the cooling and thus the evaporation stops. The evaporative cooling is continued by lowering the trap depth  $U_{Dip}$ .

Evaporative cooling in an optical dipole trap is performed by lowering the intensity of the dipole trap laser (Eq. 3.10). Unlike magnetic traps, where the trap depth is lowered with the radio-frequency-knife method, the trap strength changes during the evaporation as can be understood from equation 3.26 and seen in figure 4.5. The trap becomes shallower during the evaporation and the trap frequencies given by equation 3.26 are decreased. This is accompanied by a lower elastic collision rate and the evaporative cooling slows down. For this reason, high initial densities and trap frequencies are necessary to reach quantum degeneracy.

#### 4.3.1 *Colliding Atoms*

To evaporatively cool an atom cloud efficiently, many elastic collisions are necessary. This requirement is fulfilled when the atom cloud is trapped in a trap with high oscillation frequencies and has a high density. However, inelastic collisions are also density dependent. Therefore, the ratio between elastic and inelastic collisions has to be as large as possible, so that evaporative cooling is efficient.

To calculate the good-to-bad collisions ratio, the time between two succeeding elastic collisions has to be known. This depends on the elastic cross

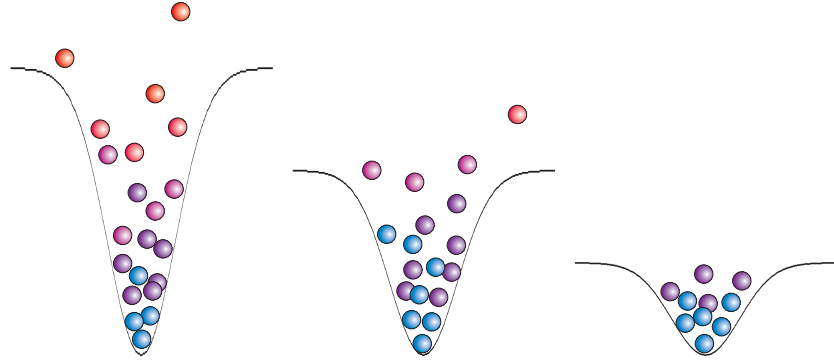


Fig. 4.5: By lowering the intensity of the dipole trap laser beam, the trap depth is reduced so that hotter atoms can leave the trap. The trap frequencies decrease during the evaporation, because the optical dipole trap reduces its curvature.

section  $\sigma$ , the density  $n$  of the atomic cloud and the average relative velocity  $\sqrt{2\bar{v}}$  of the two colliding atoms

$$\tau_{el} = \frac{1}{n\sigma\sqrt{2\bar{v}}} \quad (4.15)$$

where the elastic cross section is given by  $\sigma = 8\pi a$ , with  $a = 110a_0$  the scattering length of rubidium,  $a_0$  is the Bohr radius [38]. The average thermal velocity  $\bar{v}$  is given by

$$\bar{v} = \sqrt{\frac{8k_B T}{\pi m}}. \quad (4.16)$$

The elastic collision rate for atoms with a density of  $1.7 \cdot 10^{13} \text{ cm}^{-3}$  confined in a trap with a depth of  $\sim k_B \cdot 300 \text{ } \mu\text{K}$ , and having a temperature of  $\sim 30 \text{ } \mu\text{K}$  (this particular trap was used to create a condensate in, see section 4.5), is

$$\Gamma_{el} = \frac{1}{\tau_{el}} = 1788 \text{ s}^{-1}. \quad (4.17)$$

The inelastic collision rate can be found by adding up the collision rates of each density independent loss coefficients:

$$\Gamma_{inel} = \frac{1}{\tau_{inel}} = \alpha + \beta'n + \gamma'n^2. \quad (4.18)$$

Although the three-body losses  $\gamma'$  were neglected in the lifetime measurements, they become more and more significant as the density increases during the evaporation, due to their dependence on the density squared. This means that the ratio between the elastic and inelastic collisions will decrease throughout the evaporation, because the density increases. The ratio is given by:

$$R(T, n) = \frac{\Gamma_{el}}{\Gamma_{inel}}, \quad (4.19)$$

and should have a value  $R > 500$  [74, 75] throughout the evaporation process for efficient evaporative cooling. The lifetime measurements showed that our main losses result from heating and collisional processes, therefore the initial ratio  $R_0$  for an atom cloud with a density of  $1.7 \cdot 10^{13} \text{ cm}^{-3}$  is given by

$$R_0 = \frac{\tau_{el}^{-1}}{\alpha + \beta'n} = 1.9 \cdot 10^4. \quad (4.20)$$

This is an upper limit, because the one-body loss coefficient  $\alpha$  is probably larger for reasons explained in section 4.1.1. Nevertheless, the ratio  $R_0$  shows a good starting condition for the evaporative cooling in our optical dipole trap with a depth of  $\sim k_B \cdot 300 \text{ } \mu\text{K}$ .

During the evaporation, the atoms need on average 4 – 5 collisions to thermalize at a lower temperature [71, 75]. Due to the high oscillation frequencies of our optical dipole trap, and the high elastic-inelastic collisions ratio, we can reach the quantum degenerate regime much faster and with a lower atom loss than in a magnetic trap. In magnetic traps, the oscillation frequencies usually are 10 – 50 Hz in the axial direction, and  $\sim 400$  Hz in the radial direction, whereas the oscillation frequencies of an optical dipole trap are several kHz. The quantum degenerate regime in a magnetic trap can be reached in half a minute, but only takes a few seconds in a dipole trap (Fig. 4.6). The atom loss in a magnetic trap is a factor of 100 – 1000, in our dipole trap, we only lose a factor of 35 – 40 in atom number. Therefore, the dipole trap is more efficient. Nevertheless, the trapping volume in a dipole trap is quite small. More atoms can be trapped in a magnetic trap ( $N = 10^8$ ), thus condensates with a high atom number can be obtained. In our dipole trap, we can only trap  $\sim 350,000$  atoms (see section 4.2).

### 4.3.2 Evaporating Atoms

As mentioned before, the dipole trap strength decreases during the evaporation process, leading to a decrease in the oscillation frequencies and thus the elastic collision rate, because the elastic collision rate (Eq. 4.15) depends on the trap frequencies through the density  $n$  (Eq. 4.40). The final densities and temperatures reached with evaporative cooling are determined by how the dipole trap strength changes during the evaporation: High densities and high trap frequencies apply for a faster evaporation ramp, and low densities and/or trap frequencies demand a slower evaporation ramp. This means that the evaporation ramp for atoms in an optical dipole trap starts with a steep slope, which flattens out for longer evaporating times.

The atoms in our experiment are evaporatively cooled by ramping down the laser power with the two AOMs (Fig. 3.9) with three linear ramps. The decrease in laser power of both beams is kept equal throughout the evaporation, but can be adjusted independently, if necessary. The first ramp is a steep slope, because of the high initial density and rethermalisation time (section 4.3.1). The two following ramps are more moderate, thus taking the changing dipole strength into account. The speed of the evaporation ramp is very important: If the trap depth is ramped down too fast, the atoms do not have the time to thermalize and the evaporative cooling is not efficient. On the other hand, if the trap depth is ramped down too slow, losses due to inelastic collisions become more and more important, and the evaporative cooling is also not efficient.

Scaling laws describing the evolution of the phase space density and the atom number during the evaporative cooling in time dependent optical traps were derived by O'Hara [76]. The scaling laws depend on the so-called cut-off parameter  $\eta = \frac{U_{Dip}}{k_B T}$ , the ratio of the trap depth and the energy of the atoms. The cut-off parameter  $\eta$  is usually 10 for optical dipole traps [76], which could be confirmed for our dipole trap in the case for when gravitation does not play a role (see section 4.5). The parameter tells us that when the trap depth is lowered such that the value of  $\eta$  is smaller than 10, the atoms evaporate out of the trap until  $\eta = 10$  again.

The phase space density  $\rho_{psd}$  is increased during the evaporation, and scales with the trap depth and the atom number as

$$\frac{\rho_{psd}}{\rho_{psd,ini}} = \left( \frac{U_{ini}}{U} \right)^{\frac{3(\eta'-4)}{2(\eta'-3)}} = \left( \frac{N_{ini}}{N} \right)^{\eta'-4}, \quad (4.21)$$

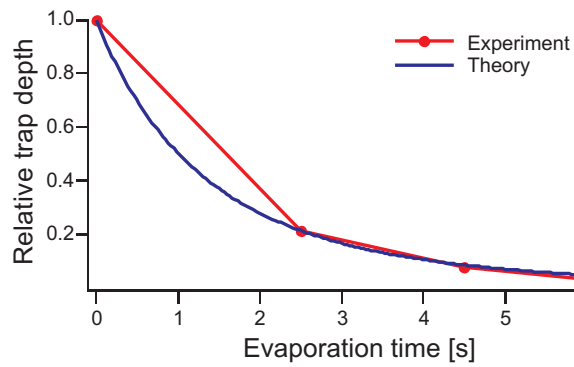


Fig. 4.6: The atoms are evaporatively cooled by ramping down the AOMs (Fig. 3.9) with three linear ramps. Each ramp is empirically determined by measuring the temperature and the number of atoms after each ramp. The optimum duration of the ramp is the one where we obtain the most atoms for a given final laser power, which determines the lowest temperature of the atoms that can be reached. The graph was fitted by the equation describing the time dependent potential depth (Eq. 4.24),  $\frac{1}{\tau} = 0.18$  and  $\frac{-2(\eta'-3)}{\eta'}$  determined by the fit is  $-4.1$ . The equation does not take inelastic collisions into account.

where the subscript *ini* denotes the initial condition of the parameter, and  $\eta' = \eta + \frac{\eta-5}{\eta-4}$ . The speed of the evaporation is determined by the elastic collision rate  $\Gamma_{el}$  (Eq. 4.17). Because the trap becomes less curved for lower intensities, the collision rate decreases. The decrease of the collision rate is given by:

$$\frac{\Gamma_{el}}{\Gamma_{el,ini}} = \left( \frac{U}{U_{ini}} \right)^{\frac{\eta'}{2(\eta'-3)}}. \quad (4.22)$$

The evaporation rate is given by the s-wave Boltzmann equation [77]:

$$\dot{N} = -2(\eta - 4)e^{-\eta}\Gamma_{el}N. \quad (4.23)$$

Combining this equation with equation 4.21 leads to a time dependent potential depth:

$$\frac{U(t)}{U_{ini}} = \left( 1 + \frac{t}{\tau} \right)^{\frac{-2(\eta'-3)}{\eta'}}, \quad (4.24)$$

the time constant  $\tau$  is given by:

$$\frac{1}{\tau} = \frac{2}{3}\eta'(\eta - 4)e^{-\eta}\Gamma_{el,ini}. \quad (4.25)$$

Equation 4.24 resembles an exponential, which has been approximated in our experiment by three linear ramps (Fig. 4.6). The slope of each ramp is determined empirically by measuring the number of atoms and the temperature of the atoms at the end of each ramp. The optimum duration of the ramp is the one where we obtain the most atoms for a given final laser power, which determines the lowest temperature of the atoms that can be reached. The experimental evaporation curve was fitted with the equation for the time dependent trap depth (Eq. 4.24). The fitted parameters  $\frac{1}{\tau} = 0.18$  and  $\frac{-2(\eta'-3)}{\eta'} = -4.1$  with  $\eta = 4.5$  are smaller than expected ( $\frac{1}{\tau} = 3.5$  and  $\frac{-2(\eta'-3)}{\eta'} = -1.4$ , where we have taken  $\eta = 10$  and  $\Gamma_{el} = 1788$ , see equation 4.17), because the equation does not take inelastic collisions into account. In addition, we have observed in our experiments that our cut-off parameter  $\eta$  decreases during the evaporation. At the end of the evaporation cycle, the temperature of the atom cloud equals the trap depth ( $\eta \sim 1$ ).

#### 4.4 Detecting a Bose-Einstein Condensate

Section 3.3.6 explained the imaging technique we use to determine the atom number of our sample. However, to determine the temperature or the waist

of the cloud, we have to fit the sample with a density distribution. All the properties of thermal clouds and condensates can be obtained from the density distribution by comparing the measured density distribution with models of the dilute atom gas. These density distribution models are well understood for thermal atom clouds ( $T \geq T_c$ ) and pure condensates, but in the intermediate region where the cloud is partly condensed and partly still thermal, the density distributions can only be approximated.

The optical dipole potential can be approximated with a harmonic potential:

$$U(\vec{r}) = \frac{1}{2}m(\omega_x^2 x^2 + \omega_y^2 y^2 + \omega_z^2 z^2). \quad (4.26)$$

The distribution density for a thermal cloud in this harmonic potential is then (see also Eq. 2.9):

$$n_T(\vec{r}) = \frac{1}{\Lambda_{dB}^3} g_{3/2}(e^{\mu - (U(\vec{r}))/k_B T}). \quad (4.27)$$

The semiclassical approach can also be used to determine the distribution after a time of flight (TOF): When the trap is switched off, the atoms fly ballistically in every direction with the velocity they had at the time of the switching off. The distribution as a function of the expansion time  $t$  is given by [33]:

$$n_{TOF}(\vec{r}, t) = \frac{1}{\Lambda_{dB}^3} \sum_{i=x,y,z} \left( \frac{1}{1 + \omega_i^2 t^2} \right) \cdot g_{3/2} \left( e^{\mu - \frac{m}{2} \left( \sum_{i=x,y,z} i^2 \left( \frac{\omega_i^2}{1 + \omega_i^2 t^2} \right) \right)} \right) / k_B T. \quad (4.28)$$

As mentioned in section 2.2.1, the expansion of an ideal thermal cloud is isotropic for large expansion times, and the density profile can be approximated by:

$$n_{TOF}(\vec{r}, t) = \frac{1}{\Lambda_{dB}^3} g_{3/2}(e^{\mu - \frac{m\vec{r}^2}{2t^2} / k_B T}). \quad (4.29)$$

In the case of a (pure) condensate in a harmonic potential, the density distribution in the Thomas-Fermi approximation is given by (see also Eq. 2.35):

$$n(\vec{r}) = \max \left\{ \frac{[\mu - U(\vec{r})]}{g}, 0 \right\}. \quad (4.30)$$

The condensate can be seen as filling up the bottom of the trapping potential up to a "height" given by the chemical potential  $\mu$ .

The expansion of the condensate is anisotropic, when the trapping potential is anisotropic: The interaction energy is converted in kinetic energy upon release, and the anisotropy is increased (section 2.2.2). The parabolic form of equation 4.30 is thereby conserved, just the axes are rescaled [78]. The radii of the condensate scale as:

$$R_i(t) = R_i(0)b_i(t) = \sqrt{\frac{2\mu}{m\omega_i(0)^2}}b_i(t), \text{ with } i = x, y, z, \quad (4.31)$$

where the time dependent scaling factor  $b_i(t)$  satisfies the differential equation

$$\ddot{b}_i + \omega_i(t)^2 b_i - \frac{\omega_i(0)^2}{b_i b_x b_y b_z} = 0, \text{ with } i = x, y, z. \quad (4.32)$$

The equations of the scaling parameters can be simplified by considering an axially symmetric harmonic potential ( $\omega_1 = \omega_2 \equiv \omega_\perp$  and  $\omega_3 \equiv \omega_z$ ), which is turned off at  $t = 0$ :

$$\begin{aligned} \frac{d^2}{d\tau^2} b_\perp &= \frac{1}{b_\perp^3 b_z} \\ \frac{d^2}{d\tau^2} b_z &= \frac{\ell^2}{b_\perp^2 b_z^2}, \end{aligned} \quad (4.33)$$

$\tau$  is a dimensionless time variable, given by  $\tau = \omega_\perp(0)t$ , and  $\ell = \frac{\omega_z(0)}{\omega_\perp(0)}$ . The equations can be solved analytically for  $\ell \ll 1$ , leading to the equations:

$$\begin{aligned} b_\perp(\tau) &= \sqrt{1 + \tau^2} \\ b_z(\tau) &= 1 + \ell^2 \left( \tau \arctan \tau - \ln \sqrt{1 + \tau^2} \right). \end{aligned} \quad (4.34)$$

The solutions to the differential equations show three stages of the free expansion: The first stage is where the interaction energy is converted in kinetic energy ( $\tau < 1$ ). Figure 4.7a shows the conversion into kinetic energy for an anisotropic optical dipole trap in  $\sim 1$  ms. The second stage shows the expansion of both directions, whereby the expansion in the direction of the tighter confinement (higher trap frequencies) is large, and the expansion in the second direction is much smaller ( $1 < \tau < \ell^2$ ). The third stage shows an asymptotic behaviour of the aspect ratio  $\frac{R_\perp}{R_z} = \frac{\pi\ell^2}{2}$  ( $\ell^2 < \tau$ ). In figure 4.7(b), this asymptotic behaviour is not visible.

With the absorption imaging technique only column densities along the imaging axis can be measured. The pictures obtained are thus two-dimensional, and the density distribution for the thermal cloud changes into

$$\tilde{n}_T(x, y) = \frac{\tilde{n}_T(0)}{g_2(e^{\mu/k_B T})} g_2(e^{(\mu - \frac{m}{2}(\omega_x^2 x^2 + \omega_y^2 y^2))/k_B T}) \quad (4.35)$$

where the imaging axis is in the  $z$  direction. The thermal cloud can also be fitted with a Gaussian distribution for temperatures above the critical temperature:

$$n_{fit,T}(x, y) = e^{-\frac{x^2}{2\sigma_x^2} - \frac{y^2}{2\sigma_y^2}}. \quad (4.36)$$

The fit improves for higher temperatures, because  $e^{\mu/k_B T} \ll 1$  for  $T \gg T_c$  and  $g_2(x) \approx x$  when  $x \ll 1$ .

As mentioned before, partly condensed clouds can only be approximated with a density distribution. Section 2.2.1 already mentioned the bimodal behaviour of a partly condensed cloud. This feature is used in the density distribution fit: The Gaussian distribution and the parabolic distribution are added up, where the Gaussian distribution describes the thermal cloud, and the parabolic distribution describes the condensate fraction. The density distribution becomes [33]

$$\begin{aligned} n_{fit}(x, y) &= \frac{\tilde{n}_T(0)}{g_2(1)} g_2\left(e^{-\frac{x^2}{2\sigma_x^2(t)} - \frac{y^2}{2\sigma_y^2(t)}}\right) \\ &+ \tilde{n}_{BEC}(0) \max\left\{1 - \frac{x^2}{R_x^2(t)} - \frac{y^2}{R_y^2(t)}, 0\right\}. \end{aligned} \quad (4.37)$$

The temperature of the cloud is determined by the radii of the thermal cloud  $\sigma_i$ . To obtain the temperature of the partly condensed cloud, the fit should be limited to the thermal part, where the condensed atoms are absent, to prevent errors due to the interaction energy. The temperature of the cloud is given by:

$$k_B T = m \left( \frac{\omega_i^2 \sigma_i^2}{1 + \omega_i^2 t^2} \right), \quad \text{with } i = x, y, \quad (4.38)$$

where  $t$  is the expansion time. By measuring the radii of the cloud for several expansion times  $t_1$  and  $t_2$ , the temperature can be determined by

$$T = \frac{m}{k_B} \frac{\sigma_{i,1}^2 - \sigma_{i,2}^2}{t_1^2 - t_2^2}, \quad \text{with } i = x, y. \quad (4.39)$$

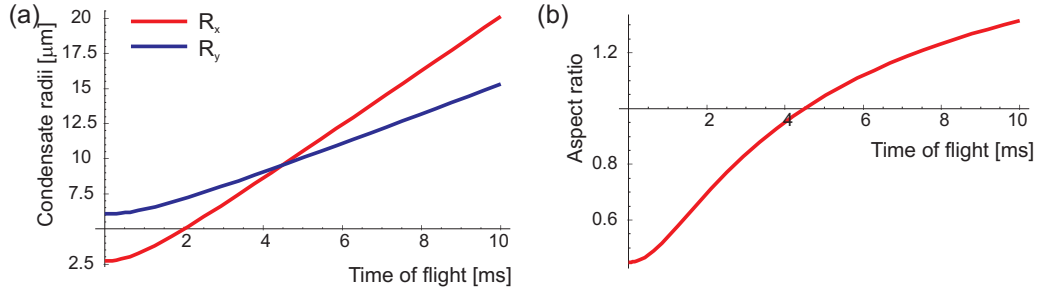


Fig. 4.7: (a) The graph shows the numerical solution to the differential equations describing the expansion of a Bose-Einstein condensate during a time of flight (Eqs. 4.31 and 4.32). (b) The changing aspect ratio derived numerically. The  $1/e^2$  radii of the two beams in the crossing are  $72 \mu\text{m}$  and  $40 \mu\text{m}$  in the  $x$  and  $y$  direction, respectively. The corresponding trap frequencies are  $\omega_x = 2\pi \times 125 \text{ Hz}$  and  $\omega_y = 2\pi \times 56 \text{ Hz}$ .

#### 4.5 Bose-Einstein Condensation

Bose-Einstein condensation is reached when the phase space density of the cloud is larger than 2.612 (Eq. 2.10). The phase space density can be determined from known trap parameters, by measuring the temperature of the cloud and the number of atoms  $N$ . Through the number of atoms we obtain the density of the cloud in the trap, by dividing it with the effective volume  $V_{eff}$  of the trapping potential:

$$n = \frac{N}{V_{eff}} \text{ with} \\ V_{eff} = \left( \frac{2\pi k_B T}{m} \right)^{3/2} \frac{1}{\bar{\omega}^3}, \quad (4.40)$$

$\bar{\omega} = (\omega_x \omega_y \omega_z)^{1/3}$  is the geometric mean of the trap frequencies. Nevertheless, determining the phase space density to prove that we have reached quantum degeneracy is not enough.

The onset of BEC is usually accompanied by the formation of a sharp peak in the density distribution of the atomic cloud. When this is observed and the bimodal function (Eq. 4.37) can be fitted to the distribution, we have a clear indication that we have reached Bose-Einstein condensation. Another means of detecting the onset of Bose-Einstein condensation is given

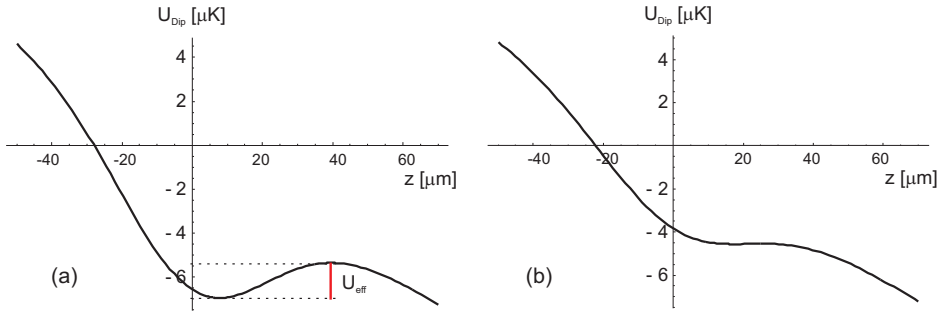


Fig. 4.8: The dipole potential under the influence of gravity. The waists of the beams are  $50 \mu\text{m}$  and  $40 \mu\text{m}$  in the  $x$  and  $y$  direction respectively. (a) The total laser power in the crossing is  $120 \text{ mW}$ , according to equation 3.17 is the trap depth  $U_{Dip} = 6.6 \mu\text{K}$ , however the effective potential depth is  $U_{eff} = 1.6 \mu\text{K}$ . (b) The gravity has opened the trap such that the atoms cannot be contained in the trap. The total laser power in the crossing is  $70 \text{ mW}$ .

by the three-body recombination: The three-body loss rate is a factor of 3! smaller in a condensate than in a thermal cloud of the same density [79], [65]. Nonetheless, we use the special feature of the BEC that it converts its interaction energy into kinetic energy when the trap is suddenly switched off, because it turned out to be impracticable to fit the bimodal function to our cloud for several reasons. First of all, gravity affects the dipole trap potential. The atoms are attracted to the bottom of the dipole trap, so that the center of the trapping potential is moved downwards. This effect is negligible for strongly confining optical dipole traps, but it cannot be ignored when the trap depth is lowered, for instance during the evaporation. The influence of the gravity is added up to the dipole potential (Eq. 3.17) to obtain the effective dipole potential:

$$U_{eff} = U_{Dip}(x, y, z) - mgz. \quad (4.41)$$

Figure 4.8 shows the influence of gravity on the dipole potential. As can be clearly seen, gravity lowers the potential barrier seen by the atoms. A typical value for the laser power at the end of the evaporation cycle is  $P_{tot} = 120 \text{ mW}$ . In this case, the effective dipole potential is only  $1.6 \mu\text{K}$ , four times lower than the dipole potential calculated with equation 3.17. When the laser intensity is lowered even more, the barrier is decreased until there is no

potential left to confine the atoms. This happens at a total laser power of 70 mW (Fig. 4.8(b)). At this point, the gravity is in equilibrium with the trapping potential. Atoms can be trapped in an optical dipole potential as long as the energy  $k_B T$  of the atoms is lower than the potential barrier.

Unfortunately, the (partly condensed) atom clouds we have observed were all trapped in a potential with a barely existing potential barrier. Which means that the cloud could expand outside the potential barrier, before the trap was switched off, leading to a bimodal distribution regardless of the fact whether we had reached quantum degeneracy or not. This problem is easily solved by adding a second detection setup in the horizontal direction ( $x, y$  direction).

Secondly, it is possible that we have trapped partly condensed clouds where the thermal cloud is almost nonexistent. According to reference [80, 81], a shallow optical dipole potential cannot be approximated with a parabolic potential, since the anharmonicity of the trapping potential has to be taken into account. Approximating the potential with a Gaussian leads to much higher condensate fractions.

In addition to reaching high enough phase space density  $\rho_{psd}$ , we based our proof of Bose-Einstein condensation on the anisotropic expansion of a quantum degenerate gas trapped in an anisotropic trap. Our trap is already slightly anisotropic (the waist of the beam travelling in the  $x$  direction is 49  $\mu\text{m}$ , and in the  $y$  direction it is 40  $\mu\text{m}$ ), but we increased the anisotropy of the trap by moving one focus several mm out of the crossing to increase the  $1/e^2$  radius of the beam in the crossing point. The focus of the beam travelling in the  $x$  direction was moved 8 mm outside of the crossing point, so that the  $1/e^2$  radius of the beam in the crossing became 72  $\mu\text{m}$  (Eq. 3.19). Figure 4.9 shows the anisotropic dipole trap and the TOF images of the evaporated cloud. As can be clearly seen in 4.9(b) and 4.9(c), the cloud changed its aspect ratio during the free expansion. The orientation of the cloud changed from a vertical orientation to a horizontal orientation in 6 ms.

Since we do not have an axially symmetric trap, we have numerically calculated the differential equations of the scaling parameters of the condensate radii (Eq. 4.32), to obtain the changing aspect ratio predicted by theory [78]. The parameters used for the calculation resembled the experimental parameters: The  $1/e^2$  radii of the two beams in the crossing are 72  $\mu\text{m}$  and 40  $\mu\text{m}$  in the  $x$  and  $y$  direction, respectively. The corresponding trap frequencies at the end of the evaporation cycle are  $\omega_x = 2\pi \times 125$  Hz and  $\omega_y = 2\pi \times 56$  Hz. The results are shown in figure 4.7. The theoretical aspect ratio of the

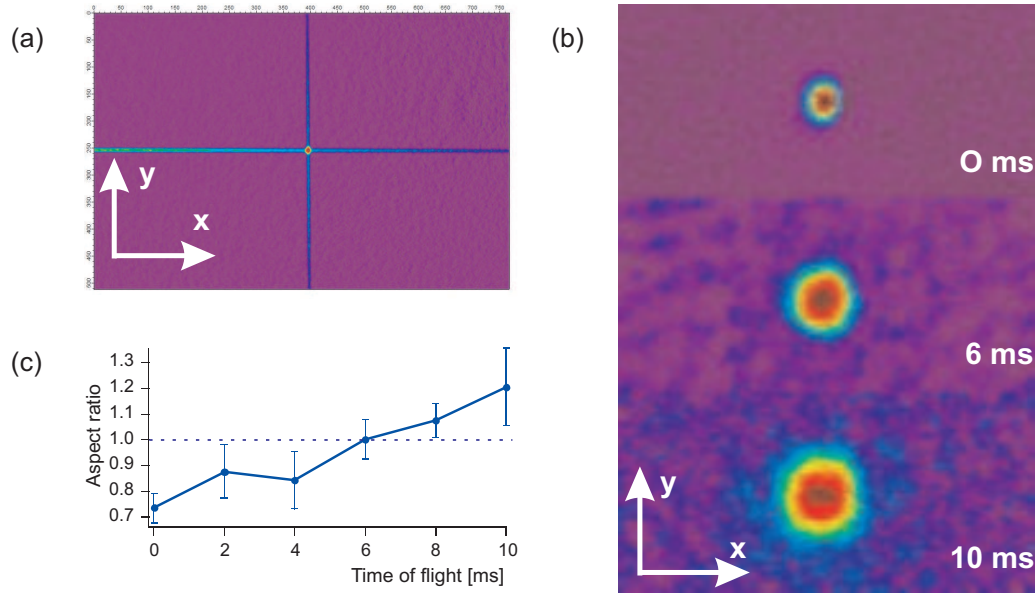


Fig. 4.9: A Bose-Einstein condensate. The aspect ratio of the cloud changed during its free expansion. (a) The focus of the beam travelling in the  $x$  direction was moved 8 mm outside of the crossing point, so that the  $1/e^2$  radius of the beam in the crossing became  $72 \mu\text{m}$ . The waist of the second beam was  $40 \mu\text{m}$ . (b) Time of flight (TOF) images of the condensate. (c) Aspect ratio  $R_x/R_y$  versus the time of flight.

Optical power after evaporation	$P$	120 mW
$1/e$ waist in the crossing ( $x$ -direction)	$w_x$	$40 \mu\text{m}$
$1/e$ waist in the crossing ( $y$ -direction)	$w_y$	$72 \mu\text{m}$
Final trap depth	$U_{Dip}/k_B$	$4.3 \mu\text{K}$
Critical temperature	$T_c$	100 nK
Phase space density	$\rho_{psd}$	$> 3$
Number of atoms	$N$	10,000
Number of condensed atoms	$N_c$	5,000
Initial aspect ratio ( $t_{TOF} = 0$ ms)	$R_x/R_y$	0.73
Final aspect ratio ( $t_{TOF} = 10$ ms)	$R_x/R_y$	1.20

Tab. 4.1: Parameters of the dipole trap and the Bose-Einstein condensate.

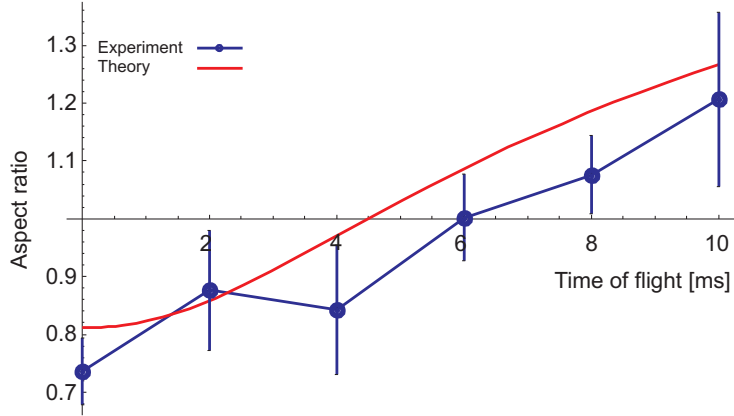


Fig. 4.10: The theoretical curve shown in figure 4.7b was weighted with the camera resolution, 1 pixel  $\hat{=} 7 \mu\text{m}$ :  $R_{i,new} = \sqrt{R_i^2 + (7 \cdot 10^{-6})^2}$ .

cloud at  $t = 0$  ms is much larger than the measured aspect ratio, since in the calculation we have not taken the camera resolution into account. We have a small magnification  $M = 1.3$  in our camera setup. Combined with the size of our camera pixel (one pixel is  $9 \mu\text{m}$ , section 3.3.6), this leads to the minimum size of  $7 \mu\text{m}$  we can image with the camera. The theoretical curve shown in figure 4.7b was weighted with the camera resolution and the resulting curve is shown in figure 4.10.

Figure 4.10 shows that the theory nicely confirms our experimental data, considering all the assumptions we have made. Each data point consists of at least 3 – 5 measurements. We estimate that 10% of these measurements consisted of clouds which did not reach Bose-Einstein condensation, and thus were thermal clouds with an isotropic expansion. This decreases the aspect ratio value. Another assumption we have made was with the fitting process: The data was fitted with a Gaussian distribution instead of with a bimodal distribution, since the data could not be accurately fitted with the bimodal function.

The  $1/e^2$  radii of the laser beams also show an error of about 10%: The displacement of the beam travelling in the  $x$  direction could be measured with an accuracy of 1 mm. A larger  $1/e^2$  radius leads to a downward movement of the aspect ratio function.

Table 4.1 shows some parameters of our optical dipole trap and the con-

densate.

## 4.6 Summarizing the Route to BEC

In this chapter, I have proved that we have reached Bose-Einstein condensation in an optical dipole trap in a simple and straightforward way. We start our experiment by loading  $\sim 350,000$  atoms from the MOT into the crossed dipole trap. 70% of the atoms in the dipole trap is optically pumped into one  $m_F$  state. We have optimized the number of atoms trapped in the dipole trap by decreasing the intensity of the repumping and cooling laser, and by increasing the detuning from resonance of the cooling laser. Thereby reducing the light induced losses. Due to the decreased intensity of the repumping laser, the atoms are pumped into the  $F = 1$  ground state. This increases the lifetime of atoms trapped in the dipole trap from less than 1 s for atoms in the  $F = 2$  ground state, to 12 s for atoms in the  $F = 1$  ground state (Fig. 4.1). The high oscillation frequencies of our dipole trap and low losses allow for a high ratio between the elastic and inelastic collisions (Eq. 4.20), which we need for an efficient evaporative cooling process. The atoms are evaporated by ramping down the laser power with three linear ramps. At the end of our evaporation cycle, we are left with about 10,000 atoms at a temperature below the critical temperature  $T_c \simeq 100$  nK. We proved Bose-Einstein condensation through the changing aspect ratio. The cloud changed its aspect ratio in a time of flight of 10 ms from 0.7 to 1.2, thereby confirming our theoretical prediction, thus proving quantum degeneracy. Our atomic cloud consists of  $\sim 5,000$  condensed atoms. The temperature of quantum degenerate clouds are usually determined by fitting a density distribution to the thermal part of the cloud. Due to the fact that our clouds can expand outside the (low) potential barrier of the optical dipole trap, before the trap is switched off, we cannot accurately determine the temperature of our quantum degenerate clouds.



## 5. USING THE COHERENCE PROPERTIES OF BOSE-EINSTEIN CONDENSATES

### *Overview of this Chapter*

In this chapter, a novel realisation for Sagnac interferometry is proposed. In this experiment, we want to load a Bose-Einstein condensate into a ring-shaped potential created by illuminating a microfabricated microoptical ring-lens. The diameter of the ring is 1.5 mm with a waist of 1.2  $\mu\text{m}$  (section 5.2). The small waist leads to a tight confinement of the Bose-Einstein condensate and can lead to a 1D BEC or even a Tonks-Girardeau gas (section 5.3).

### *5.1 Introduction*

Now that we have proved to have reached Bose-Einstein condensation, we want to use the coherence properties of the condensate to study several effects. In this respect, the atom interferometer is a very powerful tool: It can be used to study fundamental quantum mechanical phenomena, probe atomic and material properties, and measure inertial displacements. To perform atom interferometry experiments, our experimental setup has to satisfy several conditions. First we have to prepare our initial state, in our case this is the Bose-Einstein condensate. Then, we have to coherently split the condensate and apply interactions to the two parts (or two quantum states), which affect the clouds differently. Now, the two clouds can be recombined and the phase shift can be measured by detecting the fringes of the interference pattern.

In our experiment, we want to use a microfabricated ring-lens as an atom interferometer. When the ring-lens is illuminated by a laser, a ring-shaped focus is imaged in the focal plane. Atoms can be loaded in this ring-shaped potential, given by equation 3.17. The advantage of using an atom interferometer that confines atoms is that the atoms are supported against gravity.

This leads to largely enhanced experiment times, which is advantageous for precision experiments. Another advantage is that the location of the atoms can be known with high precision. This is important for experiments where spatially varying fields or interactions with small objects are studied. However, the density in "confined" atom interferometers is high to acquire high signals. This comes with several disadvantages, namely that the matter waves become nonlinear due to the interatomic interactions leading to a mean field potential. In the case of atoms trapped in a double well potential, this causes a relative frequency shift between atoms in the two wells. When the double well potential reverts into a single well potential, the nonlinear interaction can create solitons. Solitons enhance the sensitivity of phase measurements, but are hard to control [82]. Releasing the BECs before they are overlapped averts problems arising from the nonlinearity.

The ring can be used as a Sagnac interferometer. In 1913, Sagnac showed that the phase in a ring interferometer is sensitive to rotation. The Sagnac effect for light is given by:

$$\delta\phi = \frac{8\pi A\Omega}{\lambda c}, \quad (5.1)$$

and in the case for atoms:

$$\delta\phi = \frac{8\pi A\Omega}{\lambda_{dB}v} = \frac{4m A\Omega}{\hbar}, \quad (5.2)$$

where  $A$  is the enclosed area of the interferometer,  $\Omega$  is the rotation, and  $\delta\phi$  is the phase shift. Due to the de Broglie wavelength, the Sagnac effect is more sensitive when atoms are used. The sensitivity can even be enhanced when massive particles are used. Nevertheless, atom interferometers largest disadvantage (and thus a big advantage for light) is the small areas that can be used. In a fiber ring interferometer, the enclosed area can be as large as  $10^8 \text{ m}^2$ , whereas the enclosed areas for atom interferometers is only a few  $\text{mm}^2$  [82, 15]. Nonetheless, a larger sensitivity should be possible with an atom interferometer when cold atoms are used.

A few groups have created a magnetic storage ring for Sagnac interferometry in which they loaded neutral atoms [83, 84]. However, using optical potentials instead of magnetic potentials to create a ring has several advantages. Because our ring-shaped trap is all-optical, it does not involve material surfaces, as is the case for magnetic ring traps, which can cause matter wave decoherence. Furthermore, it allows for the possibility of trapping multiple magnetic sublevels and the investigation of multi-component

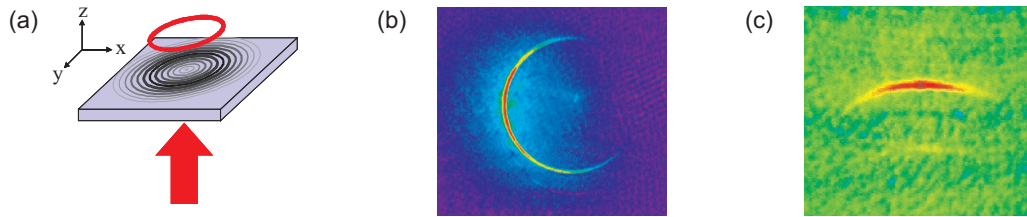


Fig. 5.1: (a) A schematic representation of the microfabricated ringlens. In our experimental setup, the focus of the ring lies in the  $xy$  plane specified by the crossed dipole trap beams (Fig. 4.3) (b) Rubidium 87 atoms were loaded in the ringlens straight from our MOT and were able to propagate freely along the ring. (c) Rubidium 87 atoms were loaded in the ringlens from the optical dipole trap by cooling the atoms in the dipole trap through evaporation. The atoms in the ring are not quantum degenerate.

(one-dimensional) gases.

## 5.2 The Microfabricated Ring-Lens

The microfabricated ring-lens was made by bending a cylindrical diffractive microlens into a ring with a maximum outer diameter of the diffractive element of 3 mm. The ring-lens was made in collaboration with the research group of Jahns at the "Fernuniversität Hagen". The ring-lens images a ring-shaped focus in its focal plane ( $F = 2$  mm), as can be seen in figure 5.1(a). The diameter of the ring-focus is 1.5 mm, and the minimum waist of the ring-focus is  $1.2 \mu\text{m}$ . This waist can only be reached when the numerical aperture of the following optical elements is large enough so that lens aberrations and intensity losses do not occur.

The ring-lens is illuminated by a Ti:Sapph laser at 796 nm, and the resulting focus is imaged 1 : 1 into the vacuum chamber. The ring-focus lies in the horizontal  $xy$  plane as specified by the crossed dipole trap beams (Fig. 4.3). The intensity in the focus of the ring-lens is given by [85]

$$I_0 = \frac{P}{\sqrt{2\pi}Rw_0}. \quad (5.3)$$

The dipole trap depth can then be calculated through equation 3.17. We have about 400 mW laser power at our disposal to illuminate the ring-lens,

leading to a maximum trap depth  $U_0 = k_B \cdot 0.4$  mK, where it is assumed that the waist of the ring-focus is  $2 \mu\text{m}$ . The trap frequencies can be calculated with the equations for the single beam dipole trap (Eqs. 3.22 and 3.23), and the radial trap frequency  $\omega_r = 2\pi \cdot 30$  kHz and the axial trap frequency  $\omega_z = 2\pi \cdot 3$  kHz. The confinement of the atoms in the ring-lens trap is therefore very tight, this can lead to interesting effects when we load a BEC in the ring. These effects are described in the following section.

Figure 5.1(b) shows rubidium atoms in the ring, which were loaded directly from the MOT. In figure 5.1(c), the ring is superimposed with the dipole trap. Atoms are loaded in the ring by evaporatively cooling the atoms in the dipole trap. The atoms in the ring are not quantum degenerate, so far we have not been able to load a BEC in the ring.

### 5.3 1D Quantum Degenerate Gases in a Toroidal Trap

Loading a Bose-Einstein condensate into the microfabricated ringlens can lead to a different behaviour of the quantum degenerate gas, because the tight confinement in the radial and axial direction of the ring-lens might lead to a trapped 1D degenerate gas. The 1D regime is obtained, when the motion of the atoms in the transverse directions is confined to zero-point oscillations. This happens, when the temperature and the interaction energy per particle  $\varepsilon$  do not exceed the radial level spacing  $\hbar\omega_\perp$ . The confinement in one dimension has a remarkable feature: When the atomic density is lowered, the interactions between the atoms become more important and the character of the system changes. For very low densities, a Tonks-Girardeau gas can be formed [86, 87, 88], where the bosonic atoms behave like fermions.

In the following it is assumed that a condensate is loaded into a tubes with strong two-dimensional confinement. The tight confinement is in the radial direction, and the atoms can propagate freely in the longitudinal direction. A trapped 1D gas is characterized by a single parameter  $\gamma$ , which is the ratio between the interaction energy and the kinetic energy of the ground state:

$$\gamma = \frac{mg_{1D}}{\hbar^2 n_{1D}}, \quad (5.4)$$

where  $g_{1D}$  is the 1D coupling constant of the interaction potential, and  $n_{1D}$  is the the 1D density. The interaction potential can be approximated by a two-atom interaction potential [89, 90]:

$$U_{1D}(z) = g_{1D}\delta(z). \quad (5.5)$$

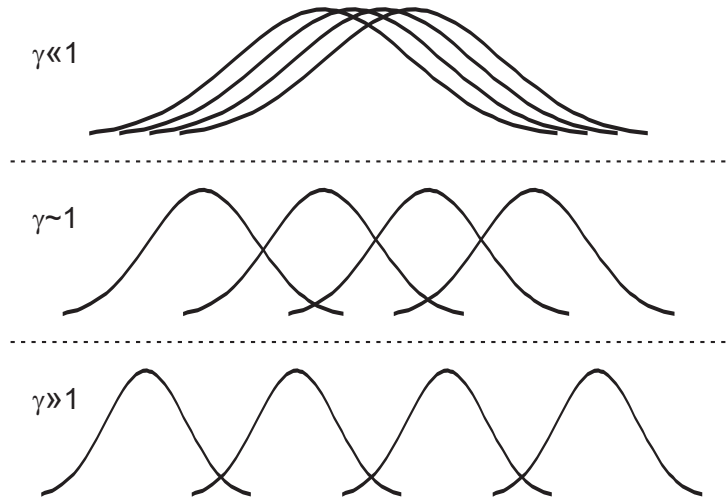


*Fig. 5.2:* Atom distributions of a 1D quantum degenerate gas. As  $\gamma$  increases, the length of the single particle wave function  $\lambda$  becomes smaller, while the interparticle spacing  $r$  becomes larger, until the bosons become spatially distinct, which resembles fermionic behaviour. For a gas trapped in a longitudinal tube,  $\gamma$  can be changed by transversely squeezing the tube or by changing the density. The gas acts like a fluid for  $\gamma \ll 1$ , and therefore expands axially when squeezed. For increasing  $\gamma$ , the squeezing affects the axial expansion less and less. For  $\gamma \gg 1$ , the gas is deep in the Tonk-Girardeau regime, and transverse squeezing has no effect on the axial distribution (or on the energy) [69]

The coupling constant is given by:

$$g_{1D} = \frac{-\hbar^2}{\tilde{\mu}a_{1D}}, \quad (5.6)$$

with the one dimensional scattering length  $a_{1D} = \frac{-a_{\perp}^2}{a}(1 - C\frac{a}{a_{\perp}})$  [89, 90], and the constant  $C = 1.4603$ ,  $a_{\perp} = \sqrt{\frac{\hbar}{\tilde{\mu}\omega_{\perp}}}$  is the size of the ground state in the radial direction (see also Eq. 2.14), and  $\tilde{\mu} = m/2$  is the reduced mass.

For high densities ( $\gamma \gg 1$ ), the system is weakly interacting, and in a harmonic potential Bose-Einstein condensation is possible. This 1D BEC resembles a condensate trapped in three dimensions. However, when the particle density  $n$  is decreased, the interactions between the atoms become more important, whereas a 3D gas would become more ideal. Decreasing the density in a 1D trap reduces the kinetic energy of the ground state, and the kinetic energy may become smaller than the interaction energy. When the interaction energy equals the kinetic energy ( $\gamma \approx 1$ ), adding an optical lattice along the axial direction changes the superfluid phase into a Mott insulator phase [91, 92]. When the density is decreased even more ( $\gamma \ll 1$ , a similar effect is attained by increasing the trapping frequencies in the radial direction), the repulsive interactions between the bosonic atoms dominate. The bosons minimize their repulsion, by preventing them from occupying the same region of space. This is called a Tonks-Girardeau gas. This resembles the Pauli exclusion principle for fermions, causing the bosonic atoms to exhibit fermionic properties, but the bosons do not have to be in another momentum states, as would be the case for fermions. The three regimes are depicted in figure 5.2. The first Tonks-Girardeau gases were observed in the group of Bloch [93] and Weiss [69], where they created the Tonks-Girardeau gas in an optical lattice.

An interesting feature of the Tonks-Girardeau gas is that it resembles a fermionic gas. Therefore, it is possible to map the impenetrable bosonic system one to one onto a gas of noninteracting fermions. For  $N$  bosons confined in an one-dimensional box with length  $L$  the ground state of the system  $\Psi^B$  is given by an absolute value of the  $N$  particle ideal Fermi gas [86, 89]:

$$\Psi^B = |\Psi^F|, \quad (5.7)$$

where the ground state of the Fermi gas is described by:

$$\Psi^F(z_1, \dots, z_N) = \frac{1}{\sqrt{N!L^N}} \det(e^{ik_{\alpha}z_{\beta}}), \quad (5.8)$$

with

$$k_\alpha = \frac{2\pi}{L}\alpha, \quad (5.9)$$

where  $\alpha$  is an integer, and  $k_\alpha \leq |k_F|$  and  $k_F = \frac{\pi(N-1)}{L}$  is the one-dimensional Fermi radius. The Slater determinant guarantees that the wavefunction vanishes whenever two particles occupy the same position in space. In other words, the bosons in the Tonks-Girardeau gas are not allowed to occupy the same region of space. As a result, the bosons are distributed over a more extended region in momentum space than in the case of an ideal, or weakly interacting Bose gas. In a one-dimensional box with length  $L$  this means that there exists an upper limit to the number of atoms [89]:

$$N \ll \frac{L}{\pi|a_{1D}|}. \quad (5.10)$$

In the case of our ring-shaped dipole trap, we can say that the length of the one dimensional box is given by the circumference of the ring  $L = 2\pi \cdot 7.5 \cdot 10^{-4}$  [94, 95]. For our radial trap frequency  $\omega_r = 2\pi \cdot 30$  kHz this would mean that we cannot load more than 2500 atoms in our trap to obtain a Tonks-Girardeau gas. However, our axial trap frequency is much smaller, this will effect the 1D gas such that we need an even lower number of atoms in our trap for a Tonks-Girardeau gas. Using the axial trap frequency  $\omega_z = 2\pi \cdot 3$  kHz, the maximum number of atoms becomes 230.

#### 5.4 A Possible Interferometry Experiment

When we want to use the ring as an interferometer, we have to be able to split the atoms in the ring, guide them along the two arms of the ring, and recombine them on the other side. When the ring is illuminated by a line-shaped laser beam, then depending on the position of the laser beam with respect to the ring-lens, we have one or two maxima (Fig. 5.3). By moving the beam from the top to the bottom, we can make a single well potential split into a double well potential, and recombine it back into a single well potential (Fig. 5.4). A Bose-Einstein condensate loaded in the single well potential of the line-shaped laser beam is thus split in two clouds when the beam is moved across the ring-lens. Upon recombination, the two clouds can interfere with one another.

Another experiment, which enhances the sensitivity of the interferometer,

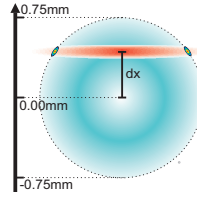


Fig. 5.3: Picture taken from reference [85]. By illuminating a part of the ring with a line-shaped laser beam, we obtain one or two maxima, depending on the position of the laser beam with respect to the ring-lens.

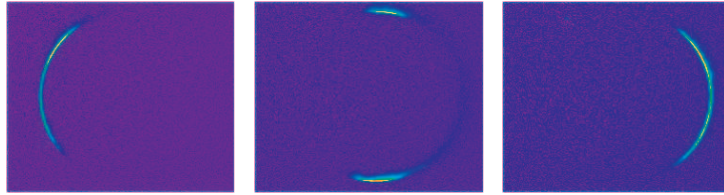


Fig. 5.4: Picture taken from reference [85]. Part of the ringlens is illuminated by a line-shaped laser beam, which has a horizontal waist of  $301 \mu\text{m}$  and a vertical waist of  $1853 \mu\text{m}$ . The ring has a diameter of  $1.5 \text{ mm}$ . Thermal atoms were loaded in the potential created by the line-shaped laser beam. Atoms loaded in the potential can be moved along the ring, when the line-shaped beam is moved from the left to the right. The atoms are split in two clouds and recombined on the right side of the ring.

deals with the interference of two solitons [96]. A soliton is a self-reinforcing solitary wave that maintains its shape while it travels at constant speed. It was described for the first time in 1834 by John Scott Russel who observed the phenomenon in water. The soliton can propagate without dispersing, because nonlinear effects compensate the dispersion. In a Bose-Einstein condensate, the nonlinearity is provided by the mean-field energy  $V_{int} = gn(\vec{r}) = \frac{4\pi\hbar^2 a n(\vec{r})}{m}$  (Eq. 2.28). Depending on whether the interaction is repulsive ( $a > 0$ ) or attractive ( $a < 0$ ), the solitons are either dark or bright, respectively. A bright soliton is a peak in the amplitude of the density, whereas a dark soliton is characterized by a local density minimum with a phase step at the position of the minimum. The first solitons detected in BECs were dark solitons [97, 98], but with the usage of Feshbach resonances, a bright soliton could be

detected only a few years later [99]

Because we create Bose-Einstein condensates with rubidium ( $^{87}\text{Rb}$ ) atoms, which have a positive scattering length, we can only create dark solitons, unless we use Feshbach resonances to tune the scattering length [100]. Solitons can be generated with the method of phase imprinting [101], where a phase step is drawn onto the condensate. This can be done with a far detuned light pulse, which projects a mask onto the condensate. Because of the light shifts, a phase distribution proportional to the light distribution is imprinted. To generate solitons in a condensate which homogeneously fills our ring-potential, we can imprint a phase on half of the BEC in the ring. We then obtain so-called gray solitons whose phase step is not infinite. The velocity of a gray soliton depends on the imposed phase shift [95, 102]. Another possibility to create a phase step is to pierce the ring with a high intense blue detuned laser beam [95, 102].



## 6. SOME CONCLUDING REMARKS

In this thesis, it was shown that we have achieved an all-optical Bose-Einstein condensation with rubidium atoms. The rubidium atoms were loaded in an optical potential created by two focussed laser beams intersecting under a  $90^\circ$  angle. By optimizing the loading of atoms from the MOT into the dipole trap, we were able to trap  $\sim 350,000$  atoms at the crossing point. The atoms were subsequently evaporatively cooled down to quantum degeneracy by ramping down the laser power with three linear ramps. Bose-Einstein condensation has been proven by using the anisotropic expansion of a quantum degenerate gas trapped in an anisotropic potential. We obtained  $\sim 5,000$  condensed atoms.

As a next step, we will load a condensate into the ring-shaped potential. This will entail lots of interesting physics, among other things the crossover from a 1D BEC into a Tonks-Girardeau gas. The ring can be used as a Sagnac atom interferometer. Loading the BEC into the potential created by illuminating the ring-lens with a line-shaped laser beam enables us to split the BEC and recombine it by moving the laser beam across the ring. Recombining the BEC in the trap leads to nonlinear effects which can generate solitons. Solitons can also be made in the Tonks-Girardeau gas by phase imprinting the gas, or by piercing the Tonks-Girardeau gas with a blue detuned laser beam.

Since the experimental setup for generating Bose-Einstein condensates has been built anew at the "Technische Universität Darmstadt", there are a few things that we can improve. Among other things, we can "recycle" the dipole trap beam: Instead of splitting the beam in two, we can use one beam and send its transmission through the vacuum chamber back through another chamber window, so that it can cross under  $90^\circ$  with itself. This doubles the intensity and thus the optical trap depth. A downfall of this system is that we cannot control the intensity of the two beams creating the crossed dipole trap separately.

A second absorption detection setup has been implemented in the ex-

periment, which images the BEC from the side and can thus detect atoms under the influence of gravity. This will improve the detection of quantum degeneracy, since we will be able to see thermal clouds leaving the dipole trap early separate from the condensed cloud (section 4.5).

We can neutralize the effect that gravity has on the dipole potential by adding a magnetic field which precisely counteracts the gravitation. This will improve our dipole trap at low intensities, so that the atoms do not disappear through the gravitational sag.

As a concluding remark, I would like to mention that our condensates will not only be transferred into the ring potential, but also into other potentials created by microfabricated optical elements, such as the dipole trap array or the cylindrical microlens array. The amount of possible dipole trap configurations that we can create with the microlenses are extensive. The huge range of differently shaped potentials allows us to investigate phenomena, which before could only be investigated in solid states. For example, the Mott insulator phase can be explored in dipole trap arrays, where the two-dimensional periodic structure resembles the crystalline structure of a solid state. In our specific case, each potential well will be individually addressable and the individual well separation can be altered. In such a periodic structure, Bloch oscillations (another solid state phenomena) can appear when the array is accelerated. A specific interest which we will investigate in the near future is, what happens with the atoms of our condensate, when we accelerate the condensate over a periodic potential.

## APPENDIX



## A. THE RUBIDIUM ATOM

The element rubidium 87 was chosen for the Bose-Einstein experiment, because the positive scattering length and the transition wavelengths of the  $D$  lines lying in the infra-red make it an excellent candidate for laser cooling and Bose-Einstein condensation. The transition wavelengths can be easily reached with standard laser diodes. We use the  $D2$  for cooling the Rubidium atoms. The cooling transition of the rubidium atom is the  $5^2S_{1/2}, F = 2 \rightarrow 5^2P_{3/2}, F' = 3$  transition. A small probability exists for atoms to excite to the  $5^2P_{3/2}, F' = 2$  level. Therefore, a repumping laser is needed to pump them back into the cooling cycle. The repumping laser is resonant with the  $5^2S_{1/2}, F = 1 \rightarrow 5^2P_{3/2}, F' = 2$  transition (Fig. A.2).

More information on the  $^{87}\text{Rb}$   $D$  lines can be found in reference [103].

Atomic number		37
Abundance $^{87}\text{Rb}$		27.83%
Mass	$m$	$1.443 \cdot 10^{-25}$ kg
Nuclear spin	$I$	3/2
S-wave scattering length	$a$	$5.819 \cdot 10^{-9}$ m

Tab. A.1: The rubidium 87 atom.

Lifetime $5^2P_{1/2}$	$\tau_{life}$	27.70 ns
Wavelength (in air)	$\lambda_{D1}$	794.766 nm
Transition frequency	$\omega_{D1}$	$2\pi \cdot 377.107$ THz
Linewidth	$\Gamma_{D1}/2\pi$	5.7500 MHz
Recoil energy	$E_R/\hbar = h/2m\lambda^2$	3.6325 kHz
Recoil temperature	$T_R$	348.66 nK
Recoil velocity	$v_R$	$5.7754$ mms $^{-1}$

Tab. A.2: Parameters of the D1 line.

Lifetime $5^2P_{3/2}$	$\tau_{life}$	26.24 ns
Wavelength (in air)	$\lambda_{D2}$	780.032 nm
Transition frequency	$\omega_{D2}$	$2\pi \cdot 384.230$ THz
Linewidth	$\Gamma_{D2}/2\pi$	6.0666 MHz
Recoil energy	$E_R/\hbar = h/2m\lambda^2$	3.7710 kHz
Recoil temperature	$T_R$	361.96 nK
Recoil velocity	$v_R$	$5.8845$ mms $^{-1}$
Doppler temperature	$T_{Doppler}$	$145.57$ $\mu\text{K}$
Saturation intensity	$I_s$	$1.669$ mWcm $^{-2}$

Tab. A.3: Parameters of the D2 line.

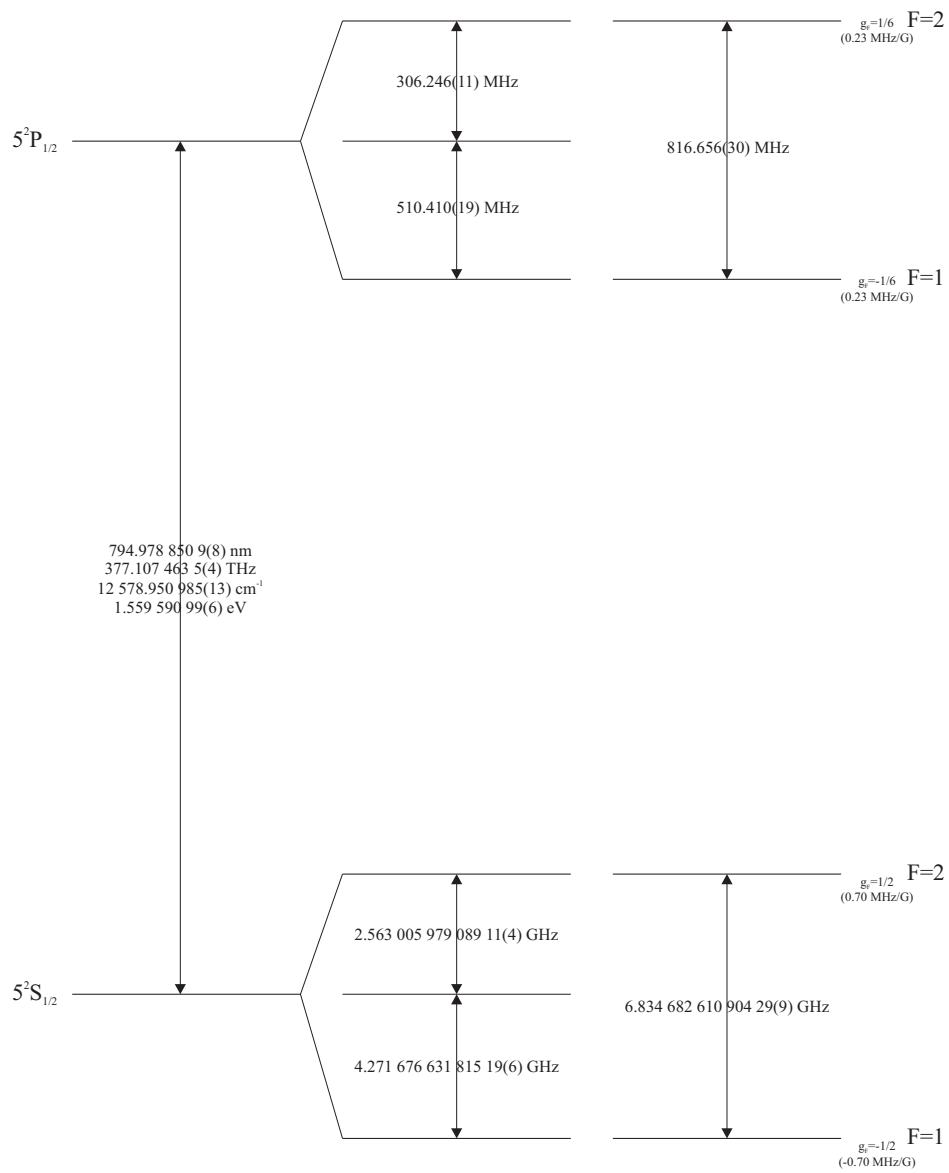


Fig. A.1: The  $D1$  transition of the rubidium 87 atom.

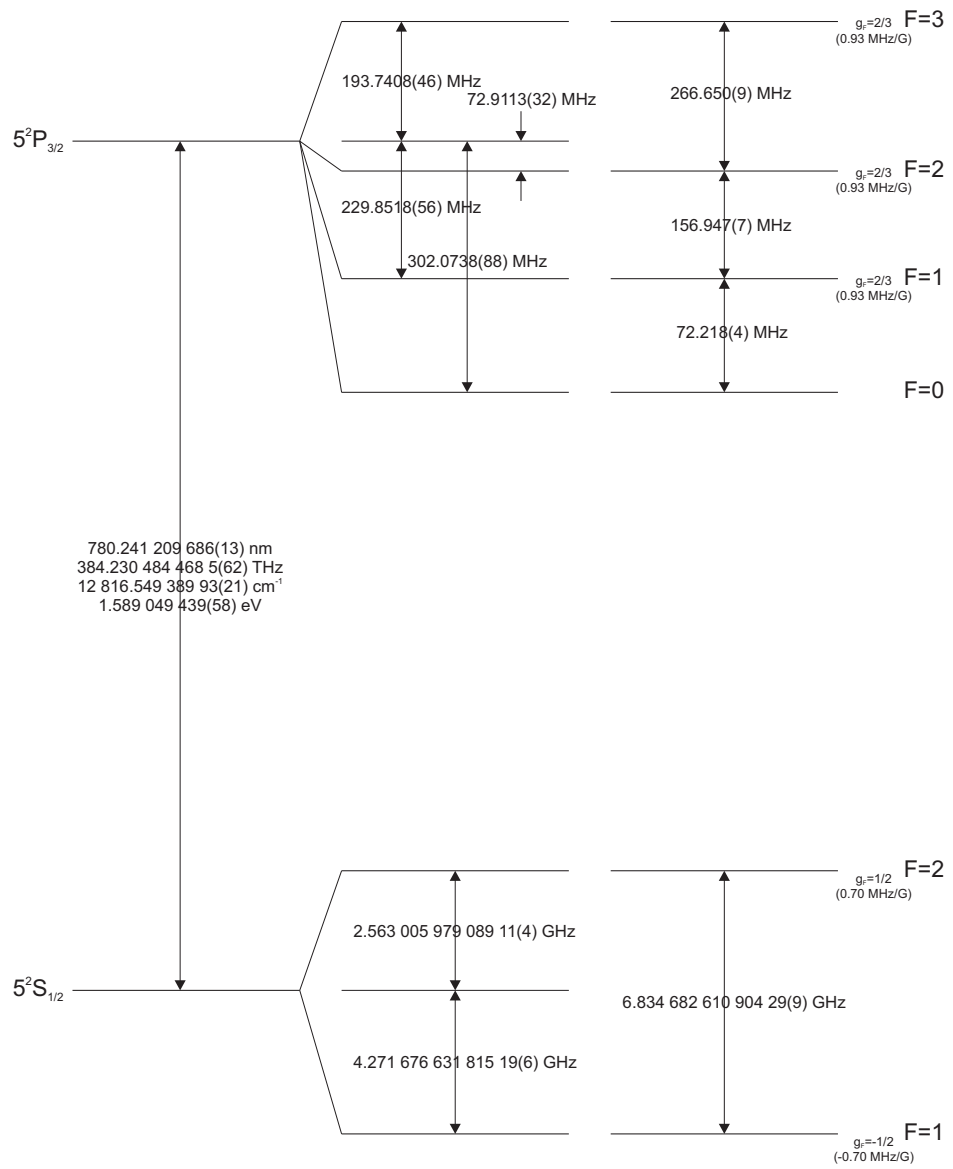


Fig. A.2: The  $D_2$  transition of the rubidium 87 atom.

## B. PARAMETERS OF THE OPTICAL DIPOLE TRAP

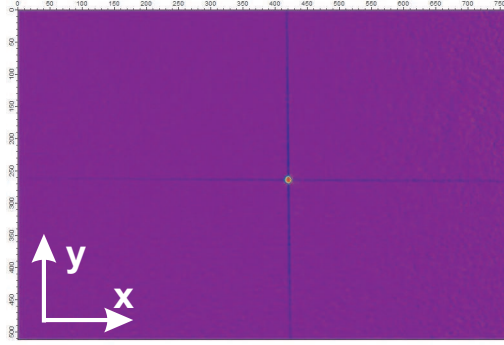


Fig. B.1: The crossed optical dipole trap.

1/e waist, beam in $x$ -direction	$w_x$	49 $\mu\text{m}$
1/e waist, beam in $y$ -direction	$w_y$	40 $\mu\text{m}$
Optical power	$P$	8.2 W
Trap depth	$U_{Dip}/k_B$	430 $\mu\text{K}$
Scattering rate	$\Gamma_s$	2 photons/s
Oscillation frequencies, $x$ -direction	$\omega_x$	$2\pi \cdot 1,085$ Hz
Oscillation frequencies, $y$ -direction	$\omega_y$	$2\pi \cdot 980$ Hz
Oscillation frequencies, $z$ -direction	$\omega_z$	$2\pi \cdot 1,460$ Hz
Number of atoms	$N$	$\sim 350,000$ atoms
Density	$n$	$1.1 \cdot 10^{12}$ atoms/cm <sup>3</sup>
Temperature	$T$	$\sim 30$ $\mu\text{K}$
Initial phase space density	$\rho_{psd}$	$4.4 \cdot 10^{-5}$

Tab. B.1: Parameters of the optical dipole trap.

## BIBLIOGRAPHY

- [1] M. H. Anderson and et al., “Observation of Bose-Einstein Condensation in a Dilute Atomic Vapor,” *Science* **269**, 198 (1995).
- [2] C. C. Bradley and et al., “Evidence of Bose-Einstein Condensation in an Atomic Gas with Attractive Interactions,” *Physical Review Letters* **75**, 1687 (1995).
- [3] K. B. Davis and et al., “Bose-Einstein Condensation in a Gas of Sodium Atoms,” *Physical Review Letters* **75**, 3969 (1995).
- [4] S. Chu and et al., “Experimental observation of optically trapped atoms,” *Physical Review Letters* **57**, 314 (1986).
- [5] T. Weber and et al., “Bose-Einstein Condensation of Cesium,” *Science* **299**, 232 (2003).
- [6] M. D. Barrett and et al., “All-optical formation of an atomic Bose-Einstein condensate,” *Physical Review Letters* **87**, 010404 (2001).
- [7] R. Dumke and et al., “All-optical generation and photoassociative probing of sodium Bose-Einstein condensates,” *New Journal of Physics* **8**, 64 (2006).
- [8] Y. Takasu and et al., “Spin-singlet Bose-Einstein condensation of two-electron atoms,” *Physical Review Letters* **91**, 040404 (2003).
- [9] T. Kinoshita and et al., “All-optical Bose-Einstein condensation using a compressible crossed dipole trap,” *Physical Review A* **71**, 011602(R) (2005).
- [10] G. Birkl and et al., “Atom optics with microfabricated optical elements,” *Optics Communications* **191**, 67 (2001).

- [11] O. Stern, "Beugung von Molekularstrahlen an Gitter einer Kristallspaltfläche," *Naturwiss.* **17**, 391 (1929).
- [12] I. Esterman and et al., "Beugung von Molekularstrahlen," *Z. Physik* **61**, 95 (1930).
- [13] C. Cohen-Tannoudji, "Nobel Lecture: Manipulating atoms with photons," *Review of Modern Physics* **70**, 707 (1998).
- [14] W. Phillips, "Nobel Lecture: Laser cooling and trapping of neutral atoms," *Review of Modern Physics* **70**, 721 (1998).
- [15] C. S. Adams and et al., "Atom Optics," *Physics Reports* **240**, 143 (1994).
- [16] B. Young, M. Kasevich, and S. Chu, *Atom Interferometry* (Academic Press, San Diego, 1997).
- [17] K. Gibble and et al., "Laser-cooled Cs frequency standard and a measurement of the frequency shift due to ultracold collisions," *Physical Review Letters* **70**, 1771 (1993).
- [18] C. Fertig and et al., "Measurement and Cancellation of the Cold Collision Frequency Shift in an 87Rb Fountain Clock," *Physical Review Letters* **85**, 1622 (2000).
- [19] M. Kasevich and et al., "Measurement of the gravitational acceleration of an atom with a light-pulse atom interferometer," *Applied Physics B* **54**, 321 (1992).
- [20] M. J. Snadden and et al., "Measurement of the Earth's Gravity Gradient with an Atom Interferometer-Based Gravity Gradiometer," *Physical Review Letters* **81**, 971 (1998).
- [21] A. Peters and et al., "Measurement of gravitational acceleration by dropping atoms," *Nature* **400**, 849 (1999).
- [22] F. Riehle and et al., "Optical Ramsey spectroscopy in a rotating frame: Sagnac effect in a matter-wave interferometer," *Physical Review Letters* **67**, 177 (1991).

- 
- [23] A. Lenef and et al., "Rotation Sensing with an Atom Interferometer," *Physical Review Letters* **78**, 760 (1997).
- [24] T. L. Gustavson and et al., "Precision Rotation Measurements with an Atom Interferometer Gyroscope," *Physical Review Letters* **78**, 2046 (1997).
- [25] R. Folman and et al., "Microscopic atom optics: from wires to an atom chip," *Advances in Atomic, Molecular and Optical Physics* **48**, 263 (2002).
- [26] D. Müller and et al., "Guiding Neutral Atoms Around Curves with Lithographically Patterned Current-Carrying Wires," *Physical Review Letters* **83**, 5194 (1999).
- [27] N. H. Dekker and et al., "Beam Splitter for Guided Atoms," *Physical Review Letters* **84**, 1124 (2000).
- [28] D. Cassettari and et al., "Guiding Neutral Atoms on a Chip," *Physical Review Letters* **85**, 5483 (2000).
- [29] W. Hänsel and et al., "Bose-Einstein Condensation on a microelectronic chip," *Nature* **413**, 498 (2001).
- [30] H. Ott and et al., "Bose-Einstein Condensation in a Surface Microtrap," *Physical Review Letters* **87**, 230401 (2001).
- [31] C. Henkel and et al., "Loss and heating of particles in small and noisy traps," *Applied Physics B* **69**, 379 (1999).
- [32] C. Henkel and et al., "Coherent transport of matter waves," *Applied Physics B* **72**, 73 (2001).
- [33] W. Ketterle, D. S. Durfee, and D. M. Stamper-Kurn, *Making, probing and understanding Bose-Einstein condensates, Proceedings of the International School of Physics "Enrico Fermi", Course CXL, edited by M. Inguscio, S. Stringari and C.E. Wieman* (IOS Press, Amsterdam, 1999).
- [34] C. J. Pethick and H. Smith, *Bose-Einstein condensation in dilute gases* (Cambridge University Press, Cambridge, 2004).

- [35] F. Dalfovo and et al., “Theory of Bose-Einstein condensation in trapped gases,” *Review of Modern Physics* **71**, 463 (1999).
- [36] W. Ketterle and et al., “Bose-Einstein condensation of a finite number of particles trapped in one or three dimensions,” *Physical Review A* **54**, 656 (1996).
- [37] K. Kirsten and et al., “Bose-Einstein condensation of atomic gases in a general harmonic-oscillator confining potential trap,” *Physical Review A* **54**, 4188 (1996).
- [38] M. Arndt and et al., “Observation of a Zero-Energy Resonance in Cs-Cs Collisions,” *Physical Review Letters* **79**, 625 (1997).
- [39] M. Naraschewski and et al., “Analytical description of a trapped semi-ideal Bose gas at finite temperature,” *Physical Review A* **58**, 2423 (1998).
- [40] M.-O. Mewes and et al., “Bose-Einstein Condensation in a Tightly Confining dc Magnetic Trap,” *Physical Review Letters* **77**, 416 (1996).
- [41] N. Bogoliubov, *Journal of Physics (Moscow)* **11**, 23 (1947).
- [42] P. Fedichev, Ph.D. thesis, Universiteit van Amsterdam, (1999).
- [43] A. L. Fetter, *Theory of a dilute low-temperature trapped Bose condensate, Proceedings of the International School of Physics "Enrico Fermi" on Bose-Einstein Condensation in Atomic Gases, arXiv:cond-mat/9811366v1* (IOS Press, Amsterdam, 1998).
- [44] E. P. Gross, “Hydrodynamics of a Superfluid Condensate,” *Journal of Mathematical Physics* **4**, 195 (1963).
- [45] E. P. Pitaevskii, *Journal of Experimental and Theoretical Physics Letters* **13**, 451 (1961).
- [46] A. Ashkin and et al., “Acceleration and Trapping of Particles by Radiation Pressure,” *Physical Review Letters* **24**, 156 (1970).
- [47] A. Ashkin and et al., “Observation of a single-beam gradient force optical trap for dielectric particles,” *Optics Letters* **11**, 288 (1986).

- 
- [48] R. Grimm, M. Weidemüller, and Y. B. Ovchinnikov, “Optical dipole traps for neutral atoms,” *Advances in Atomic, Molecular and Optical Physics* **42**, 95 (2000).
- [49] A. Ashkin and et al., “Optical trapping and manipulation of viruses and bacteria,” *Science* **235**, 1517 (1987).
- [50] A. Ashkin and et al., “Optical trapping and manipulation of single cells using infrared laser beams,” *Nature* **330**, 769 (1987).
- [51] C. Cohen-Tannoudji and et al., “Dressed-atom description of resonance fluorescence and absorption spectra of a multi-level atom in an intense laser beam,” *Journal of Physics B* **10**, 345 (1977).
- [52] C. Cohen-Tannoudji and et al., “Dressed-atom approach to atomic motion in laser light: the dipole force revisited,” *Journal of the Optical Society of America B* **2**, 1707 (1985).
- [53] W. Demtröder, *Laser Spectroscopy: Basic Concepts and Instrumentation* (Springer Verlag, Berlin, Heidelberg, 1998).
- [54] H. J. Metcalf and P. van der Straten, *Laser Cooling and Trapping* (Springer, New York, 2002).
- [55] W. Vassen, *Introduction to Laser Cooling and Trapping* (Course at the ‘Vrije Universiteit’ in Amsterdam, the Netherlands, 2000).
- [56] R. Frisch, “Experimenteller Nachweis des Einsteinschen Strahlungsrückstosses,” *Z. Phys.* **86**, 42 (1933).
- [57] E. L. Raab and et al., “Trapping of Neutral Sodium Atoms with Radiation Pressure,” *Physical Review Letters* **59**, 2631 (1987).
- [58] W. Ketterle and et al., “High Densities of Cold Atoms in a Dark Spontaneous-Force Optical Trap,” *Physical Review Letters* **70**, 2253 (1993).
- [59] L. Ricci and et al., “A compact grating-stabilized diode laser system for atomic physics,” *Optics Communications* **117**, 541 (1995).
- [60] U. Schünemann and et al., “Simple scheme for tunable frequency offset locking of two lasers,” *Review of Scientific Instruments* **70**, 242 (1999).

- [61] T. Stace and et al., “Laser offset-frequency locking using a frequency-to-voltage convertor,” *Measurement Science and Technology* **9**, 1635 (1998).
- [62] X. Baillard and et al., “Interference-filter-stabilized external-cavity diode lasers,” *Optics Communications* **266**, 609 (2006).
- [63] H. Eklund and et al., “Rotation of laser beam polarization in acousto-optic devices,” *Optical and Quantum Electronics* **7**, 73 (1975).
- [64] S. Bali and et al., “Quantum-diffractive background gas collisions in atom-trap heating and loss,” *Physical Review A* **60**, R29 (1986).
- [65] E. Burt and et al., “Coherence, Correlations, and Collisions: What One Learns about Bose-Einstein Condensates from Their Decay,” *Physical Review Letters* **79**, 337 (1997).
- [66] R. Jáuregui and et al., “Nonperturbative and perturbative treatments of parametric heating in atom traps,” *Physical Review A* **64**, 053408 (2001).
- [67] S. Friebel and et al., “CO<sub>2</sub>-laser optical lattice with cold rubidium atoms,” *Physical Review A* **57**, R20 (1998).
- [68] G. Cennini and et al., “Bose-Einstein condensation in a CO<sub>2</sub>-laser optical dipole trap,” *Applied Physics B* **77**, 773 (2003).
- [69] T. Kinoshita and et al., “Observation of a One-Dimensional Tonks-Girardeau Gas,” *Science* **305**, 1125 (2004).
- [70] S. J. M. Kuppens and et al., “Loading an optical dipole trap,” *Physical Review A* **62**, 013406 (2000).
- [71] A.-L. Gehrmann, *Evaporative Kühlung in optischen Dipolfallen* (Leibniz Universität Hannover, 2005).
- [72] N. Masuhara and et al., “Evaporative Cooling of Spin-Polarized Atomic Hydrogen,” *Physical Review Letters* **61**, 935 (1988).
- [73] W. Petrich and et al., *Atomic Physics 14, edited by C.E. Wieman and D. Wineland* (AIP, New York, 1994).

- 
- [74] K. Bongs, *Atomoptische Experimente mit Bose-Einstein Kondensaten* (Leibniz Universität Hannover, 1999).
- [75] W. Ketterle and et al., “Evaporative cooling of trapped atoms,” *Advances in Atomic, Molecular, and Optical Physics* **37**, 181 (1996).
- [76] K. M. O’Hara and et al., “Scaling laws for evaporative cooling in time-dependent optical traps,” *Physical Review A* **64**, 051403 (2001).
- [77] O. J. Luiten and et al., “Kinetic theory of the evaporative cooling of a trapped gas,” *Physical Review A* **53**, 381–389 (1996).
- [78] Y. Castin and et al., “Bose-Einstein condensates in time dependent traps,” *Physical Review Letters* **77**, 5315 (1996).
- [79] Y. Kagan and et al., “Effect of Bose condensation on inelastic processes in gases,” *Journal of Experimental and Theoretical Physics* **42**, 209 (1985).
- [80] J.-P. Martikainen and et al., “Bose-Einstein condensation in shallow traps,” *Physical Review A* **63**, 043602 (2001).
- [81] J.-P. Martikainen and et al., “Erratum: Bose-Einstein condensation in shallow traps,” *Physical Review A* **65**, 039903(E) (2001).
- [82] A. D. Cronin and et al., “Atom interferometers,” arXiv:0712.3703v1 (2008).
- [83] J. A. Sauer and et al., “Storage ring for neutral atoms,” *Physical Review Letters* **87**, 270401 (2001).
- [84] S. Wu and et al., “Bidirectional propagation of cold atoms in a ”stadium”-shaped magnetic guide,” *Physical Review A* **70**, 013409 (2004).
- [85] A. Lengwenus, *Manipulation der internen und externen Freiheitsgrade neutraler Atome in optischen Mikropotentialen* (Institut für Angewandte Physik der Technische Universität Darmstadt, 2008).
- [86] M. Girardeau and et al., “Relationship between systems of impenetrable Bosons and Fermions in one dimension,” *Journal of Mathematical Physics* **1**, 516 (1960).

- [87] H. Lieb and et al., “Exact analysis of an interacting Bose gas I. The general solution and the ground state,” *Physical Review* **130**, 1605 (1963).
- [88] H. Lieb and et al., “Exact analysis of an interacting Bose gas II. The excitation spectrum,” *Physical Review* **130**, 1616 (1963).
- [89] M. Olshanii and et al., “Atomic scattering in the presence of an external confinement and a gas of impenetrable Bosons,” *Physical Review Letters* **81**, 938 (1998).
- [90] V. Dunjko and et al., “Bosons in cigar-shaped traps: Thomas-Fermi regime, Tonks-Girardeau regime, and in between,” *Physical Review Letters* **86**, 5413 (2001).
- [91] T. Stöferle and et al., “Transition from a Strongly Interacting 1D Superfluid to a Mott Insulator,” *Physical Review Letters* **92**, 130403 (2004).
- [92] M. Greiner and et al., “Quantum phase transition from a superfluid to a Mott insulator in a gas of ultracold atoms,” *Nature* **415**, 39 (2002).
- [93] B. Paredes and et al., “Tonks-Girardeau gas of ultracold atoms in an optical lattice,” *Nature* **429**, 277 (2004).
- [94] M. D. Girardeau and et al., “Dark solitons in a one-dimensional condensate of hard core bosons,” *Physical Review Letters* **84**, 5691 (2000).
- [95] M. D. Girardeau and et al., “Quantum mechanics of one-dimensional trapped Tonks gases,” *arXiv:cond-mat/0104585v1* (2008).
- [96] A. Negretti and et al., “Enhanced phase sensitivity and soliton formation in an integrated BEC interferometer,” *Journal of Physics B* **37**, L385 (2004).
- [97] S. Burger and et al., “Dark solitons in Bose-Einstein condensates,” *Physical Review Letters* **83**, 5198 (1999).
- [98] J. Denschlag and et al., “Generating solitons by phase engineering of a Bose-Einstein condensate,” *Science* **287**, 97 (2000).
- [99] L. Khaykovich and et al., “Formation of a matter-wave bright soliton,” *Science* **296**, 1290 (2002).

- 
- [100] T. Volz and et al., “Characterization of elastic scattering near a Feshbach resonance in rubidium 87,” *Physical Review A* **68**, 010702(R) (2003).
- [101] L. Dobrek and et al., “Optical generation of vortices in trapped Bose-Einstein condensates,” *Physical Review A* **60**, R3381 (1999).
- [102] M. D. Girardeau and et al., “Interference of a thermal Tonks gas on a ring,” *Physical Review Letters* **89**, 170404 (2002).
- [103] D. A. Steck, “Rubidium 87 D Line Data,” Technical report, Los Alamos National Laboratory, <http://steck.us/alkalidata> (2008).



## ACKNOWLEDGEMENTS

Having come to the end of my thesis, I want to dedicate the final words to the people who helped me create a successful research project.

First of all I want to thank Prof. Dr. Gerhard Birkl for giving me the opportunity to work in the fascinating research area of cold atoms and Bose-Einstein condensates. I have learned many new things under his supervision.

When I started in Hannover, I worked in a lab which held two separate experiments and four students working on them. I thank André Lengwenus for being my friend from the start and the many helpful discussions, and Anna-Lena Gehrman, with whom I worked very closely on one experiment. I also have to thank Michael Volk for forcing me to speak German right from the beginning, my German is now very good, even though I refuse to write my thesis or the acknowledgements in German. Falk Scharnberg also worked for a very short period on my experiment. Besides benefiting from his profound knowledge, I very much enjoyed his company.

I thank Prof. Dr. Wolfgang Ertmer, in his group I have done the first half of my PhD. I also want to thank all the members of his group at the IQO, I enjoyed the friendly atmosphere and I will never forget the many times we went to a "Biergarten", to Steintor, and the many discussions we had on the balcony.

Before we moved to Darmstadt, Olli Wille joined my experiment. I thank him for the many many discussions, I had a lot of fun, and I guess the rest of the group as well.

In the end, three experiments and six people moved to Darmstadt. Without the help of Jens Kruse, Olli Wille, Andre Lengwenus, Wouter van Drunen and Dr. Norbert Herschbach, the experiment would never have been moved. Thank you. Additionally, I want to thank Wouter van Drunen for being my Dutch friend in Germany.

Many Darmstadt students wanted to join the new group APQ, and I thank all the "Miniforscher", Bachelorstudents, "HIWIs" and Masterstudents, especially Felix Steinebach, Michael Fraczek, Thomas Lauber, Markus Krut-

zik and Susanne Hertsch. Their einthusiasm makes our group great.

My project would not have been possible without the administrative skills of Frau Pfennig and Frau Hünitzsch from Hannover, and Gabi Jenny-Deußer, who has become the most important person of our group in Darmstadt

I also want to thank our mechanical workshop under Herr Kalbfleisch for creating many high class parts for my experiment.

Als laatste wil ik mij bedanken bij mijn twee beste vriendinnen, Elles en Elise, voor hun ondersteuning en vertrouwen.

## CURRICULUM VITAE

### Personal information

Date of Birth	13.05.1977
Place of Birth	Hoorn, the Netherlands
Citizenship	Dutch

### Education

06/1997	"Atheneum R.S.G. Wiringherlant" in Wieringerwerf, the Netherlands. General qualification for university entrance.
08/1997 – 08/1998	"Vrije Universiteit" in Amsterdam, the Netherlands. Propaedeutic diploma in physics.
08/1998 – 05/2004	"Vrije Universiteit" in Amsterdam, the Netherlands. Physics study.
09/2002 – 08/2003	"Australian National University" in Canberra, Australia. Master thesis with the topic: "A compact liquid helium-cooled He* beam line for efficient MOT loading".
05/2004	Master of science degree in physics.
10/2004 – 10/2006	"Institut für Quantenoptik, Leibniz Universität Hannover" in Hannover, Germany. Doctoral study in physics.
since 11/2006	"Institut für Angewandte Physik, Technische Universität Darmstadt" in Darmstadt, Germany. Continuation doctoral study in physics.